NTNU

Limiting mechanisms for the torque density of wind turbine drivetrains

MSc Thesis

Wichert Kooloos

3 July, 2019

Preface

With this thesis I will finalize the graduation process for obtaining a master's degree in Offshore Engineering from Delft University of Technology and a master's in Technology - Wind Energy from the Norwegian University of Science and Technology as part of the European Wind Energy program. The goal of this thesis is to define the limiting mechanisms for three different drivetrain configurations and a scaling model is developed to study the influence of the limiting mechanisms on the torque density. In the last nine months, I have learned a lot about machine design in three different areas of engineering: mechanic, hydraulic and electric. I can say that this helped me to understand how the world around me works a lot better. I would like to take this opportunity to thank my chair, Dr.Ir. Polinder for the elaborate conversations about generator design and getting me started in the new world of electrical power engineering. I would also like to thank Dr.Ir. Nejad for the weekly fruitful and enthusiastic discussions. Reminding me to always take into account the bigger picture. I would also like to thank Dr.Ir. van Ostayen for providing a critical view on the design of the gearbox while also being able to answer all my hydraulic pump related questions. Lastly, but certainly not the least, I would like to thank Dr.Ir. Diepeveen for giving me the opportunity to write my thesis at DOT power and providing me all the practical information that I needed about hydraulic pump design. The last 2 years of my master's would have been very lonely and a bit boring without my fellow EWEM students. I would especially like to thank Sanne, Sara, Johan, Matthijs and Jelle, for always listening to my endless stories. Furthermore, I would like to thank Claire for keeping up with me the last 9 months and of course for making my thesis look aesthetically pleasing. I would like to conclude by thanking my parents Arnold and Clementine and my siter Marit for always being there for me and helping me through the graduation process.

Abstract

As wind turbines continue to increase in size, so do the loads acting on the drivetrain. To handle the higher loads the mass of the drivetrain needs to increase. A better understanding of this mass increase can result in lighter drivetrain design and provide an insight which drivetrain design has the lowest mass potential for large rotor diameters. In this thesis the limiting mechanisms, mass and torque density of three wind turbine drivetrains are investigated for an increasing rotor diameter. The limiting mechanisms in this thesis provide a theoretical limit to the minimum required mass of a drivetrain for increased loading. Through an extensive literature study the limiting mechanisms are found and three scaling models are developed to calculate the torque density of the drivetrains. The drivetrains that are being considered in this thesis are the drivetrain with gearbox and high-speed generator, the direct drivetrain and the hydraulic drivetrain. The following research questions are answered in this thesis:

- What are the limiting mechanisms of the three investigated drivetrain types?
- What are the achievable torque densities of the three investigated drivetrain configurations for increasing rotor diameters?

Two limiting mechanisms are found for the drivetrain with gearbox and high-speed generator: Tooth flank stress **(1.72 GPa)** and Root bending stress **(0.24 GPa)**. The Tooth flank stress is found to be governed by the Hertzian contact strength while the root bending stress is governed by the flexural strength. Two limiting mechanisms for the RFPMSG are found for the airgap flux density **(1 T)** and the current loading **(30 - 200 kA/m)** in the generator windings. The airgap flux density is limited by the saturation of the stator teeth material in the generator whereas the current loading is limited by the heat dissipation of the windings and stator laminations. For the hydraulic pump, the limiting mechanism is found at the interaction of the camring and the cam roller. The maximum stress that is allowed at this point is determined by the Hertzian contact strength of the material and is found to be **(1.72 GPa)**. Using the limiting mechanisms of the three drivetrain configurations, scaling models for the mass and torque density of the three drivetrains have been developed.

Contents

Nomenclature

α	Pressure angle [rad]
α_t	Temperature coefficient [$-$]
δP	Pressure difference [Pa]
ε_α	Transverse contact ratio [$-$]
$\hat{A_s}$	Current loading stator [kA/m]
$\hat{B_g}$	Flux density [T]
λ	Tip speed ratio [$-$]
μ	Magnetic permeability [$-$]
μ_0	Magnetic permeability of a freespace [$-$]
μ_r	Relative magnetic permeability [$-$]
∇T	Temperature gradient [K/m]
ν	Kinematic viscosity [m^2/s]
ν	Poissons number [$-$]
ω	Angular velocity [rad/s]
ϕ	Flux [Wb]
Φ_{cond}	Conductive heat flux [W/m^2]
Φ_{conv}	Convective heat flux [W/m^2]
ρ	Mass density [kg/m^3]
ρ_{air}	Air density [kg/m^3]
ρ_{cu}	Density of copper [kg/m^3]
ρ_{steel}	Density of steel [kg/m^3]
σ_F	Root bending stress [Pa]
σ_h	Hertzian flank pressure [Pa]
σ_C	Hertzian endurance strength [Pa]
σ_{Fmax}	Maximum allowed bending stress [Pa]
σ_{Hmax}	Maximum allowed Hertzian flank pressure [Pa]
τ_p	Pole pitch [m]
τ_s	Slot pitch [m]
a	Centre to centre distance [m]

A_g Airgap area $[m^2]$

A_r Tooth area ratio $[m^2]$

A_s Slot area $[m^2]$

A_t Stator tooth area $[m^2]$

A_{cus} Area of the conductor $[m^2]$

A_{cyl} Cylinder area $[m^2]$

A_{swept} Swept rotor area $[m^2]$

b Gear width $[m]$

b_p Magnet width $[m]$

b_so Slot opening width $[m]$

B_t Flux density tooth $[T]$

b_{cam} Contact area width $[m]$

B_{rm} The remenant flux density $[T]$

b_{sav} Average slot width $[m]$

C Constant $[-]$

C_p Power coefficient $[-]$

D Rotor diameter $[m]$

D_c Conductor diameter $[m]$

D_H Hydraulic parameter $[m]$

D_{begin} Beginning rotor diameter $[m]$

D_{cyl} Cylinder diameter $[m]$

D_{end} Ending rotor diameter $[m]$

D_{gen} Airgap diameter $[m]$

E Module of elasticity $[Pa]$

F_c Peripheral forces on the carrier $[-]$

F_d Force density in the airgap $[kN/m^2]$

F_H Total horizontal reaction force $[N]$

F_p Peripheral force planet $[N]$

F_{cam} Force acting between the cam ring and cam roller $[N]$

F_{Hcam} Horizontal component of the cam force $[N]$

F_{Vcyl}	Vertical component of the cylinder force $[N]$
g	Mechanical airgap $[m]$
g_{eff}	The effective airgap $[m]$
H	Magnetic field strength $[kA/m]$
h	Slot height $[m]$
h_t	Heat convective transfer coefficient $[W/m^2K]$
I	Current $[A]$
I_s	RMS value current through one conductor $[A]$
k	Heat conductivity $[W/km]$
k_a	Thermal conductivity of air $[W/Km]$
k_c	Carter Richter factor $[-]$
k_f	Slot filling factor $[-]$
k_sf	Conductor filling factor $[-]$
k_{asp}	Aspect ratio $[-]$
$K_{F\alpha}$	Factor describing the division of load between teeth $[-]$
$K_{F\beta}$	Load distribution factor for bending $[-]$
$K_{H\alpha}$	Factor describing the division of load between teeth $[-]$
$K_{H\beta}$	Load distribution factor for Hertzian pressure $[-]$
k_{ro}	Relation between outer and pitch diameter of ring gear $[-]$
l_m	Magnet length in direction of magnetization $[m]$
l_s	Stack length $[m]$
L_{cam}	Length of cam roller $[m]$
l_{cus}	Length of the conductor $[m]$
L_{gen}	Length of generator $[m]$
M	Mass $[kg]$
m	module $[m]$
M_c	Mass of carrier $[kg]$
M_p	Mass of planet $[kg]$
m_p	Number of phases $[-]$
M_r	Mass of ring $[kg]$

M_s Mass of sun [kg]

M_{arms} Mass electromagnetic parts of the arms [kg]

M_{cyl} Mass of the generator cylinder [kg]

M_{em} Mass electromagnetic parts [kg]

M_{gear} Mass of single gear [kg]

M_{gen} Mass generator [kg]

M_{NREL} Mass NREL generator [kg]

$M_{parallel}$ Mass of gear pair [kg]

M_{pinion} Mass of pinion gear [kg]

M_{rA} Mass rotor arms [kg]

M_{rC} Mass rotor cylinder [kg]

M_{rI} Mass rotor iron [kg]

M_{rM} Mass rotor magnets [kg]

M_{sA} Mass stator arms [kg]

M_{sCu} Mass stator copper [kg]

M_{sC} Mass stator cylinder [kg]

M_{sI} Mass stator iron [kg]

M_{stage} Mass of stage[kg]

n Gear ratio of a gear stage [n]

N_p Number of planets [$-$]

N_s Number of turns [$-$]

N_τ Number of poles [$-$]

N_{cam} Number of cams [$-$]

N_{cyl} Number of cylinders [$-$]

n_{factor} Gear ratio distribution factor [$-$]

N_{slot} Number of slots [$-$]

Nu Nusselt number [$-$]

P Power [W]

p Number of poles for a machine [$-$]

P_{air} Power in air flow [W]

P_{cool} Cooling power [W]

P_{cu} Power in copper wire [W]

P_{fan} Fan power [W]

P_{loss} Power loss [W]

P_{rated} Rated power [W]

Pr Prandtl number [$-$]

q_p Number of slots per pole phase [$-$]

R Resistance [Ω]

r Radius [m]

R_c radius [m]

r_c Carrier radius [m]

r_p Planet pitch radius [m]

r_r Ring pitch radius [m]

R_s Resistance in a copper wire [Ω]

r_s Sun pitch radius [m]

r_{gear} Pitch radius gear [m]

r_{pinion} Pitch radius pinion [m]

R_{ref} Reference resistance [Ω]

Re Reynolds number [$-$]

S Wetted cooling surface [m^2]

S_{cyl} Stroke length cylinder [m]

T Temperature [K]

T Torque [Nm]

T_d Torque density [Nm/kg]

T_s Surface temperature [K]

T_s Torque sun [Nm]

T_{in} Torque in [Nm]

$T_{m,f}$ Cooling medium temperature [K]

T_{out} Torque out [Nm]

T_{pinion} Torque on pinion [Nm]

T_{ref} Reference temperature [K]

T_{rotor} Wind rotor torque [Nm]

u Gear ratio of a single gear pair [–]

u_{gear} Gear ratio regular gear [–]

u_{pr} Gear ratio planet-ring [–]

u_{ps} Gear ratio planet-sun [–]

V Voltage [V]

v_{air} Air velocity [m/s]

V_{cyl} Volume of a cylinder [m^3]

V_{gen} Volume of generator rotor [m^3]

V_{pump} Displacement volume of the pump [m^3/rev]

V_{rated} Rated wind speed [m/s]

V_{wind} Wind speed [m/s]

W Magnitude of the flow velocity [m/s]

Y_B Helix angle factor for bending [–]

Y_F Form factor for bending [–]

Y_ε Contact ratio factor for bending [–]

Z_H Form factor for Hertzian pressure [–]

Z_M Material factor for the Hertzian pressure [–]

z_p Planet tooth number [–]

z_r Ring tooth number [–]

z_s Sun tooth number [–]

Z_ε Contact ratio factor for Hertzian pressure [–]

z_{pinion} Pinion tooth number [–]

1 Introduction

Since the start of commercial wind power, the industry has been expanding. This expansion translates into the growth in size of wind turbines as well as growth in size of wind farms. The driver behind this growth is the levelised cost of energy (LCOE) and the risk that is involved when investing in wind farms. The LCOE can be described as the costs that are being made to produce energy, divided by the produced energy (1.1) (Tran and Smith, 2018).

$$LCOE = \frac{Total\ Lifetime\ Cost}{Total\ Lifetime\ Energy\ Production} \tag{1.1}$$

The LCOE makes it possible to compare different energy producing technologies. An energy source with a low LCOE is therefore cheap to produce. The reduction in LCOE triggers the offshore wind industry to innovate further. When observing (1.1) it can be concluded that one can lower the LCOE by either increasing the energy production or lowering the total life time cost. The main trend in the offshore wind industry is to save cost and produce more energy by up-scaling the wind turbines (Díaz et al., 2015). As can be seen in figure 1.1, the wind turbines are getting larger every year.

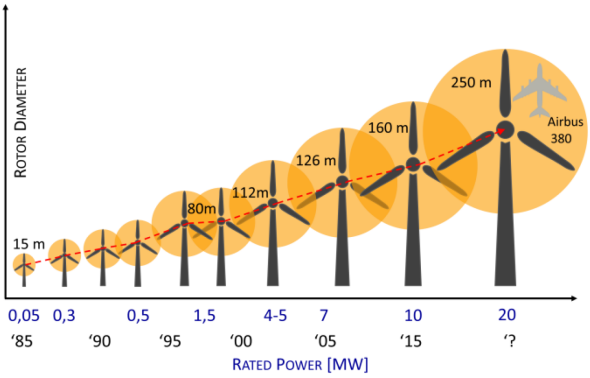

Figure 1.1: Up-scaling of Wind Turbines in Size and Rated Power (Díaz et al., 2015)

All these innovations have lead to a LCOE of 65 euros/MWh in 2017 for offshore wind energy. Making offshore wind energy now cheaper than energy from coal and other non-renewable energy sources, as seen in figure 1.2 (Anders Nymark, 2018).

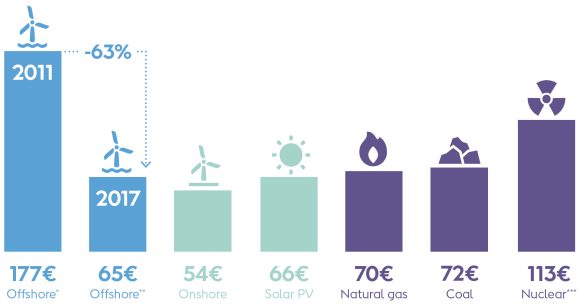

Figure 1.2: Levelised cost of energy for different energy sources in the year 2017 (Anders Nymark, 2018)

The cost for offshore wind energy decreased because of three reasons. First of all, by industrialization of the sector due to national plans and standardization, it was possible to drive down the cost of each unit (Anders Nymark, 2018).

Secondly, innovation enabled more efficient, cheap and durable components and thus wind turbines. By optimization, these components are more easily integrated into the power grid and are more reliable, reducing errors and costs (Anders Nymark, 2018).

Thirdly, upscaling of both wind turbines and wind farms reduces the cost per unit, because of the economy of scale (Anders Nymark, 2018).

The up-scaling of wind turbines and wind farms create new technological challenges. The focus of this thesis will be on the influence, of an increasing rotor diameter, on the mass of wind turbines. Increasing the rotor diameter, enables the wind turbine to generate more power. However, the increase of rotor diameter causes the torque loads to increase as shown in (1.2). This increase of torque loading increases the loads on the drivetrain of a wind turbine. Therefore, the required volume and mass of the drivetrain needs to increase to handle the torque loading. This increase of drivetrain mass brings along higher cost and poses a problem when increasings the size of wind turbines.

$$P = \omega T \tag{1.2}$$

The goal of this thesis is to define the limiting mechanisms of three offshore wind turbine drivetrains and to calculate the achievable torque densities for an increasing rotor diameter. Finding the limiting mechanisms will provide an insight in the minimal amount of drivetrain mass that is required to handle the increased torque loading. The following research questions will be answered in this thesis:

- What are the limiting mechanisms of the three investigated drivetrain types?
- What are the achievable torque densities for the three investigated drivetrain configurations for large wind turbine rotor diameters?

The hypothesis of this thesis is that the torque density potential of a hydraulic drivetrain configuration is higher than that of the gearbox drivetrain and direct drivetrain when increasing the rotor diameter and is based on empirical data obtained from existing drivetrain systems.

The results of this thesis are obtained by performing extensive literature research on the different drivetrain configurations and their design. Furthermore, a model is designed to calculate the mass of the three different drivetrains for an increasing rotor diameter. The final result is a comparison between the different drivetrains on their limiting mechanisms and torque density.

This thesis will focus on drivetrains that are being used in upwind horizontal axis wind turbines. A steady wind profile, a constant tip speed ratio and capacity factor are assumed and therefore dynamic loads on the drivetrains are not taken into account. The only parameter that is changing the loads on the drivetrain is the increase of the wind turbine rotor diameter.

To obtain the desired result the first step is to accurately define the three drivetrain configurations. The results are shown in section 2.1 and more elaborately in appendix B.The second step is to define the limiting mechanisms for each of the three drivetrain setups. This is discussed for each drivetrain setup in respectively sections 3.3, 5.3 and 4.3. The third step consists of calculating the required volume and mass of the drivetrains for an increase in rotor diameter. With this data the torque density of the three drivetrain setups can be calculated as shown in (1.3). Note that a high torque density means that the machine can handle more torque per unit mass.

$$T_d = \frac{T}{M} \tag{1.3}$$

The fourth and last step, is to compare the drivetrains on their limiting mechanisms and their torque density and present the conclusion.

2 Wind turbine drivetrain design and selection

The drivetrain of a wind turbine is the place where the rotational kinetic energy from the shaft driven by the wind, is transformed into usable electricity. The drivetrain is therefore an essential part of the wind turbine. Currently, there are roughly two commercially available drivetrain categories and one experimental drivetrain configuration. The gearbox drivetrain shown in figure 2.1 and the direct drivetrain shown in figure 2.2 are both commercially available. A new alternative, a drivetrain using fluid transmission, is currently researched as shown in figure 2.3 (Diepeveen et al., 2012). So, this thesis will limit the scope to research only the gearbox drivetrain, the direct drivetrain and the hydraulic drivetrain. As can be seen from figure 2.1, 2.2 and 2.3 the main difference between the three drivetrains is that the gearbox drivetrain does have a gearbox and the direct drivetrain and hydraulic drivetrain do not. In the case of the direct drivetrain the rotor is directly connected to the generator. There is no consensus in the wind industry which drivetrain is better in regards of torque density, reliability, repairability, installability and cost. As there is no standard drivetrain system yet, a lot of research is being done into drivetrain design. Making a drivetrain lighter, more efficient or more reliable will directly effect the LCOE of the wind turbine. In section 2.1 the drivetrain design selection is further eleborated upon. A justification will be given for choosing the three particular drivetrain configurations that will be researched in the rest of this thesis.

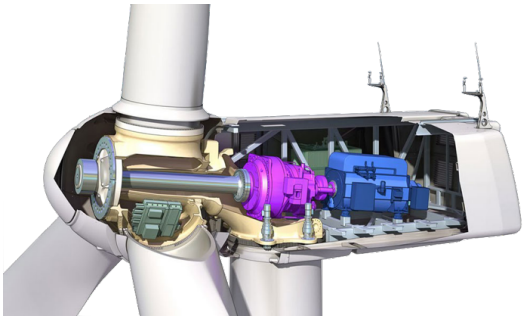

Figure 2.1: Gearbox Drivetrain (Wenzel, 2014)

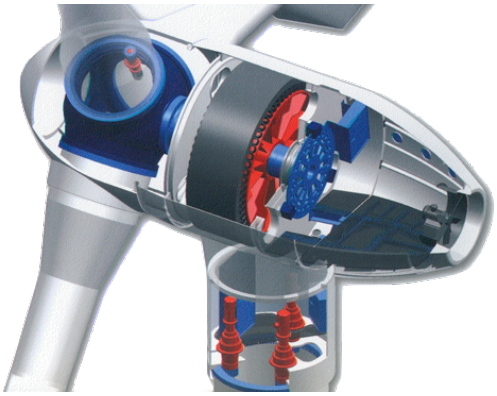

Figure 2.2: Direct drive drivetrain (Jensen et al., 2012)

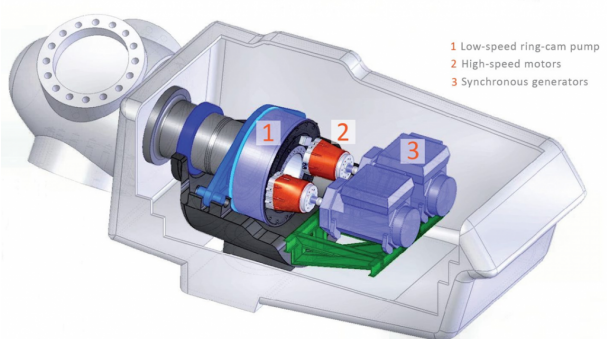

Figure 2.3: Drivetrain using a hydraulic pump as fluid transmission (ENERGY, 2014)

As can be seen in figure 2.4, drivetrains can be sudivided into three categories using a gearbox transmission, a direct transmission and a fluid transmission. The gearbox transmission drivetrains have many different configurations. Two categories that are being shown in figure 2.4 are the gearbox transmission with high speed generator and low speed generator. In the first configuration a high gear ratio is necessary to full fill the high rated angular speed of the generator. For the medium speed speed generator a lower gear ratio is required because the generator requires a lower angular speed to work accordingly. More about these configurations is explained in appendix B.1. The fluid transmission category uses hydraulic fluid to transfer the power from the wind rotor to a motor that drives a generator. An explanation about this concept is given in appendix D. The direct transmisson system only uses a generator to generate electricity. Roughly two types of direct drive transmissions are available on the market one with permanent magnets and one with electrically excited magnets. These systems are further explained in appendix C. Note that for an objective comparison the mass of the power generating components in the nacelle is included in the mass calculations. This means that for the gearbox the mass of a permanent magnet high speed generator is included in the calculations.

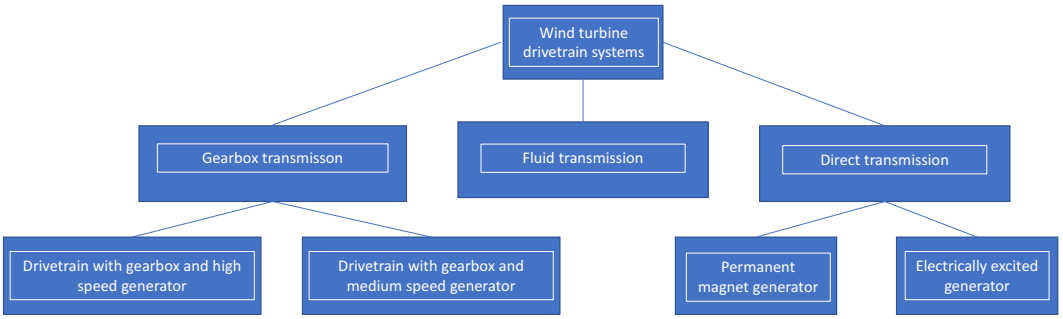

Figure 2.4: Chart for different wind turbine drivetrain designs

2.1 Description of the researched wind turbine drivetrain types

To ensure relevance and actuality of this thesis, the two most common commercially available offshore drivetrain configurations will be chosen and will be compared for their optimal torque density together with the non commercially available innovative hydraulic drivetrain. In sections B.2 and C.4 the common types of drivetrains with gearboxes and generators are described.

The following configuration will be chosen for the drivetrain with gearbox: a three stage gearbox with two planetary stages and one parallel stage with a high speed permanent magnet synchronous generator and full converter. This configuration is suitable for 5> MW wind turbines. MHI Vestas uses this configuration for its 9 & 10MW offshore wind turbines (Vestas, 2018). This configuration was chosen with the information presented in section B.1. Note that for the mass calculations, the mass of a high speed generator is included.

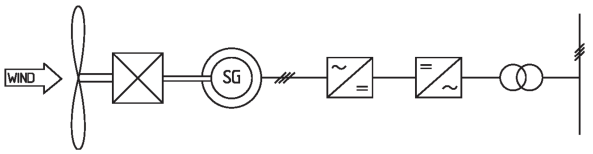

Figure 2.5: The offshore gearbox drivetrain with three stage, two planetary, one paralel gear configuration with full converter, used in this thesis (Hau and von Renouard, 2003)

Based on the most common commercially available direct drivetrain technology currently used the following direct drive configuration has been chosen: a radial flux permanent magnet synchronous generator with full converter. Amongst other wind turbines this configuration is used in Siemens's 8MW offshore wind turbine the SG 8.0-167 DD (Siemens, 2018). A more elaborate explanation on the radial flux permanent magnet generator can be found in appendix C.

Figure 2.6: The offshore direct drivetrain configuration with full converter used in this thesis (Hau and von Renouard, 2003)

In figure 2.7 from Polinder, Henk, a comparison is made for four generator types on their strengths and weaknesses. The two chosen generator concepts described in the paragraphs above are indicated as gearbox full converter (GFC) and direct drive generator (DD). Furthermore, not having a gearbox is increasing the reliability of the system (Polinder, Henk).

TABLE II
COMPARISON OF FOUR WIND TURBINE GENERATOR CONCEPTS,
+: STRENGTH, - WEAKNESS.

		CS	DFIG	GFC	DD
Cost, size and weight		+	+/-	+/-	-
Suitability for 50 and 60 Hz grid		-	-	+	+
Audible noise from blades		-	+	+	+
Energy yield	Variable speed	-	+	+	+
	Gearbox	-	-	-	+
	Generator	+	+	+	-
	Converter	+	+/-	-	-
Reliability and maintenance	Brushes	+	-	+	- (PM: +)
	Gearbox	-	-	-	+
	Mechanical loads	-	+	+	+
	Complexity	+	-	-	-
Power quality	'Flicker'	-	+	+	+
	V&f control possible	-	+	+	+
	Harmonics	+	-	-	-
Grid faults	Fault currents	+	-	-	-
	Fault ride-through	+	+/-	+	+
	Restoring voltage	-	+/-	+	+

Figure 2.7: Strength & weaknesses of generator designs (Polinder, Henk)

The third drivetrain configuration that will be researched for its optimal torque density is a hydraulic pump. In this thesis a radial piston pump is chosen for its high torque ability and low revolutions per minute (RPM). The design of the pump is assumed to be similair to the desing of a Hägglunds motor. The Hägglunds motor uses oil as hydraulic fluid and the wind rotor is attached to the cylinder block through the shaft directly. A cross section of a Hägglunds engine is presented in figure 2.8.

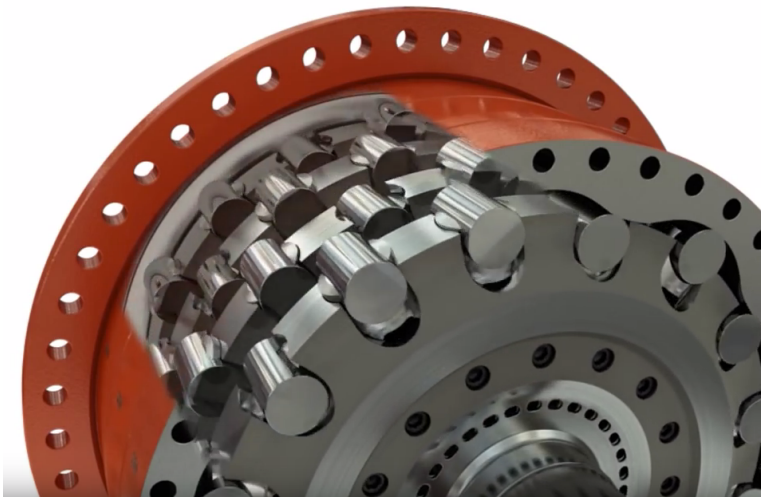

Figure 2.8: The Hagglunds pump (Group, 2018)

2.2 Wind turbine parameters and definitions

In table 2.1 the parameters that are used for the the wind turbine are shown. The rotor diameter of the wind turbine will start with 50 meters corresponding to a 0.71 *MW* wind turbine and will stop at 300 meters corresponding to a 25.4 *MW* turbine. An explanation about the assumptions and the influence they have on the torque and power of the wind turbine is given in chapter 2.2.1. In this table V_{rated} is the rated wind speed, λ is the tip speed ratio given in (2.1) and ρ_{air} is the density of air. The power coefficient C_p is the power the wind turbine can obtain out of the theoretical power that can be found in the air column that passes the rotor area.

Table 2.1: Wind Turbine parameters

Symbol:	**Value:**
V_{rated}	11 [m/s]
λ	7.5 [-]
ρ_{air}	1.2 kg/mˆ3
C_p	0.45 [-]
D_{begin}	50 [m]
D_{end}	300 [m]

2.2.1 Wind turbine rotor assumptions

As in any model assumptions are made in order to perform calculations. First of all the decision is made to keep the tip speed ratio (λ) constant.

$$\lambda = \frac{\omega \cdot R}{V_{wind}} \tag{2.1}$$

As can be seen in (2.1) this assumption makes it possible to calculate the rotational speed of the wind turbine rotor for an increase in rotor diameter when the wind speed is known. Fixed tip speed ratio wind turbines are possible by changing the pitch angle of the wind turbine blades as described in appendix A.

Secondly, a fixed wind speed is assumed in order to objectively compare the increase in mass by only one variable, the rotor diameter.

These two assumptions lead to a wind rotor that increases in diameter and therefore the angular speed ω declines. Increasing the rotor diameter has an increasing influence on the torque of the wind turbine shaft. If no losses are assumed the power of the the system will stay constant because both torque and angular speed increase and decrease linearly with increasing rotor diameter. The power of a wind turbine rotor P_{rated} is related to the rotor diameter D by the following equations (2.2), (2.3) and (2.4).

$$A_{swept} = 0.25\pi D^2 \tag{2.2}$$

$$P_{air} = 0.5\rho_{air} A_{swept} V_{rated}^3 \tag{2.3}$$

$$P_{rated} = C_p P_{air} \tag{2.4}$$

The angular speed is calculated by rearranging (2.1) to equation (2.5). The torque of the rotor can than be calculated with (2.6).

$$\omega = \frac{\lambda V_{rated}}{r} \tag{2.5}$$

$$T = \frac{P_{rated}}{\omega} \tag{2.6}$$

As can be seen in figure 2.9. The power of the wind turbine increases roughly 35 times while the angular velocity of the rotor is decreasing 6 times over the rotor diameter. The reason for the decrease in angular velocity is the fixed tip speed ratio as shown in (2.5). Rewriting (2.6) shows that the torque will increase 213 times.

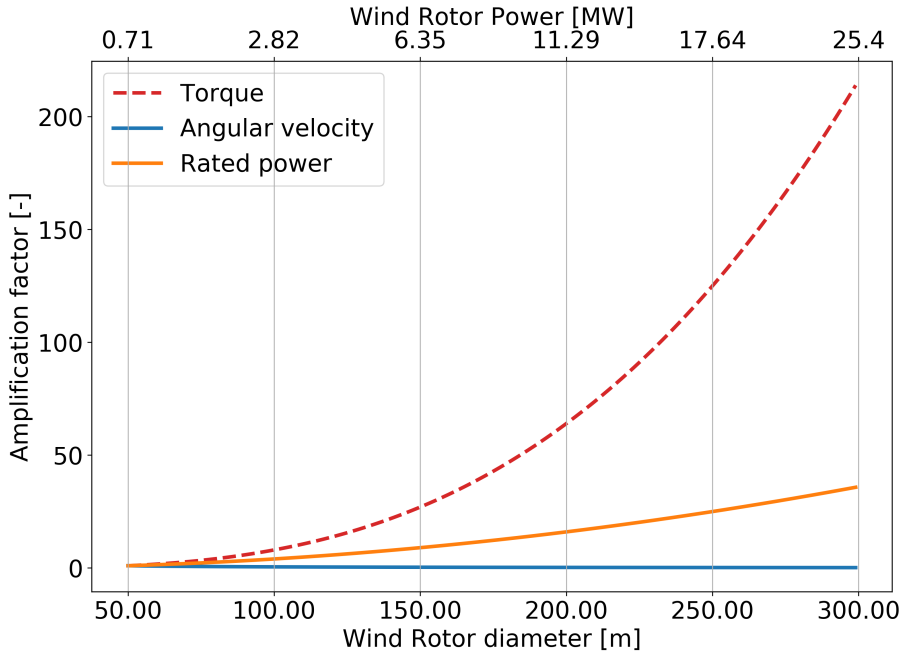

Figure 2.9: Amplification factor of torque, angular velocity and rotor power

The relation between torque and rotor diameter can be derived as shown in (2.7). With C_1 as a constant and given by equation 2.8.

$$T = C_1 D^3 \tag{2.7}$$

$$C_1 = \frac{C_p \rho_{air} \pi V_{rated}^2}{16\lambda} \tag{2.8}$$

3 Wind turbine drivetrain with gearbox transmission

3.1 Introduction

In this chapter the potential torque density of a gearbox based drivetrain as described in section 2.1 will be evaluated and calculated. The calculation method that will be used is described in Roos and Spiegelberg (2005). The most essential equations and methods will be given and explained in this chapter, after which, the results will be presented. The content of this chapter is presented in figure 3.1.

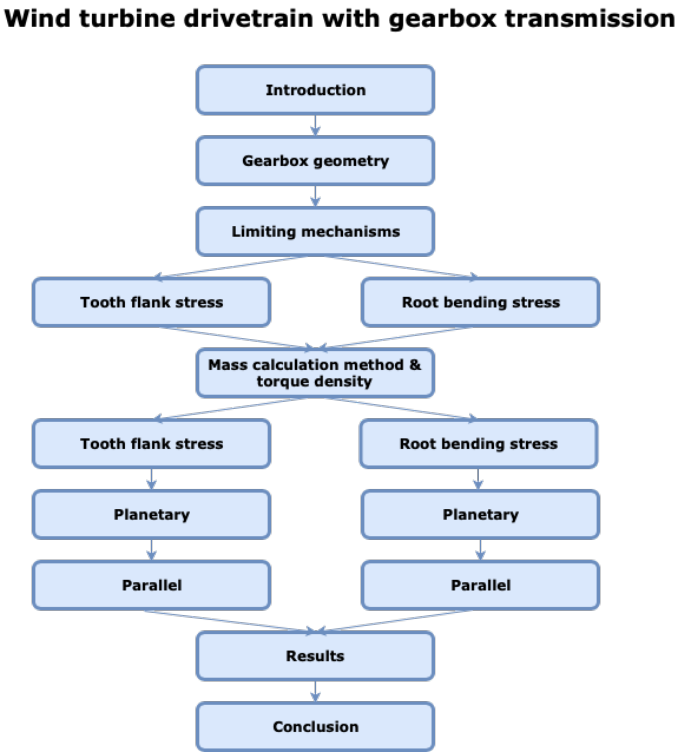

Figure 3.1: Gearbox chapter content overview

The purpose of a gearbox is to provide a high angular speed on the output shaft, from a low angular speed input shaft. This way a high speed generator can be used to generate electricity while the power is provided by a low angular speed wind rotor. A more elaborate explanation can be found in appendix B.1. In the next chapter the geometry of the gearbox is relevant, because it influences the load division and therefore the mass of the drivetrain.

3.2 Geometry of a wind turbine gearbox with high speed generator

In figure 3.2, the gearbox configuration that will be used for the calculations is presented. Note that the first two stages (leftside) of the gearbox are planetary and the third stage (right) is parallel. As can be expected, the resulting dimensions and therefore the calculation methods differ between the planetary stages and the parallel stages. The different methods will be described in sections 3.2.1 and 3.2.2.

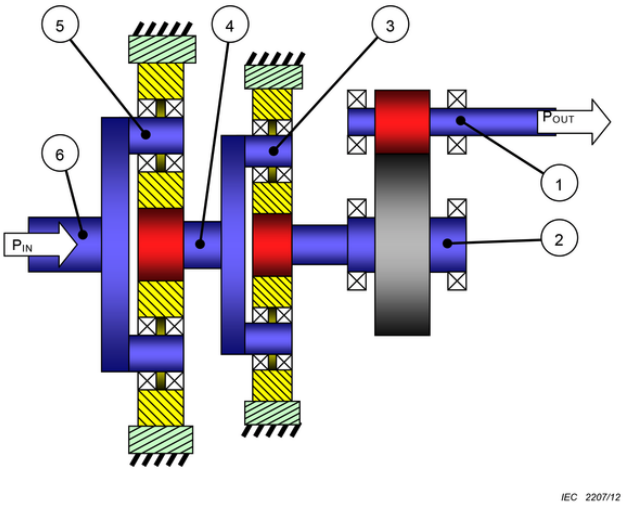

Key

1	HSS	High-speed shaft
2	HS-IS	High-speed intermediate shaft
3	IS-PS	Intermediate-speed planet shaft
4	ISS	Intermediate-speed shaft
5	LS-PS	Low-speed planet shaft
6	LSS	Low-speed shaft
P_{IN}		Power input
P_{OUT}		Power output

Figure 3.2: Researched gearbox configuration (International Organization for Standardization, 2012)

3.2.1 The design of planetary gearbox stages

The first and second stage of the gearbox are shown in figure 3.3. As can be seen in the figure, the ring of the gearbox is fixed. The planetary gears, driven by the planet carrier will rotate inside of the ring and will drive the sun gear. Note that the planet carrier has a high torque and low RPM and the sun gear will have low torque and high RPM. The rotation of the planet carrier and sun gear is the same.

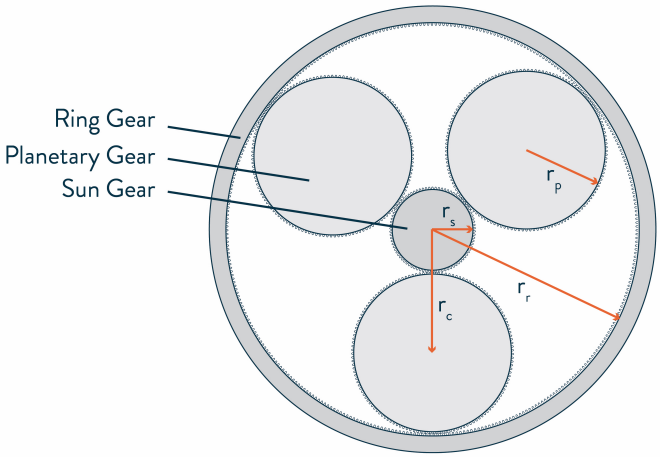

Figure 3.3: Cross section of the first and second planetary stages

In this model the pitch radius of the gear ring r_r is assumed to be known and constant. With the gear ring pitch radius known, it is possible to calculate the sun pitch radiusr_s, the planet pitch radiusr_p and the carrier radius r_c with (3.1), (3.2) and (3.3).

$$r_s = \frac{r_r}{(n-1)} \tag{3.1}$$

$$r_p = \frac{r_r - r_s}{2} \tag{3.2}$$

$$r_c = r_s + r_p \tag{3.3}$$

In (3.1), n is the required gear ratio for the stage. Note that in this thesis the gear ratio is defined as output speed over input speed. The number of teeth for the ring z_r, the planet z_p and the sun z_s, can be calculated when the module m is known. Where m is the module size of the gear tooth.

$$z_r = \frac{2 \cdot r_r}{m} \tag{3.4}$$

$$z_s = \frac{z_r}{n-1} \tag{3.5}$$

$$z_p = \frac{2 \cdot r_p}{m} \tag{3.6}$$

The incoming torque in the first stage is generated by the torque of the wind rotor. The torque is split over the planets by the planet carrier, after which the torque is transferred to the sun gear. The torque of the sun gear T_s can be calculated with (3.7).

$$T_s = \frac{T_{rotor}}{n} \tag{3.7}$$

The peripheral forces on the sun and planet F_p and carrier F_c gears are given by (3.8) and (3.9). In this equation N_p represents the number of planetary gears that is used.

$$F_p = \frac{T_s}{N_p \cdot r_s} \tag{3.8}$$

$$F_c = \frac{2 \cdot T_s}{N_p \cdot r_s} \tag{3.9}$$

Lastly the gear ratios for the planet ring interaction u_{pr} and planet sun interaction u_{ps} can be calculated as shown in (3.10) and (3.11).

$$u_{pr} = \frac{r_r}{r_p} \tag{3.10}$$

$$u_{ps} = \frac{r_p}{r_s} \tag{3.11}$$

3.2.2 The design of parallel gearbox stages

For the third stage of the planetary gear the relations are a lot more simple. Note, that since we require a high angular rotational speed at the generator side of the drivetrain, the high speed generator shaft is connected to the pinion gear of the third stage. The gear wheel of the third stage is connected by a shaft to the sun of the second planetary stage. A cross section with the crucial parameters can be seen in figure 3.4.

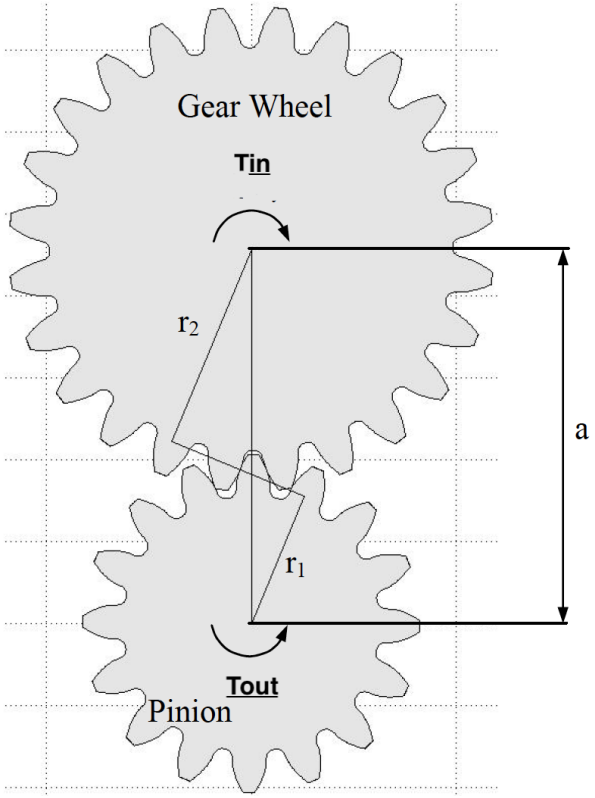

Figure 3.4: Cross section of third parallel gearbox stage (Roos and Spiegelberg, 2005)

The gear ratio of the third stage is calculated with the known gear pitch radiusr_{gear} and pinion pitch radiusr_{pinion} as shown in (3.12). Furthermore, the distance from the centre of the pinion to the centre of the gear a is calculated in (3.13). The outgoing torque T_{out} can be calculated, with (3.14) assuming a 100 % efficiency. Lastly, the amount of teeth of the pinion z_{pinion} is given by equation (3.15).

$$u_{gear} = \frac{r_{gear}}{r_{pinion}} \tag{3.12}$$

$$a = r_{gear} + r_{pinion} \tag{3.13}$$

$$T_{out} = \frac{T_{in}}{u_{gear}} \tag{3.14}$$

$$z_{pinion} = \frac{2 \cdot r_{pinion}}{m} \tag{3.15}$$

3.3 The limiting mechanisms of a gearbox transmission

Before being able to calculate the torque density of the gearbox drivetrain configuration presented in figure 3.2, it is necessary to find the limiting mechanisms of the gearbox drivetrain system.
The limiting mechanisms that can be defined in a gearbox stage while being loaded are the maximum allowable stress at the tooth flank and the root bending stress as stated in Roos and Spiegelberg (2005). The allowable stress at the tooth flank is calculated by using the theory developed by Heinrich Hertz describing the stress that occurs between two elastic curved objects (Radzevich, 2012). The locations of the two limiting mechanisms and their stress profiles are shown in figure 3.5.

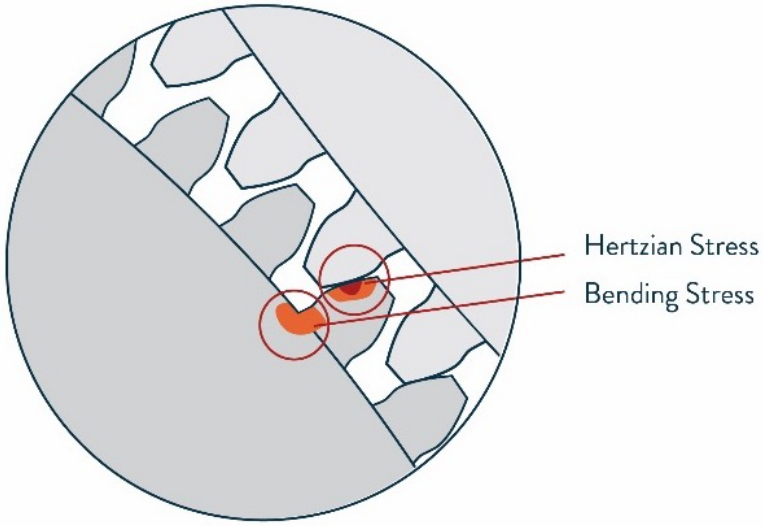

Figure 3.5: Hertz and root bending stress locations on gear teeth (Tobie et al., 2017)

3.3.1 Tooth flank stress as limiting mechanism

In this chapter the Hertzian stress theory will be used to calculate the minimal required width of the two planetary stages as well as calculating the minimal required width of the third parallel gear stage. To achieve this, (3.20) is used. This equation is specifically used for calculating the Hertz stress caused by gear teeth interaction at the contact area (International Organization for Standardization, 2012).
Tooth flank failure occurs when the repeated loading of one gear tooth by the other exceeds the Hertzian stresss limit of the tooth. An example of tooth flank failure is shown in figures 3.6 and 3.7. As can be seen in (3.23), the amount of Hertzian stress that the tooth can handle is determined by the maximum tooth flank pressure. Increasing this material property will lead to a smaller tooth width as shown in (3.23). For case carburized gears a maximum tooth flank pressure σ_{Hmax} of 1.72 GPa can be found in Radzevich (2012).

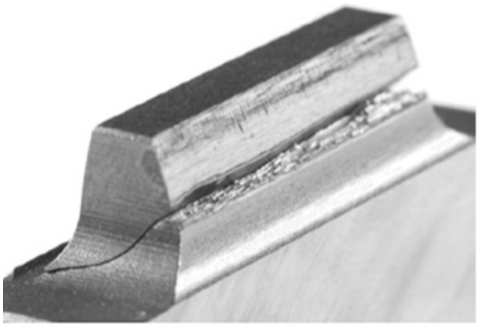

Figure 3.6: Tooth flank fracture (Boiadjiev et al., 2014)

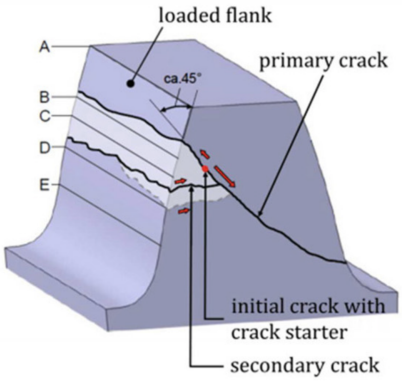

Figure 3.7: Tooth flank fracture (Boiadjiev et al., 2014)

3.3.1.1 Planetary gear stage width calculation

In equation (3.20), Z_H is the form factor, Z_M is the material factor and Z_ε is the contact factor. Furthermore, $K_{H\alpha}$ and $K_{H\beta}$ are respectively describing the division of load between the teeth and the load distribution on each individual tooth (Roos and Spiegelberg, 2005) and α is the pressure angle. The values that are assumed for these parameters are respectively 1 and 1.3 (International Organization for Standardization, 2012). The maximum compressive pressure that the tooth can handle σ_{Hmax} is found to be 1.724 GPa (Radzevich, 2012). Lastly, u is the gear ratio between two gears, b is the gear width and d_1 is the gear reference diameter. The above mentioned variables are calculated in equations (3.17) and (3.18).

$$Z_H = \sqrt{\frac{2 \cdot cos(\beta_b)}{sin(2 \cdot \alpha_t)}} \tag{3.16}$$

Since, for spur gears the transverse pressure angle α_n is equal to α_t, the symbol α will be used for the pressure angle from now on (Roos and Spiegelberg, 2005). Furthermore, the helix angle is zero on the pitch cylinder which results in $cos(\beta_b)$ = 1. Now, Z_H can be simplified to (3.17).

$$Z_H = \sqrt{\frac{2}{sin(2 \cdot \alpha)}} \tag{3.17}$$

Z_M is calculated by (3.18) with μ_1 & μ_2 being the poisson ratio of the gear and pinion and E_1 & E_2 being the E-moduli of the gear and pinion. In the case of planetary gears the gear will be represented by the planet and the pinion will be represented by the sun.

$$Z_M = \sqrt{\frac{2}{\pi(\frac{1-\nu_1^2}{E_1} + \frac{1-\nu_2^2}{E_2})}} \tag{3.18}$$

The contact factor Z_ε is given by equation (3.19). It is important to note that this contact factor differs between the different gear configurations.

$$Z_\varepsilon = \sqrt{\frac{4-\varepsilon_\alpha}{3}} \tag{3.19}$$

The contact ratio $\varepsilon\alpha$ for a sun-planet gear pair and a ring-planet gear pair is derived in (Roos and Spiegelberg, 2005).
It is now possible to find the gear width b for the sun-planet contact and ring-planet contact by rewriting equation (3.20) and inserting ε_α.

$$\sigma_H = Z_H \cdot Z_M \cdot Z_\varepsilon \sqrt{\frac{F_{cal} \cdot K_{H\alpha} \cdot K_{H\beta}(u+1)}{b \cdot d_1 \cdot u}} \tag{3.20}$$

For the sun planet configuration, (3.21) is obtained while for the ring planet configuration (3.23) is obtained. The exact derivation can be found in Roos and Spiegelberg (2005).

$$b_{SP} = \frac{Z_H^2 Z_M^2 Z_\varepsilon^2 K_{H\alpha} K_{H\beta} \frac{T_{out}(n-1)^2}{6(n-2)\sigma_{Hmax}^2}}{r_r^2} \tag{3.21}$$

The sun planet equations can be simplified as shown in (3.22).

$$b_{SP} = \frac{Z_H^2 Z_{M^2} K_{H\alpha} K_{H\beta}}{6 r_r^2 \sigma_{Hmax}^2} \frac{T_{out}(n-1)^2 Z_\varepsilon^2}{(n-2)} \tag{3.22}$$

The ring planet equations can be simplified as shown in (3.24).

$$b_{RP} = \frac{Z_H^2 Z_M^2 Z_\varepsilon^2 K_{H\alpha} K_{H\beta} \frac{T_{out}(n-1)}{6(n-2)\sigma_{Hmax}^2}}{r_r^2} \tag{3.23}$$

$$b_{RP} = \frac{Z_H^2 Z_{M^2} K_{H\alpha} K_{H\beta}}{6 r_r^2 \sigma_{Hmax}^2} \frac{T_{out}(n-1) Z_\varepsilon^2}{(n-2)} \tag{3.24}$$

Since the required width of a planetary gear stage is now known, it is possible to calculate the mass of a planetary gear stage. The method for the mass calculation will be presented in chapter 3.4. Note that in order to design a planetary gear stage that complies with the tooth stresses of the ring, planet and gear, the biggest value for gear width b will be chosen. A more thorough explanation will be provided in section 3.4.

3.3.1.2 Parallel gear stage width calculation

In this section the method used for calculating the width b of a pair of parallel spur gears is explained (Roos and Spiegelberg, 2005). The general formula for the Hertz stress is the same as for the planetary gear stage and is given in (3.20). Also the equations for Z_H, Z_M, Z_ε are the same for the planetary gear and therefore given by (3.17), (3.18), (3.19). However, the contact ratio ε_α is different from that of the planetary gear as shown in and the derivation is described in (Roos and Spiegelberg, 2005).

With (3.15) and (3.12) and the chosen pressure angle α it is possible to calculate the contact ratio. The torque T_{out} can be calculated with (3.14) and the center to center distance a with (3.13). Since all the parameters are now known, the required width for the parallel gear can also be calculated.

$$b = \frac{Z_H^2 Z_M^2 Z_\varepsilon^2 K_{H\alpha} K_{H\beta} \frac{T_{out}(u+1)^3}{2u^2 \sigma_{Hmax}^2}}{a^2} \tag{3.25}$$

Equation (3.25) can be further simplified to (3.26) by rearranging for all the constants.

$$b = \frac{Z_H^2 Z_M^2 K_{H\alpha} K_{H\beta}}{2a^2 \sigma_{Hmax}^2} \frac{T_{out}(u+1)^3 Z_\varepsilon^2}{u^2} \tag{3.26}$$

3.3.2 Root bending stress as limiting mechanism

As could be seen in figure 3.5, Hertzian stresses are not the only limiting mechanism of a gear stage. The general equation for the root bending stress can be found to be (3.27) (Roos and Spiegelberg, 2005).
The root bending stress of a gear tooth is caused by a normal force pressing against the tooth flank with a arm to the root of the tooth as shown in figure 3.8. As can be seen in (3.30), the required width of a gear depends on the flexural strength of the material σ_{Fmax}. A value of 0.24 [GPa] can be found for carburized gears (Gears, 2011). A higher value for the flexural strength will result in a lower gear width requirement.

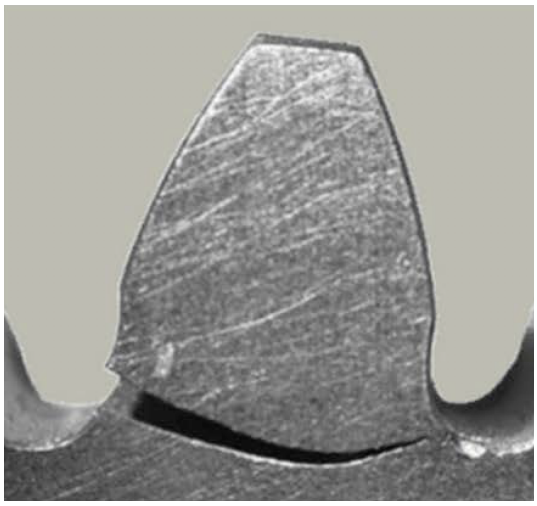

Figure 3.8: Root bending stress fracture of gear tooth (Boiadjiev et al., 2014)

$$\sigma_F = Y_F Y_\beta Y_\varepsilon \frac{F_{cal} K_{F\alpha} K_{F\beta}}{bm} \tag{3.27}$$

As can be noticed (3.27) is different from the general Hertz Stress equation with a few new unknowns. The form factor Y_F is calculated as shown in (3.28) (Roos and Spiegelberg, 2005). The helix angle factor Y_β can be found to be 1 for spur gears and the contact ratio factor Y_ε is calculated in (3.29). Furthermore, according to International Organization for Standardization (2012), the load division factor $K_{F\alpha}$ and $K_{F\beta}$ can be found to be respectively 1 and 1.3.

$$Y_F \approx 2.2 + 3.1e^{-z/14} \tag{3.28}$$

$$Y_\varepsilon = \frac{1}{\varepsilon_\alpha} \tag{3.29}$$

3.3.2.1 Planetary gear stage width calculation

The required gear width b, that is necessary to comply with the root stress that is acting on the gears, can be calculated with (3.30). Note that the root bending stress form factor Y_F for the sun and planet is given by (3.28), but for the ring planet configuration it is given by a value of 2.06 (Roos and Spiegelberg, 2005). Variable N_p, represents the number of planets in the planetary stage. Separating the variables and the constants in the equations renders 3.31.

$$b = \frac{Y_F Y_\beta Y_\varepsilon K_{F\alpha} K_{F\beta} \frac{1}{N_p} \frac{T_s (n-1)^2 z_s}{2n\sigma_{Fmax}}}{r_r^2} \tag{3.30}$$

$$b = \frac{Y_F Y_\beta Y_\varepsilon K_{F\alpha} K_{F\beta}}{r_r^2 N_p \sigma_{Fmax} 2} \frac{T_s (n-1)^2 z_s}{n} \tag{3.31}$$

3.3.2.2 Parallel gear stage width calculation

For the parallel gear stage the contact ratio ε_α is calculated in the same way as was done for the planetary gear. Width (3.32), it is now possible to calculate the gear width of the third parallel gear stage. The full derivation for this equation can be found in Roos and Spiegelberg (2005). Separating the variables and the constants in the equations renders 3.33.

$$b = \frac{Y_F Y_\beta Y_\varepsilon K_{F\alpha} K_{F\beta} \frac{T_{pinion} z_{pinion} (u+1)^2}{2u\sigma_{Fmax}}}{a^2} \tag{3.32}$$

$$b = \frac{Y_F Y_\beta Y_\varepsilon K_{F\alpha} K_{F\beta}}{2a^2 \sigma_{Fmax}} \frac{T_{pinion} z_{pinion} (u+1)^2}{u} \tag{3.33}$$

Note that the limiting mechanisms that requires the largest width b for a gear stage will be chosen as limiting. This only holds if the assumption is made that, in the case of a planetary gear, the planet, sun and ring will have the same width for that particular gear stage.

3.4 Calculation method for the gearbox volume & mass

Since all the necessary geometry and properties of the gears can now be obtained, it is possible to calculate the mass of the gears. The mass calculation of the gears is performed according to the method presented in Roos and Spiegelberg (2005). Again, the gears are assumed to be cylinders for the mass calculations. In (3.34), (3.35), (3.36), (3.37), the mass of respectively the pinion M_{pinion}, gear M_{gear}, sun M_s and planet Mp are given.

$$M_{pinion} = r_{pinion}^2 \pi b \rho \tag{3.34}$$

$$M_{gear} = r_{gear}^2 \pi b \rho \tag{3.35}$$

$$M_s = r_s^2 \pi b \rho \tag{3.36}$$

$$M_p = r_p^2 \pi b \rho \tag{3.37}$$

In order to calculate the mass of the ring M_r, the thickness of the ring scales with the diameter of the ring as shown in 3.38.

$$M_r = (r_{ro}^2 - r_r^2) b \pi \rho \tag{3.38}$$

The assumption is made that the width of the carrier is equal to the necessary with of the gears. Furthermore, the assumption is made that the planet carrier has a cylindrical shape an can therefore be calculated with (3.40).

$$r_c = r_s + d_p \tag{3.39}$$

$$M_c = r_c^2 b_c \pi \rho \tag{3.40}$$

It must be noted that the assumption is made the the outer diameter of the ring r_{ro} is a factor r_{fac} larger than the inner diameter r_r as shown in equation (3.41).

$$r_{ro} = r_r * r_{fac} \tag{3.41}$$

The total mass of a single planetary stage will therefore be given in (3.42).

$$M_{stage} = M_s + N_p \cdot M_p + M_r + M_c \tag{3.42}$$

The mass of a parallel stage can be calculated with (3.43).

$$M_{parallel} = M_{gear} + M_{pinion} \tag{3.43}$$

To obtain the mas of the total gearbox configuration as shown in figure 3.2, (3.44) is used.

$$M_{tot} = M_{stage_1} + M_{stage_2} + M_{parallel} \tag{3.44}$$

3.5 Computational model for gearbox mass calculation on the basis of limiting mechanisms

In order to perform the calculation method that is discussed in the previous chapter a python script is used to perform the mass and torque calculations for a range of rotor diameters. A flowchart for the computational method that is used can be seen in figure 3.9. In the first section of this chapter the parameters with a short explanation will be given in tables 3.1 and 3.2. The second part of this chapter consists of explaining the assumptions that have been made while making this model.

3.5.1 Gearbox configuration parameters

The gearbox configuration parameters (3.1) and the gearbox material parameters (3.2) are split up to provide a more clear distinction between the two. The gearbox is set to a constant output velocity of 1500 RPM to ensure the compatibility with a high speed generator. To achieve a constant output velocity for an increasing rotor diameter the model changes the gearbox ratio accordingly. The $n_{factors}$ given in table 3.1 are the division factors for the gear ratio of the gearbox over the three stages. The m parameters represent the moduli of the gears.

3.5.2 Assumptions gearbox transmission

Firstly it is assumed that no friction losses appear in the gearbox stages. Therefore (3.7) is valid as is (A.3) for the rotational speed.

$$\omega_{out} = \omega_{in} \cdot n \tag{3.45}$$

In order to have a realistic gearbox the rotational output speed ω_{out} has to be constant. Therefore, a constant rotational output is assumed that complies with the properties of the generator as can be seen in chapter 3.5.1. To establish a constant generator output the gear ratio of the gearbox has to change accordingly while increasing the rotor diameter of the wind turbine. In this computational model, the gear ratio is divided over the gear stages by three factors, one for each stage. These factor have been chosen in accordance with Nejad et al. (2016b) and the values can be found in table 3.1.

Thirdly, the assumption is made that the mass of the gears can be calculated by using the reference radii instead of calculating the exact volume of all the teeth. Further mass assumptions are that the carrier is assumed to be a circular disk, the shafts between the stages are taken into account with the relation provide in Fingersh et al. (2006). The mass of the oil and housing is calculated with an assumed wall thickness and factor see table 3.1.

Table 3.1: Gearbox configuration parameters

Symbol:	**Value:**
α	20 [^{o}]
ω_{gen}	1500 [rpm]
$n_{factor1}$	0.36 [-]
$n_{factor2}$	0.43 [-]
$n_{factor3}$	0.21 [-]
r_{r1}	1.25 [m]
r_{r2}	0.8 [m]
m_1	50 [mm]
m_2	45 [mm]
m_3	30 [mm]
N_{p1}	3 [-]
N_{p2}	3 [-]
N_{p3}	1 [-]
$KH\alpha$	1 [-]
$KH\beta$	1.3 [-]
$KF\alpha$	1 [-]
$KF\beta$	1.3 [-]
$Y\beta$	1 [-]
$YFRP$	2.06 [-]
r_{fac}	1.05 [-]
b_c	1.05
oil_{fac}	1/3

Table 3.2: Gearbox material parameters

Symbol:	**Value:**
ν	0.3 [-]
ρ_{steel}	8050 [kg/m3]
E	$210 \cdot 10^9$ [Pa]
σ_{Hmax}	$1.72[GPa]$
σ_{Fmax}	$0.24[GPa]$

The total gear ratio of the entire gearbox is given in (3.46). The total gear ratio is divided over the gears with the factors displayed in table 3.1. The total gear ratio of the gearbox is divided over the gear stages as shown in equations (3.47), (3.48), (3.49).

$$i_{tot} = \frac{\omega_{gen}}{\omega_{wind}} = \frac{\omega_{gen} D}{2\lambda V_{rated}} \tag{3.46}$$

$$n_1 = \left(\frac{i_{tot} n_{factor1}}{n_{factor2} n_{factor3}}\right)^{1/3} \tag{3.47}$$

$$n_2 = \left(\frac{i_{tot} n_{factor1}}{n_{factor2} n_{factor3}}\right)^{1/3} \frac{n_{factor2}}{n_{factor1}} \tag{3.48}$$

$$n_3 = \left(\frac{i_{tot} n_{factor1}}{n_{factor2} n_{factor3}}\right)^{1/3} \frac{n_{factor3}}{n_{factor1}} \tag{3.49}$$

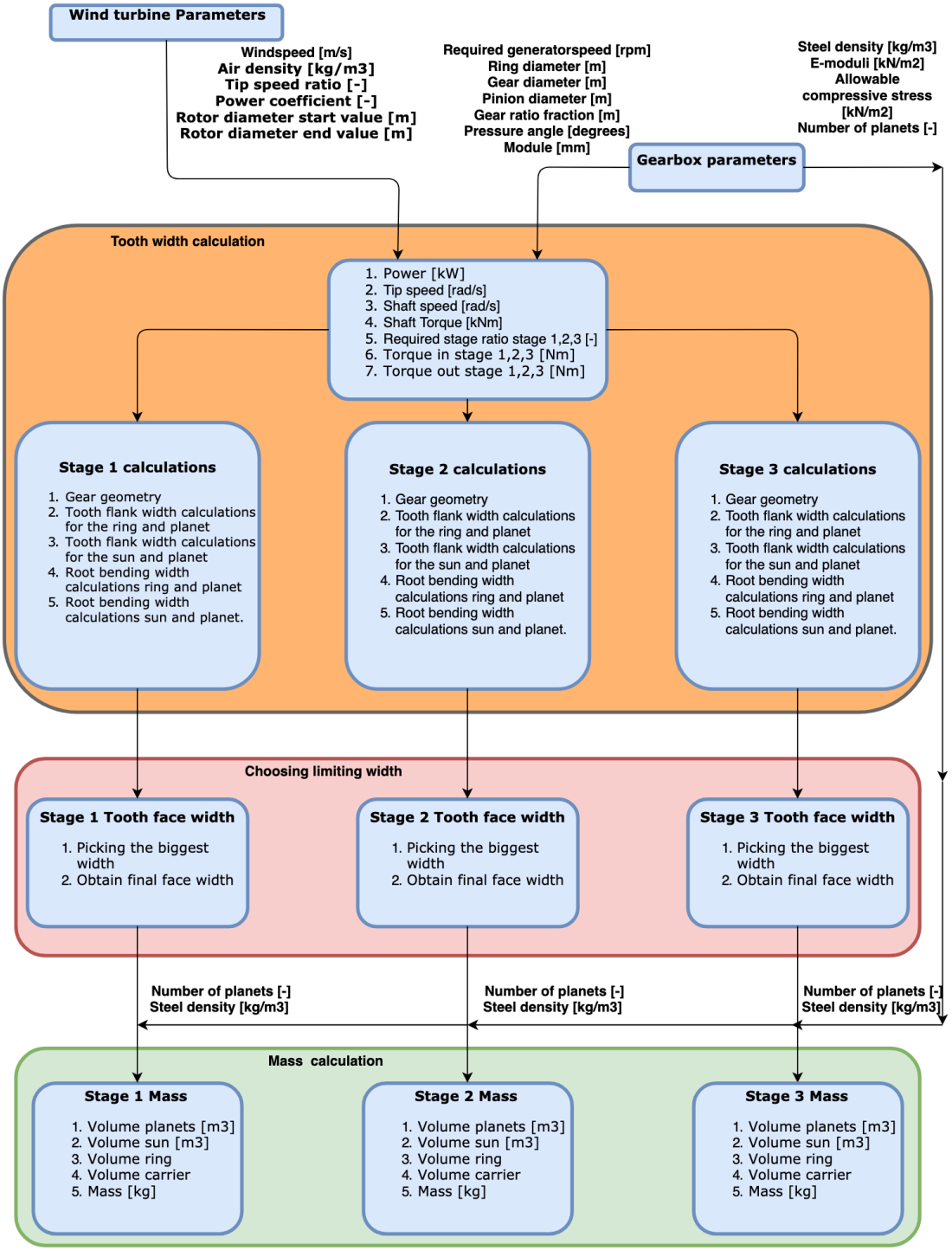

Figure 3.9: Flowchart of computational gearbox mass model

3.6 Results

3.6.1 Limiting mechanisms of a gearbox transmission

The limiting mechanisms that were identified in this chapter are the tooth flank stress and the root bending stress. For the tooth flank stress the fundamental stress mechanism is found to be the Hertz stress. The Hertz stress increases when the contact area between two teeth is decreasing as the Hertz stress is the stress per area. As described in section 3.3, the required width of the gears is determined by the maximum Hertzian pressure that can be applied to the material. According to Budynas et al. (2008) this maximum pressure P_{max} can be defined as the surface endurance limit σ_{Hmax} also known as the Hertzian endurance strength. The Hertzian endurance strength for carburized steel gears is: 1.72 GPa (Radzevich, 2012)
The root bending stress is determined by the flexural strength of the material. When a force is applied on a tooth, a moment is created in the root of the tooth. This moment is transferred in to tension at the root of the tooth, leading to stress. As the module of the tooth increases, the root area increases and therefore the allowed root bending moment can be increased. The allowed root bending stress in the tooth is determined by the flexural strength σ_{Fmax} of the material. This flexural strength for carburized steel gears is: 0.24 [GPa] (Gears, 2011).

3.6.2 Torque density of gearbox transmission

To obtain the results for the gearbox, the computational model described in chapter 3.5 is used. In figure 3.10 the gear ratio for each of the three stages is displayed. As expected the gear ratios increase as the rotor diameter increases. This is due to the assumption of a fixed tip speed ratio, that is causing the rotor speed of the wind turbine to decrease as the rotor diameter increases. Furthermore, it can be noted that the rate of increase of the gear ratios becomes less for larger rotor diameters. The total gear ratio is presented in figure 3.11. This is the multiple of the individual gear stage values. It can be concluded that for the chosen fixed tip speed ratio and high speed generator the gear ratio becomes too high. A normal gear ratio range would be in between 1:80 and 1:120 (Nejad et al., 2016b). There are two ways to solve this problem. A solution would be to change the pitch of the blades in order to increase the tip speed ratio. This will make the rotor turn faster and therefore decrease the required gear ratio. The second solution would be to use a medium speed generator that requires a lower angular velocity from the shaft exiting the gearbox.

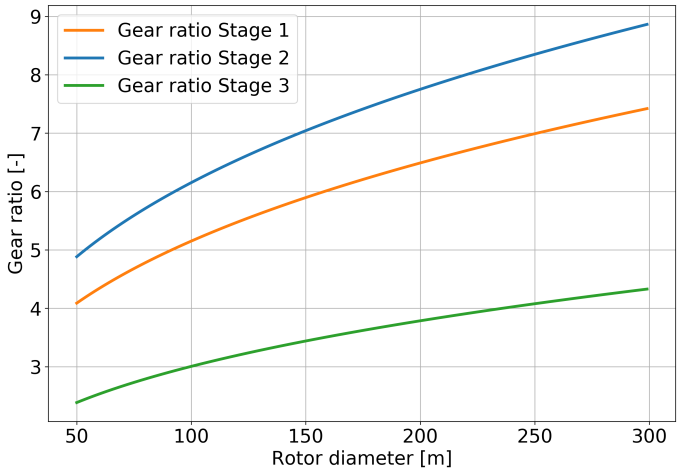

Figure 3.10: Gear ratio for each individual gear stage

Substitution of equations (3.46), (3.47), (3.48) and (3.49). Leads to the following relation with the rotor diameter as shown in equation (3.53). With the constant $C2_n$ for the three different stages as shown in (3.50), (3.51) and (3.52).

$$C2_1 = \left(\frac{\omega_{gen} n_{factor1}^2}{2\lambda V_{wind} n_{factor2} n_{factor3}}\right)^{1/3} \tag{3.50}$$

$$C2_2 = \left(\frac{\omega_{gen} n_{factor1}^3}{2\lambda V_{wind} n_{factor3} n_{factor2^2}}\right)^{1/3} \tag{3.51}$$

$$C3_2 = \left(\frac{\omega_{gen} n_{factor1}^3}{2\lambda V_{wind} n_{factor2} n_{factor3^2}}\right)^{1/3} \tag{3.52}$$

$$n_n = C2_n D^{1/3} \tag{3.53}$$

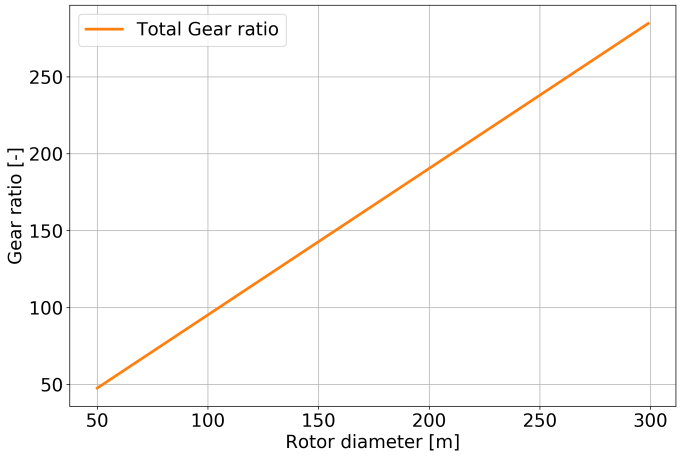

Figure 3.11: Total Gearbox ratio

The next step in the analysis of the results is to study the contact ratio ε_α shown in figure 3.12. The contact ratio is the number of teeth that is in contact with each

other when two gears meet. It is important to note that a big difference between the number of teeth of a gear pair results in a low contact ratio, whereas a similar teeth number results in a high gear ratio. Furthermore, it can be seen that the contact ratio of the ring - planet gears increases. The contact ratio of the sun - planet gears decreases. The downward gear ratio trend is the result of the increasing gearbox ratio. This is causing a dissimilarity in the number of teeth of the gear pair. For, the ring gear the amount of teeth is held constant while the number of teeth of the planet increases. This leads to a decrease between the number of teeth of the ring gear and the planet gear, resulting in an increased contact ratio.

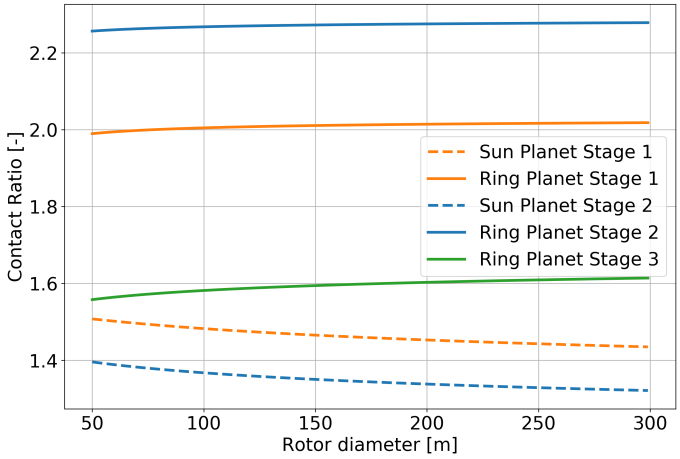

Figure 3.12: The contact ratio for all the gear teeth interactions for the three stages

In figures 3.13, 3.14, 3.15 the required gear width b can be seen. As expected the required gear width increases while the rotor diameter of the wind turbine increases. For both stage 1 and stage 2 the sun - planet gear pairs determine the width of the gears. This can be explained by the fact that a high contact ratio value has a negative effect on the contact factor as shown in (3.29) and (3.19). Whether root stress or hertz stress is the dominant limiting mechanism depends on the chosen module and ring diameter. Choosing a bigger ring diameter will result in an increase of the root stress and therefore gear width. Choosing a bigger module will result in a decrease of the root bending stress and therefore the required gear width. The main driver of the Hertz stress is the contact ratio. As mentioned before, if the contact ratio increases, the more contact area to transfer the stress between a gear pair will be present. Therefore an increase in contact ratio leads to a decrease in Hertz stress in the teeth leading to a smaller required width of the gear.

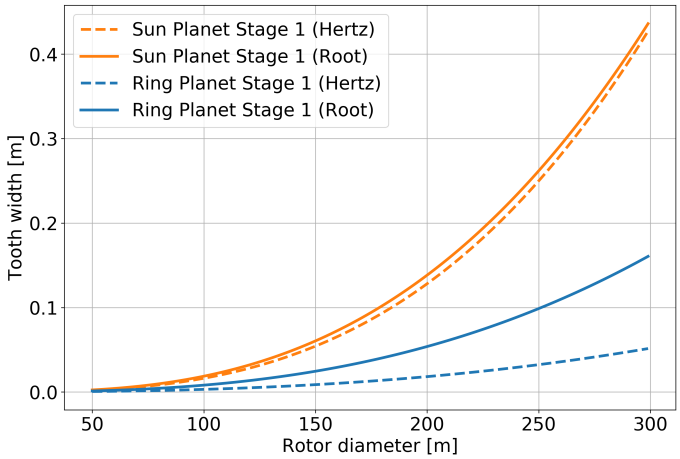

Figure 3.13: The gear width that is required to satisfy the two limiting mechanisms at two possible locations in stage 1

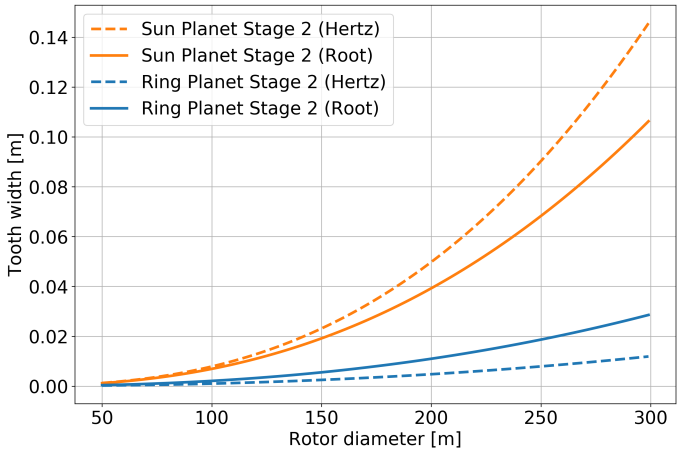

Figure 3.14: The gear width that is required to satisfy the two limiting mechanisms at two possible locations in stage 2

Equations (3.57), (3.58), (3.59) are derivations of respectively (3.22), (3.24) and (3.31), where $C3$, $C4$ and $C5$ are calculated in (3.54), (3.55) and (3.56). These equations are used for the planetary stages of the gears.

$$C_3 = \frac{Z_H^2 Z_{M^2} K_{H\alpha} K_{H\beta}}{6 r_r^2 \sigma_{Hmax}^2} \tag{3.54}$$

$$C4 = \frac{Z_H^2 Z_{M^2} K_{H\alpha} K_{H\beta}}{6 r_r^2 \sigma_{Hmax}^2} \tag{3.55}$$

$$C5 = \frac{Z_H^2 Z_M^2 K_{H\alpha} K_{H\beta}}{2 a^2 \sigma_{Hmax}^2} \tag{3.56}$$

$$b_{SP} = C_3 \frac{T_{out}(n-1)^2 Z_\varepsilon^2}{(n-2)\sigma_{Hmax}^2} \tag{3.57}$$

$$b_{RP} = C_4 \frac{T_{out}(n-1)Z_\varepsilon^2}{(n-2)\sigma_{Hmax}^2} \tag{3.58}$$

$$b = C_5 \frac{T_s(n-1)^2 z_s}{n\sigma_{Fmax}} \tag{3.59}$$

As the contact ratio factor is approximately constant, as can be seen in figure 3.12, the following relations can be found between the gear width and the rotor diameter by substituting (2.7) and (3.53) into the above equations. Equations (3.60), (3.61) and (3.62) give the relation between the rotor diameter and gear width that is necessary for a sun-planet gear, root-planet gear and parallel gear. Equation (3.60) and (3.61) are used to calculatue the width to comply with the Hertz stress and (3.62) is used to calculate the necessary sun-planet and ring-planet gear width for root bending.

$$b_{SP} = \frac{C_3 C_1 D^3 (C2_n D^{1/3} - 1)^2}{(C2_n D^{1/3} - 2)\sigma_{Hmax}^2} \tag{3.60}$$

$$b_{RP} = \frac{C_4 C_1 (C2_n D^{10/3} D^3)}{(C2_n D^{1/3} - 2)\sigma_{Hmax}^2} \tag{3.61}$$

$$b = \frac{C_5 C_1 D^3 (C2_n D^{1/3} - 1)^2}{C2_n D^{1/3}\sigma_{Fmax}} \tag{3.62}$$

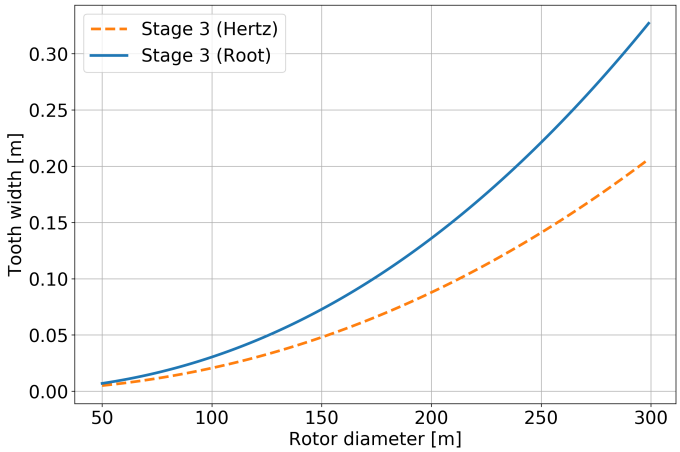

Figure 3.15: The gear width that is required to satisfy the two limiting mechanisms at two possible locations in stage 3

For the third parallel stage, (3.65) and (3.66) can be found by rearranging (3.26) and (3.33). The gear width that is required for the parallel stage that complies with the Hertz stress is given by (3.65) while the gear width that is required for the root bending stress is given by (3.66). The constants C_6 and C_7 are given by (3.63) and (3.64).

$$C_6 = \frac{Y_F Y_\beta Y_\varepsilon K_{F\alpha} K_{F\beta}}{r_r^2 N_p \sigma_{Fmax} 2} \tag{3.63}$$

$$C_7 = \frac{Y_F Y_\beta Y_\varepsilon K_{F\alpha} K_{F\beta}}{2a^2 \sigma_{Fmax}} \tag{3.64}$$

$$b = C_6 \frac{T_{out}(u+1)^3 Z_\varepsilon^2}{u^2 \sigma_{Hmax}^2} \tag{3.65}$$

$$b = C_7 \frac{T_{pinion} z_1 (u+1)^2}{u \sigma_{Fmax}} \tag{3.66}$$

Substitution of (2.7) and (3.53) shows a relation for the parallel gear width depending on the rotor diameter leading to (3.67) and (3.68).

$$b = \frac{C_6 C_1 D^3 (C2_n D^{1/3} + 1)^3}{(C2_n D^{1/3})^2 \sigma_{Hmax}^2} \tag{3.67}$$

$$b = \frac{C_7 C_1 D^3 (C2_n D^{1/3} + 1)^2}{C2_n D^{1/3} \sigma_{Fmax}} \tag{3.68}$$

Remember that the largest gear width is taken for each stage to comply with the stresses in the gear stages. Substitution of (2.7) and (3.53) into (3.2) and (3.1) gives a relation between the area of the gears for respectively the planet and sun, shown in (3.69) and (3.70).

$$A_p = \frac{1}{4}\pi (r_r - \frac{r_r}{C2_n D^{1/3} - 1})^2 \tag{3.69}$$

$$A_s = \frac{\pi r_r^2}{(C2_n D^{1/3} - 1)^2} \tag{3.70}$$

Multiplying the area with the gear width will result into the volume of the gears. As the density of the gear material is assumed to be constant a relation between the rotor diameter and mass is defined. To calculate the mass of the system, note that the high speed generator is also included. The high speed generator mass is calculated with the relation found in (Fingersh et al., 2006). In figure 3.16, the mass contribution for each individual gear stage is shown. As expected the mass of the gearbox increases as the rotor diameter of the wind turbine increases. As can be seen, stage 1 contributes the most to the mass of the gearbox after the high speed generator. This is caused by stage 1 requiring the largest gear width and having the largest ring diameter. Both factors result in a larger required volume of the stage and the volume of the cylinder increases with the power of three.

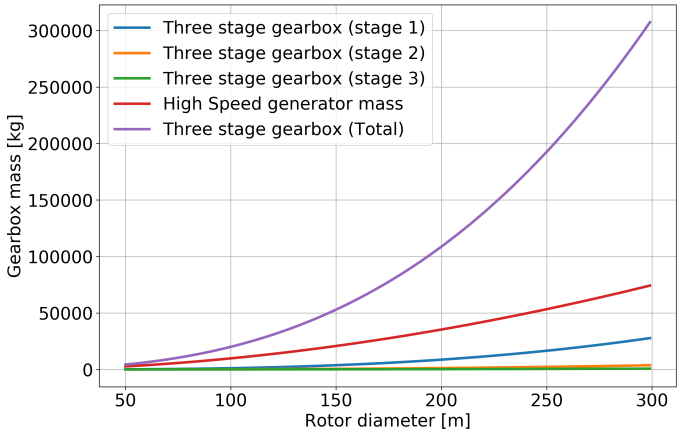

Figure 3.16: Gear stage mass

To validate the obtained results, the modelled gearbox mass is compared with the mass of a three stage, two planetary, one parallel gearbox model provided by the National Renewable Energy Lab Fingersh et al. (2006). The NREL model is based on empirical data. It must be noted that this paper was published in 2006 and therefore an extrapolation of this empirical data might give an unreliable validation. Therefore, more recent gearbox mass data is added to the model to provide a better validation.

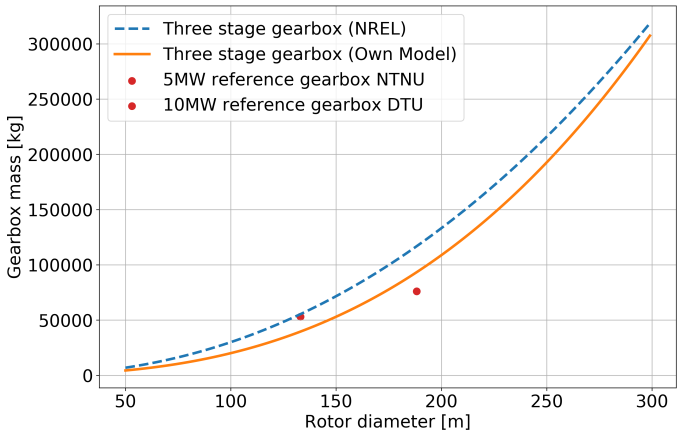

Figure 3.17: Gearbox mass compared with the NREL model

The torque density of the gearbox with the high speed generator is presented in figure 3.19. The torque density is increasing over the entire rotor diameter range, this can be explained by the torque increasing faster than the mass of the system as shown in figure 3.18. As the difference between the torque and mass is increasing, with increasing rotor diameter, so will the torque density curve. It must be noted that the rate with which the difference between mass and torque is increasing, is decreasing for larger rotor diameters, leading to the torque density to level off as shown in figure 6.7. The mass increase trend can be explained by the relations that are given in equations (3.60), (3.61), (3.62), (3.67), (3.68).

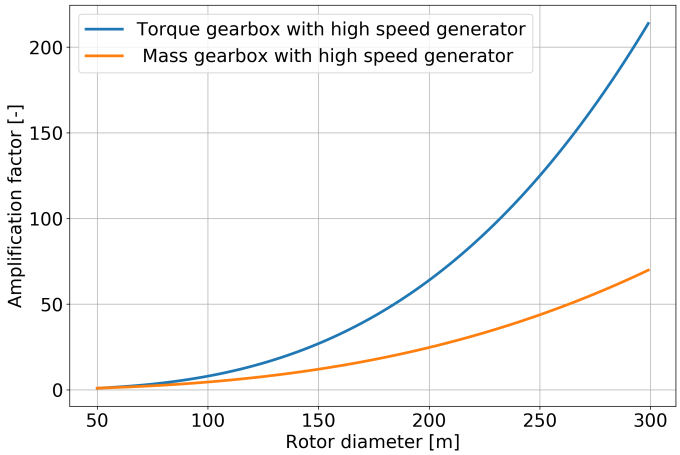

Figure 3.18: The amplification factor of the applied torque and gearbox mass

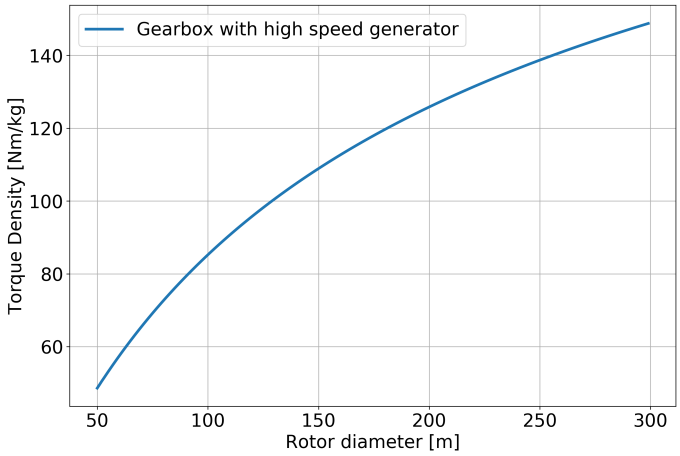

Figure 3.19: The torque density of the gearbox and high speed generator

3.7 Conclusion

3.7.1 Limiting mechanisms of a gearbox transmission

The root flank and root bending stress have been defined as the limiting mechanisms of the gearbox. The sensitivity of the gearbox model to the maximum Tooth flank stress and Root bending stress parameters is significant, therefore improving these material properties will enable the design of smaller gearboxes.
If dynamics are taken into account bearing failure could also become a limiting factor in gear design. As the horizontal forces of the wind rotor are transferred through the shaft into the gearbox, dynamic forces can cause excessive forces on the gearbox bearings.

3.7.2 Scaling model of a gearbox transmission

As can be seen in figure 3.17 the obtained results for the gearbox mass are reasonably accurate when looking at the existing validation data. The validation data was obtained from two reference gearboxes designed by the Norwegian University of Science and Technology (NTNU) (Sethuraman et al., 2017) and the Technical University of Denmark (DTU) (Nejad et al., 2016a). It must be noted that more gearbox validation data is needed to require a larger certainty of the result. Note that the mass of the gears is determined according to the method used in (Roos and Spiegelberg, 2005). In this paper the gears are assumed as homogeneous solids, however further investigation might show that less material is needed to transfer the stresses from the teeth to the shaft. A possibility for further mass reduction is then possible.

As has been mentioned in section 3.6, the gear ratio can be seen to increase over the rotor diameter and surpasses the maximum value of 120 as mentioned in (Nejad et al., 2016b) at a rotor diameter of 140 meters. Figure 3.11 shows that the chosen gearbox configuration with high speed generator is not a valid option. To solve this, the first possibility is to increase the tip speed ratio to make the rotor spin faster and therefore reduce the spinning velocity difference of the wind rotor and the generator rotor. There are several downsides to this method of which the most important one would be the decrease of fatigue life due to the higher amount of loading cycles. The second possibility is to choose a medium speed generator also reducing the required gear ratio. The disadvantage of this method is that the increase of size and therefore weight of the medium speed generator, is decreasing the torque density of the nacelle configuration.
Furthermore it can be concluded that the torque density of the drivetrain with gearbox will increase when increasing the rotor diameter. As the rotor torque increases at a higher rate than the mass of the gearbox as shown in figure 2.9. The torque density will increase but level off for larger rotor diameters. This is due to decrease of the difference between the applied torque and mass of the system for larger rotor diameters. Scaling laws have been derived to show the relation between rotor diameter and gear mass more clearly and are given by (3.60), (3.61), (3.62), (3.67), (3.68), (3.69) and (3.70).

4 Wind turbine drivetrain with direct drive generator

4.1 Introduction

The effects of the limited force density of a permanent magnet generator on the the torque density of a direct drive drivetrain configuration as described in section 2.6 will be investigated. Suggestions are made on how the mass of a generator could be reduced by improved cooling techniques or improvements of the structure. The layout of the chapter is shown in figure 4.1.

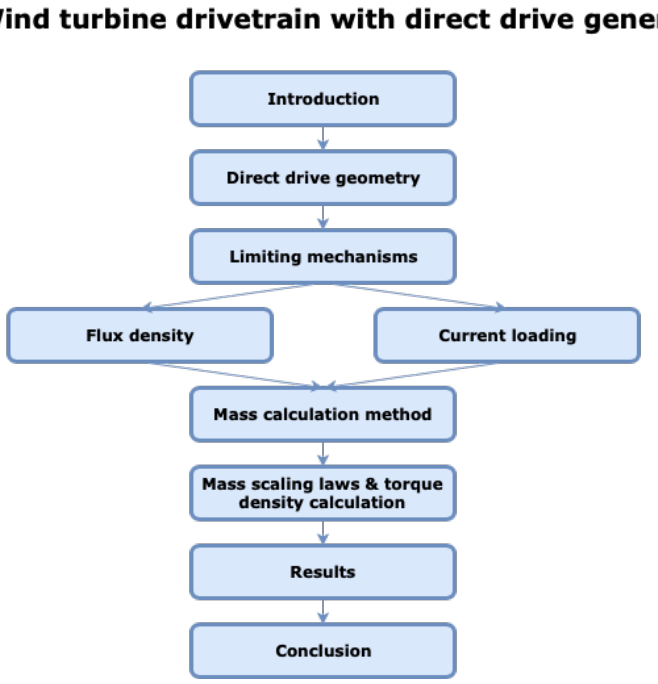

Figure 4.1: Direct drive chapter overview

4.2 Geometry of a wind turbine direct drive generator

The radial flux permanent magnet direct drive (RFPMDD) generator that will be considered in this thesis is presented in figure 4.2. More information on other generator types can be found in the appendix C. As can be seen, the generator has an inner rotor and an outer stator. The rotor of the generator is connected to the shaft of the wind turbine and therefore rotates with the same speed.

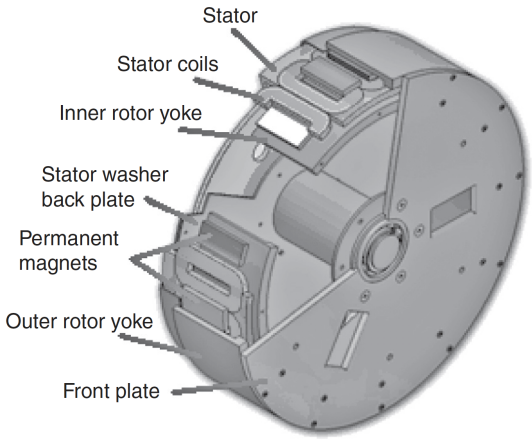

Figure 4.2: Radial flux permanent magnet generator with inner rotor and outer stator (Mueller, Markus and Polinder, Henk)

Figure 4.3 shows a cross section of the rotor and the stator. The permanent magnets are attached to the rotor while the windings or conductors are found in between the slots of the stator between the stator teeth. The permanent magnets create the magnetic field. It is important to note that for permanent magnet generators no electrical excitation is necessary to create the magnetic field. As the rotor turns, the magnetic field lines pass the windings and create a flux. Due to saturation of the stator teeth material a limit is reached for the amount of flux that can flow between the rotor and the stator. This limit is given as the flux density, representing the amount of flux that can flow through a determined area.

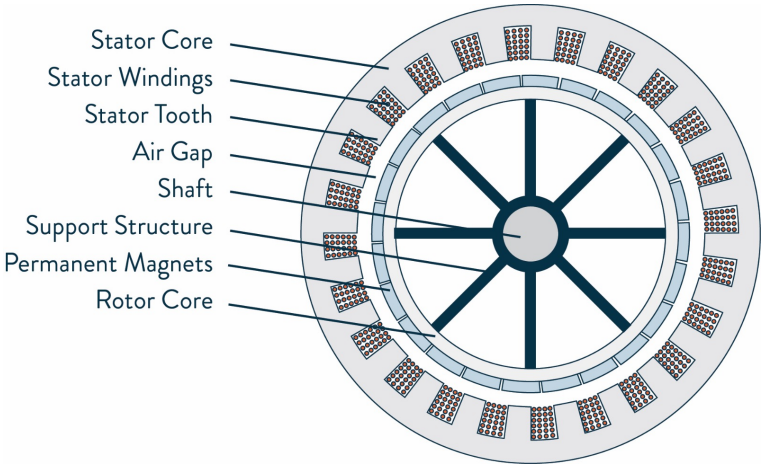

Figure 4.3: Schematic overview of a permanent magnet direct drive generator

Another limit is determined by the amount of current that can be run trough the windings. A more thorough explanation will be presented in chapter 4.3. This current density J of a conductor limits the current loading $\hat{A}_s$ of the generator. These two limits, limit the force density F_d as shown in (4.1).

The increase of the generator diameter and size, for an increase in torque loads can

be explained by noting that the force density is limited by material properties of the stator iron and the conductors/windings (see chapter 4.3). As the force density is limited, so is the the shear force in the airgap δ resulting from the multiplication of the force density with the airgap surface area. So the only way for the generator to handle an increase in torque while having a limited shear force value is to increase the airgap diameter.

4.3 The limiting mechanisms of a direct drive generator

The limiting mechanisms of a direct drive generator can be found as heat dissipation, limiting the linear current loading $\hat{A}_s$ and the magnetic saturation of the stator teeth limiting the air-gap flux density $\hat{B}_g$ as described in (Mueller, Markus and Polinder, Henk). Both of these parameters influence the force density F_d as shown in (4.1).

$$F_d \approx \frac{1}{2}\hat{B}_g\hat{A}_s \tag{4.1}$$

Due to these physical limitations the force density is a relatively constant value between 30 - 60 kN/m2 as described in (Mueller, Markus and Polinder, Henk) for air cooled machines. A higher force density will lead to higher generator torque as can be seen in (4.2) and this in turn leads to a higher power of the generator (4.3) (Asger Bech Abrahamsen, Dong Liu and Henk Polinder). In other words a higher input torque from the wind rotor can be handled by the generator if the area of the airgap increases. Figure 4.4 shows a zoomed in cross-section of the direct drive generator. With this figure the locations of the limiting mechanisms can be explained.

$$T = \frac{1}{2}\pi F_d D_{gen}^2 L_{gen} \tag{4.2}$$

$$P = \omega T \tag{4.3}$$

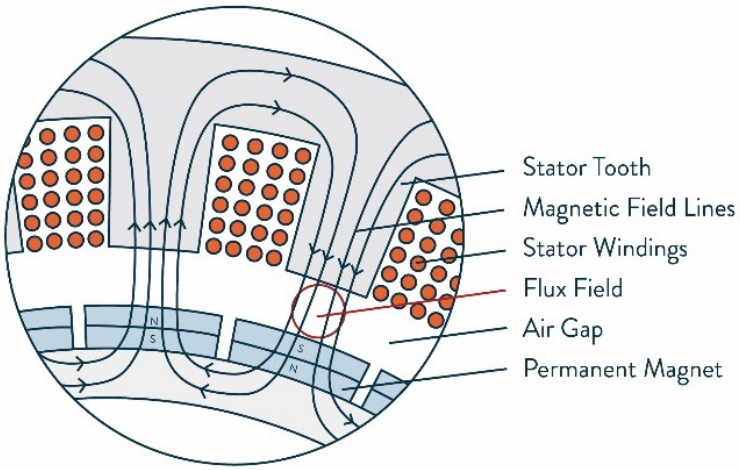

Figure 4.4: Zoomed in cross-section of a direct drive generator showing the flux and necessary components to explain the limiting mechanisms

4.3.1 Flux density as limiting mechanism

As explained in section 4.2 a flux appears when the magnetic field lines of a magnet passes the iron stator tooth. Surrounding the stator tooth are windings in which the current will be induced. The amount of flux that can flow between the rotor and stator is limited by the magnetic saturation of the stator tooth material. Flux is calculated as shown in (4.4).

$$\phi = \hat{B_g} A cos(\theta) \tag{4.4}$$

In (4.4), A represents the area where the flux lines pas through and θ is the angle of that area as shown in figure (4.4).

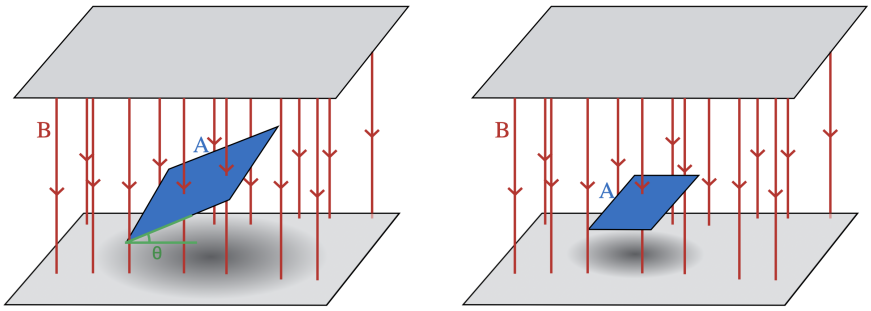

Figure 4.5: Magnetic flux trough a given surface area (KhanAcademy, 2018)

In the case of the generator used in this thesis the flux flows from permanent magnets on the rotor to the stator teeth. The objective when designing a generator is to increase the flux density as much as possible to obtain a higher force density F_d. As explained in chapter 4.2 the increase in flux density will lead to a higher force density which in turn leads to a higher power rating as can be seen in (4.2) and (4.3). However, several factors can limit the flux density, such as the saturation of the magnetic steel or the strength of the permanent magnets (Asger Bech Abrahamsen, Dong Liu and Henk Polinder). The flux density limit is depending on the material out of which the stator teeth are made. The magnetic permeability of a material can be plotted as shown in figure 4.6.

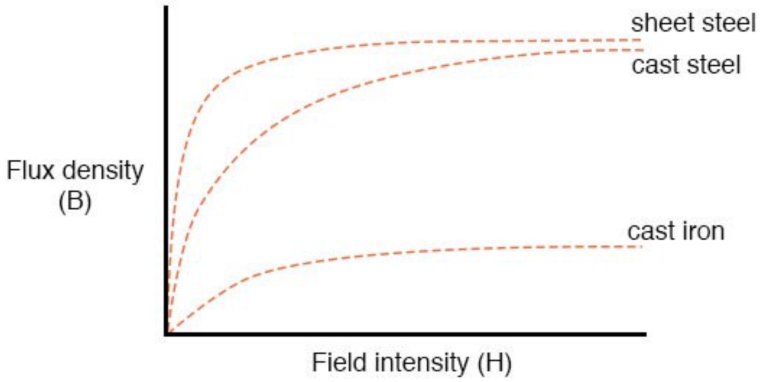

Figure 4.6: The flux density of several materials for an external magnetic field strength (CIRCUITS, 2018)

The y-axis represents the flux density of the material whereas the x-axis represents the external magnetic field H. It can be seen that the slope of the flux density gradually decreases until a maximum value is reached. After reaching the maximum value

the material will behave as if in a vacuum. A small increase of the flux density can still be achieved but a large increase of the magnetic field strength is necessary, which is not efficient. The flux density that corresponds with the asymptotic value shown in figure 4.6, is the point at which the material is saturated. The trend of this curve can be explained by the fundamentals of ferromagnetic materials. For low values of the external magnetic field H not all the atoms in the material are aligned. For high values of the external magnetic field, a value of the magnetic value is reached where all the atoms are aligned and therefore no more magnetic field lines can pass through the same surface area for a material. Since the flux density saturation has now been explained, the material properties can be studied of the magnets and stator material to determine if the strength of the magnets can also limit the flux density instead of the permeability of the stator material. For this to happen the flux density provided by the permanent magnet in the stator tooth has to be smaller than the saturation value of the stator material $B_{magnet} < B_{stator}$.

The magnetic strength of a permanent magnet can be explained by expanding figure 4.6 to figure 4.7. This curve represents the magnetic hysteresis curve of a ferromagnetic material. The fundamental take away of this curve is that a certain amount of flux is left in the material while there is no external magnetic field present. The ferromagnetic material has now become a permanent magnet. Figure 4.7 also shows that when the magnetic field is reversed the flux will flow in the other direction.

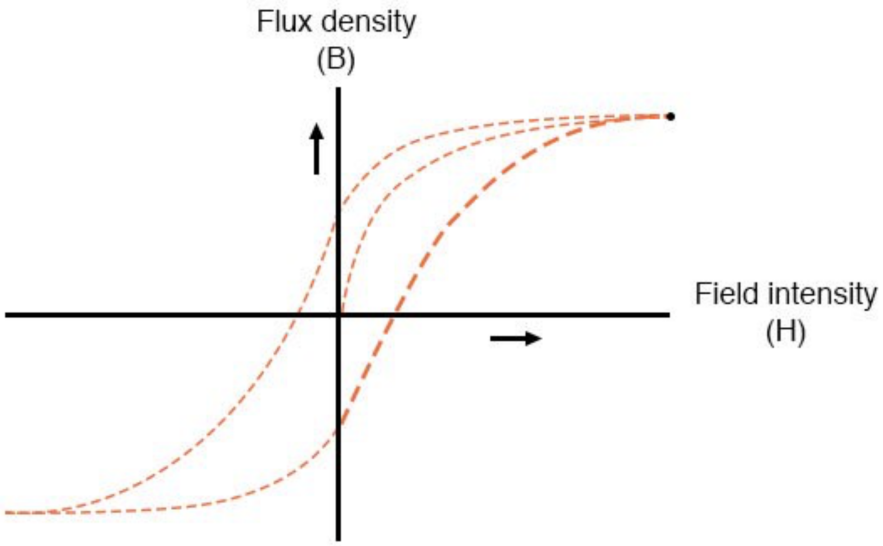

Figure 4.7: The magnetic hysteresis curve for a ferromagnetic material (CIRCUITS, 2018)

The amount of flux that is left in a material when no external magnetic field is present is called the remanence of the material B_r. This property is material dependent and materials with a high remanence are very suitable to be used as permanent magnets. A common type of permanent magnet that can be found in a direct drive wind turbine is the neodymium magnet (NdFeB) (Asger Bech Abrahamsen, Dong Liu and Henk Polinder). This magnet has a maximum remanence value of 1.5 Tesla T (Pyrhonen

et al., 2013). The relation between the magnetic remanance and the fundamental space harmonic of the magnetic flux density in the airgap of the generator is given in (4.5) (Polinder, 2013). In this equation l_m is the length of the magnet in the direction of the magnetization, μ_{rm} is the recoil permeability of the magnet, g_{eff} is the effective airgap, B_{rm} is the remanent flux density of the magnets, b_p is the width of the magnet and τ_p is the the pole pitch of the magnet.

$$\hat{B_g} = \frac{l_m}{\mu_{rm} g_{eff}} B_{rm} \frac{4}{\pi} sin(\frac{\pi b_p}{2\tau_p}) \tag{4.5}$$

Note that the flux density in the air gap usually has a value of 1 T for permanent magnet machines as described in Polinder (2013).
The effective airgap g_{eff} can be calculated with (4.6). Where g is the mechanical airgap and k_C is the Carter Richter factor. τ_s is the slot pitch of the machine and b_{so} is the slot opening width.

$$g_{eff} = k_C(g + \frac{l_m}{\mu_{rm}}) \tag{4.6}$$

The carter factor k_C can be calculated with the following equations (4.7), (4.8) and (4.9) (Mueller, Markus and Polinder, Henk).

$$k_C = \frac{\tau_s}{\tau_s - g_1 \cdot \gamma} \tag{4.7}$$

$$g_1 = g + \frac{l_m}{\mu_{rm}} \tag{4.8}$$

$$\gamma = \frac{4}{\pi}(\frac{b_{so}}{2g_1} arctan(\frac{b_{so}}{2g1}) - log\sqrt{1 + (\frac{b_{so}}{2g_1})}) \tag{4.9}$$

More on how the flux density saturates the stator of the generator will be presented in the next part of this section. In figure 4.8, the BH curve for several types of steel and iron can be seen. It can be concluded that the maximum flux density in these materials is 2 T. In other words the stator teeth of the generator will saturate a flux density of 2 T.

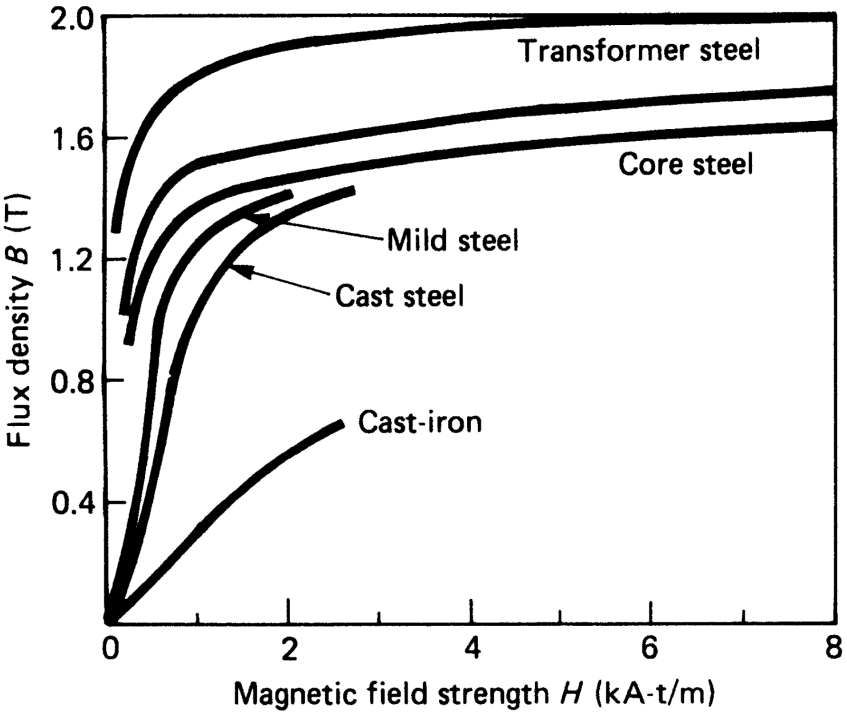

Figure 4.8: The magnetic hysteresis for steel and iron (Laughton and Say, 2013)

The relation between the flux density and the magnetic field strength is given by the permeability μ as presented in (4.10). The higher the permeability of the material the higher the flux density of the material becomes. The magnetic permeability is a material property that is also dependent on temperature.

$$B = H\mu \tag{4.10}$$

The permeability of a material can be calculated with (4.11), where μ_r is the relative permeability of the material and μ_o is the magnetic permeability of free space.

$$\mu_r = \frac{\mu}{\mu_0} \tag{4.11}$$

When looking at figure 4.9. It can be seen that the magnet has a larger surface area than the stator tooth. The ratio between these two surface areas is important, because it has an enlarging effect on the flux density in the stator tooth.

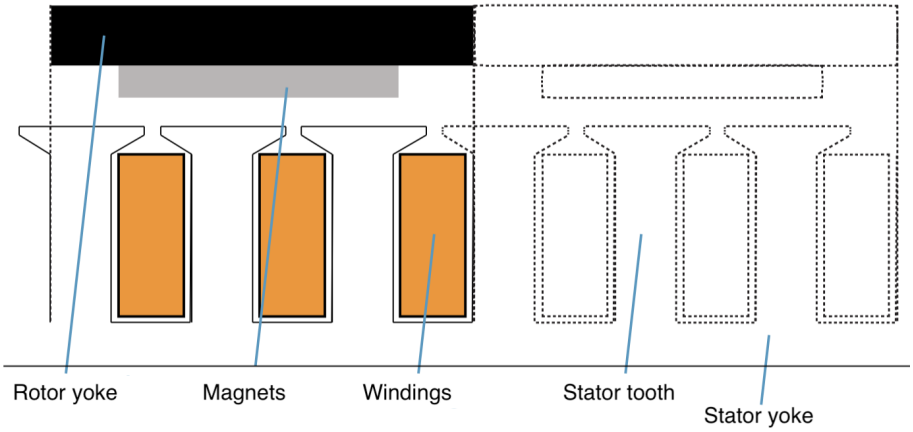

Figure 4.9: A sketch displaying the ratio between stator tooth width and slot width (Hartviksen, 2015)

The stator tooth width and slot width roughly have the same size. Therefore it can be assumed that half of the stator surface area consists out of tooth surface and the other half consists out of slot openings. It is important to note that the flux will always follow the path of least resistance which is provided by the stator tooth material. With this in mind the ratio of tooth area and airgap area is presented in (4.12).

$$A_r = \frac{A_g}{A_t} \tag{4.12}$$

Now, the relation between the flux density of the airgap $\hat{B}_g$ and the flux density in a tooth B_t is presented in (4.13). Considering figure 4.8, it can now be concluded that all the possible steel or iron stator materials will saturate at a flux density in the airgap of 1 T, Assuming that the conductors can cope with the induced current by the flux density in the stator teeth, the maximum flux density is limited by the saturation of the stator tooth material.

$$B_t = \frac{A_g}{A_t}\hat{B}_g \tag{4.13}$$

For both adjustments an asymptotic limit is found where after no increase of flux is to be expected. Moreover, increasing the tooth width will decrease the slot width therefore reducing the current loading $\hat{A}_s$ that will be discussed in chapter 4.3.2.

4.3.2 Current loading as limiting mechanism

As has been stated in Asger Bech Abrahamsen, Dong Liu and Henk Polinder and described in the previous chapter, the limiting mechanism for the maximum achievable force density of the generator is the saturation of the stator material and the current loading of the generator.
Besides flux density, the current loading of the stator windings A_s is also of influence on the force density given in (4.1). As stated in Asger Bech Abrahamsen, Dong Liu and Henk Polinder, the current loading is limited by the heating of the armature windings and the forced air cooling of the lamination steel of the stator teeth.

The value of the current loading limit can be obtained as shown in (4.14) (Shrestha, 2013).

$$\hat{A_S} = \frac{N_{slot} I_s q_p m_p}{\tau_p} \tag{4.14}$$

Where q_p is the number of slots per pole per phase, m_p is the amount of phases in a machine and τ_p is the pole pitch. In (4.15), N_{slot} is calculated, which represents the number of conductors per slot. Furthermore, I_s represents the root mean squared (r.m.s.) current, run through one conductor and can be calculated with (4.16). It is important to note that a square conductor shape is assumed with the sides equal to conductor diameter D_c, to fill the slot more efficiently. J is the maximum current density in the conductor where k_f is the filling factor of the slot. The average width of the slot b_{sav} and h represent the average width of the slot and the height of the slot.

$$N_{slot} = \frac{k_{fill} b_{sav} h}{D^2} \tag{4.15}$$

$$I_s = D_c^2 J \tag{4.16}$$

Substituting the above equations into (4.14) cancels out the diameter of the conductor and therefore no assumption is required.
As can be seen from (4.14), there are several parameters that are of influence on current loading. In the following paragraphs these parameters are described.

First of all (4.14) and (4.15) show that increasing the surface area of the the slot increases the current loading. However, increasing the slot width relative to the magnet increases the cogging torque of the machine as reported in Pyrhonen et al. (2013). Increasing the cogging torque will increase the cut-in speed of the wind turbine, but will also increase the noise and vibrations (GHIŢĂ et al., 2013). Furthermore, the increase of the slot width will decrease the stator tooth width, reducing the amount of flux that can flow through the stator. Increasing the height of the slots will increase the diameter of the generator, increasing the generator mass and increasing the slot leakage inductance as reported in Semken et al. (2012).

Secondly, increasing the filling factor will increase the current loading value. However, due to insulation of the conductors the filling factor of the slot is limited. Note

that a filling factor of 0.6 can be achieved when using rectangular coils and suitable insulation materials (Shrestha, 2013).

Thirdly, typical values for the current density J in a copper conductor are 3 - 4 A/mm2 (Asger Bech Abrahamsen, Dong Liu and Henk Polinder). The current density is limited due to the deterioration of insulation material because of excessive temperatures in the copper of the conductor (Polinder, 2013). The deterioration of the conductor material can cause a short-cut and destruction of the generator. Higher current density values are possible with forced cooling techniques such as air cooling and liquid cooling (Shrestha, 2013). The rise of temperature in the conductor is caused by two types of losses in the generator that generate heat. These losses can be found in the stator windings and the stator laminations (Polinder, 2013) and are explained in the following paragraphs.
Equation (4.17) is used to calculate the copper losses (Polinder, 2013). It is important to note that these losses generate heat and can damage the insulation material. In this equation R_s is the phase resistance and I_s the stator winding current. R_s is calculated with (4.18) (Polinder, 2013). ρ_{cu} is the resistivity of copper which is a material property, l_{Cus} and A_{Cus} are the length of the conductor for one turn and the area of the conductor respectively. Note that one turn is one circumference of the stator tooth.

$$P_{CU} = 3R_s I_s^2 \tag{4.17}$$

$$R_s = \frac{\rho_{cu} l_{Cus}}{A_{Cus}} \tag{4.18}$$

The length of the conductor can be estimated by taking two times the stack length of the stator and N_τ times the pole pitch τ_p of the generator, depending on the winding type (Polinder, 2013). This number than has to be multiplied by the number of turns to obtain the total length of the conductor. This is shown in (4.19).

$$l_{Cus} = N_s(2l_s + N_\tau \tau_p) \tag{4.19}$$

The area of a conductor is dependent on conductor fill factor k_{sfil}, the number of slots per pole phase q, the number of poles for the machine p, the slot area A_s and the number of turns N_s. The equations for the surface area of a conductor (4.20) and slot area (4.21) are shown below (Shrestha, 2013).

$$A_{Cus} = \frac{pqk_{sf}A_s}{N_s} \tag{4.20}$$

$$A_s = b_{sav}h \tag{4.21}$$

For the slot width b_{sav} the average width of the slot is taken.

The iron losses per unit of mass of the stator laminations can be calculated with (4.22) presented in Polinder (2013). The iron lamination loss is made up of the hysteresis losses and the eddy currents. Due to the hysteris losses less flux can flow through

the stator teeth as explained in section 4.7. The eddy currents cause losses due to the generation of heat as the current flows through the stator laminations. A loss factor of 2 is applied in (4.22) to compensate for the increased losses by manufacturing processes and the non sinusoidal flux density distribution (Polinder, 2013).

$$P_{Fe} = 2\frac{f_e}{f_0}\left(\frac{\hat{B_{Fe}}}{\hat{B_0}}^2\right)(P_{Fe0h} + P_{Fe0e}) \tag{4.22}$$

As stated in Shrestha (2013), direct drive generators have large diameters and therefore large surfaces. These large surfaces help to naturally cool the generator. Usually, the part of the generator that needs the most cooling will be placed on the outside of the generator. In the case of the RFPMSG in this thesis the stator will need to be placed on the outside of the generator this is due to the relatively high copper and iron losses in the stator of multi megawatt turbines. As these losses produce the most heat, it is more efficient to place the stator on the outside of the generator. There are exceptions in design of the generator, as presented in Shrestha (2013). Note that the permanent magnets also benefit from cooling as the magnetic properties decrease rapidly at high temperatures, lowering the remanence values. The temperature of the magnets is mainly determined by the temperature of the generator Shrestha (2013). In order to increase the current loading of the armature windings air cooling or liquid cooling techniques can be used, this will increase the current density that can be run through the conductor.

The reason that cooling has a positive effect on the temperature of a stator conductor winding is the reduction of resistance in the winding for lower temperatures. Equation (4.23), shows that for an increase in temperature the resistance in the conducting wire increases. R and R_{ref} represent the resistance of the conductor at the surrounding temperature and at the reference temperature respectively. α_t is the temperature coefficient of resistance for the conductor material. T and T_{ref} are the surrounding temperature and the reference temperature respectively. Substituting Ohm's law (4.24) and the power law (4.25) and (4.23), it can be shown that the power losses in the winding decrease with a decrease in surrounding temperature in (4.26).

$$R = R_{ref}(1 + \alpha_t(T - T_{ref})) \tag{4.23}$$

$$V = I \cdot R \tag{4.24}$$

$$P = V \cdot I \tag{4.25}$$

$$P = I^2 \cdot R_{ref}(1 + \alpha(T - T_{ref})) \tag{4.26}$$

In table 4.1 the effects of different cooling methods on the potential current loading can be seen. Direct water cooling is the most effective method to increase the current loading. However, for practical reasons direct water cooling is hard to implement in the generator, therefore, most generators are air cooled (Semken et al., 2012).

Table 4.1: Current loading potential for different cooling methods (Semken et al., 2012)

Cooling method:	**Potential Current Loading:**
Air Cooling	30 - 80 kA/m
H2 Cooling	90 - 110 kA/m
Direct Water Cooling	150 - 200 kA/m

Two heat transfer mechanisms can be differentiated within a generator. The most dominant heat transfer mechanism to spread the air coolant through the generator is convection given by (4.27) (Semken et al., 2012). The conductive heat flow through the generator materials can be calculated with (4.28), where h_t is the convective heat transfer coefficient, T_s is the temperature of the surface that has to be cooled, $T_{m,f}$ is the mean temperature of the fluid, k is the heat conductivity and ∇T is the temperature gradient (Semken et al., 2012). Using equations (4.27) and (4.28) the required cooling power is given by (4.29).

$$\Phi_{conv}" = h_t(T_s - T_{m,f}) \tag{4.27}$$

$$\Phi_{cond}" = -k\nabla T) \tag{4.28}$$

$$P = \Phi" S \tag{4.29}$$

As the temperature of the secondary coolant $(T_{m,f})$, will remain above the mean temperature of the primary coolant, the only way to further increase the convective flux density is to increase the heat transfer coefficient h_t given in (4.30) (Semken et al., 2012). Where k_a is the thermal conductivity of air and D_H is the hydraulic perimeter given as (4.31). With A as the surface area and P as the wet perimeter. The Nusselt number Nu is given as (4.32) where C, a and b depend on the flow surface geometry. Pr is the Prandtl number of the coolant and Re is the Reynolds number given in (4.33). The flow velocity w and kinematic viscosity ν can be seen in (4.33).

$$h = Nu\frac{k_a}{D_H} \tag{4.30}$$

$$D_H = \frac{4A}{P} \tag{4.31}$$

$$Nu = CRe^a Pr^b \tag{4.32}$$

$$Re = \frac{wD_H}{\nu} \tag{4.33}$$

In order to keep a constant or decreasing temperature the losses given by equations (4.22) and (4.17) have to be smaller than the cooling power as shown in (4.34).

$$P_{loss} \leq P_{cool} \tag{4.34}$$

In Semken et al. (2012) a proportionality is defined between the flow velocity magni-

tude v_{air}^3 and the power of the fan P_{fan} given as (4.35).

$$P_{fan} \propto v_{air}^3 \tag{4.35}$$

Using the following equations leads to the proportionality between the power of the fan and the nominal power of the generator P_n in (4.41) (Semken et al., 2012).

$$P_{cool} \propto v_{air}^a \tag{4.36}$$

$$P_{fan} \propto P_{cool}^{\frac{3}{a}} \tag{4.37}$$

Given the fact that the copper losses are proportional to the square of the current (4.38) and the nominal power of the generator is proportional to the current (4.39) a proportionality can be found relating the losses and nominal power of the generator (4.40).

$$P_{losses} \propto I^2 \tag{4.38}$$

$$P \propto I \tag{4.39}$$

$$P_{losses} \propto P^2 \tag{4.40}$$

Combining equations (4.37) and (4.40) gives (4.41).

$$P_{fan} \propto P^{\frac{6}{a}} \tag{4.41}$$

The following scaling law (4.42) can now be defined to calculate the necessary cooling power of a fan for different wind turbine rotor diameters.

$$P_{fan2} = \frac{P_{fan1}}{P_1^{\frac{6}{a}}} P_2^{\frac{6}{a}} \tag{4.42}$$

If just as in Semken et al. (2012) a constant $a = 4/5$ is used, a fan power of 50 kW for a 4 MW wind turbine is used, the necessary fan power can be calculated for different generator power and therefore wind rotor diameters as shown in figure 4.10. Note that for this figure it is assumed that all the dimensions of the generator are constant. In other words this figure shows how much cooling power you would need to keep a constant generator temperature while the rated power of the generator is increased. As can be seen in figure 4.10 the power needed to keep a constant generator temperature becomes very significant when increasing the rotor diameter. Therefore it is recommended to look at other coolants such as water to limit the power necessary for cooling. However, from figure 4.10 it can be concluded that there is a realistic limit to cooling power and therefore it is necessary to increase the size of the generator in order to have a higher power rating.

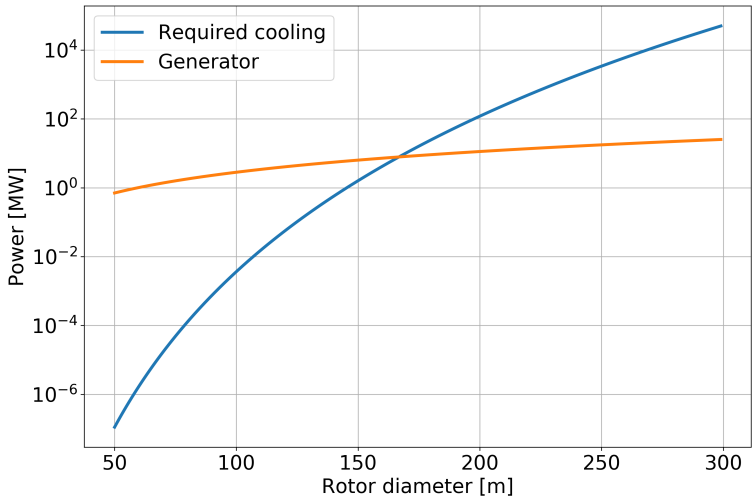

Figure 4.10: The fan power required to cool a generator that has constant dimensions for different rotor diameters

To summarize, the current loading $\hat{A}_s$ is limited by geometry configurations and heat losses in the stator laminations and the conductors. As discussed, due to design reasons increasing the current loading by increasing the slot area is not a practical solution. However, due to improved cooling in the generator the current density in the conductors can increase due to the decrease of the resistance of the conductor. However as shown in figure 4.10 there is an efficiency limit after which cooling causes a loss increase that is way too large.

4.4 Calculation method for the direct drive generator mass

In this chapter the scaling method in regards to the volume and mass of the generator for different rotor diameters will be explained. The scaling model is based on the scaling laws described in Shrestha et al. (2009). The force density and its limits are calculated according to the equations described in chapter 4.3.
The general equation for power produced by a rotating machine is given in (4.43).

$$P = \omega_m \cdot T \tag{4.43}$$

The same wind turbine parameters are used as given in table 2.1. Furthermore also the same assumptions are made for the wind turbine as shown in chapter 2.2.1. As the wind rotor shaft of the turbine is directly connected to the rotor or the generator, the torque (4.44) and angular speed (4.45) will be the same as that of the rotor. The torque and angular speed of the generator motor can be calculated with equations presented in section 2.2.1.

$$T_{hub} = T \tag{4.44}$$

$$\omega_{hub} = \omega \tag{4.45}$$

A relation between generator torque and rotor volume can be found in (4.46), as presented in Asger Bech Abrahamsen, Dong Liu and Henk Polinder. Note that equations (4.46) and (4.47) are the same as equations (4.2) and (4.1), but are repeated for the sake of clarity.

$$T = \frac{1}{2}\pi F_d D_{gen}^2 L_{gen} \tag{4.46}$$

Since the torque of the generator is known, the next step is to determine the force density F_d. The force density estimation is given by (4.47) as presented in Asger Bech Abrahamsen, Dong Liu and Henk Polinder. As discussed in chapter 4.3. The flux density $\hat{B}_g$ in the airgap can be estimated to be 1 T due to the saturation of the stator teeth material. Furthermore, for the current loading $\hat{A}_s$ a value of 100 kA/m is chosen. The value is obtained as described in chapter 4.3.

$$F_d \approx 0.5 \hat{B}_g \hat{A}_s \tag{4.47}$$

It can be seen that the only variables that are still unknown in (4.46) are the diameter of the airgap D_{gen} and the length of the generator L_{gen}. To solve (4.46), an aspect ratio k_{asp} for the generator is chosen with (4.48). As described in Shrestha (2013), the mass of the generator will increase with an increase in the aspect ratio of the generator. This shows that a generator with a large axial length is more expensive than a generator with a large radius. Based on Shrestha (2013) an aspect ratio is chosen of 0.4.

$$k_{asp} = \frac{L_{gen}}{D_{gen}} = 0.4 \tag{4.48}$$

With the substitution of (4.48) into (4.46), the airgap diameter and length can be

solved. The volume of the generator rotor can now be calculated with (4.49) for each rotor diameter.

$$V_{gen} = 0.25\pi D_{gen}^2 L_{gen} \tag{4.49}$$

A model for scaling the mass of direct drive generators is presented in Shrestha et al. (2009). In this model the mass of a direct drive generator is split up into three different masses: the electromagnetic part M_{em}, the structural part M_{arms} and the cylindrical part M_{cy}. The total mass of the generator is given as

$$M_{gen} = M_{em} + M_{arms} + M_{cy} \tag{4.50}$$

Figure 4.11 clearly shows the support structure, cylinders and electromagnetic parts of the generator.

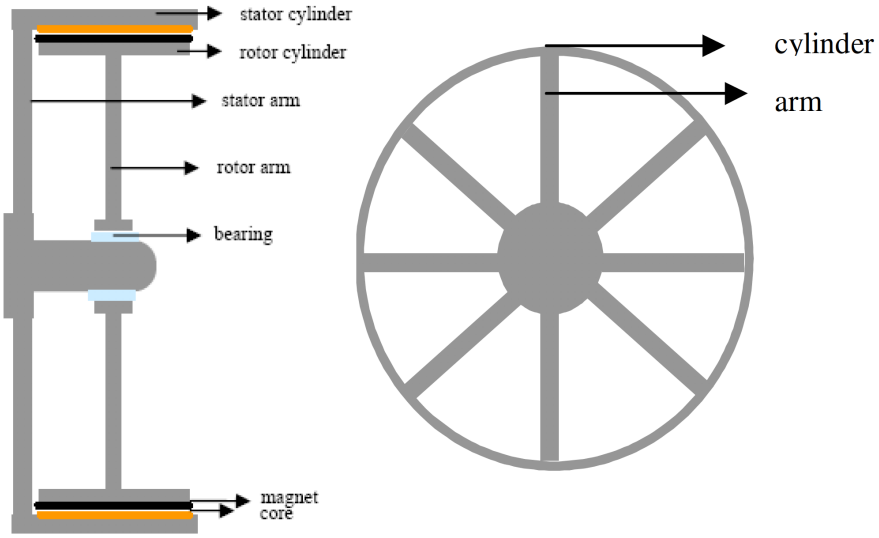

Figure 4.11: A side and front view of a direct drive generator (Shrestha et al., 2009)

The electrical, structural and cylindrical parts of the generator are scaled with equations (4.51), (4.52), (4.53) as described in Shrestha et al. (2009)

$$\frac{M_{em1}}{M_{em2}} = \frac{P_1}{P_2} \tag{4.51}$$

$$\frac{M_{arms1}}{M_{arms2}} = \frac{P_1^{1.75}}{P_2^{1.75}} \tag{4.52}$$

$$\frac{M_{cy1}}{M_{cy2}} = \frac{P_1^{1.5}}{P_2^{1.5}} \tag{4.53}$$

Note that the assumptions made for this model are that the flux density and the aspect ratio of the generator stay constant (Shrestha et al., 2009). Therefore the only way to handle more torque is to increase the airgap surface area, with an increase of volume and mass as a logical consequence. When equations (4.51), (4.52), (4.53) are rearranged as shown in (4.54), (4.55), (4.56), the mass of the electromagnetic,

structural and cylindrical parts can be calculated. More on the derivations of these equations is reported in Shrestha et al. (2009).

$$M_{em2} = \frac{M_{em1}}{P_1^{1.5}} P_2^{1.5} \tag{4.54}$$

$$M_{arms2} = \frac{M_{arms1}}{P_1^{1.75}} P_2^{1.75} \tag{4.55}$$

$$M_{cy2} = \frac{M_{cy1}}{P_1^{1.5}} P_2^{1.5} \tag{4.56}$$

Rearranging these equations to show the relation with the rotor diameter and power gives respectively (4.57), (4.58) and (4.59).

$$M_{em2} = \frac{M_{em1}}{8P_1^{1.5}} (\pi C_p \rho_{air} V_{wind}^3)^{1.5} D^{3.5} \tag{4.57}$$

$$M_{arms2} = \frac{M_{arms1}}{8P_1^{1.5}} (\pi C_p \rho_{air} V_{wind}^3)^{1.5} D^{3.75} \tag{4.58}$$

$$M_{cy2} = \frac{M_{cy1}}{8P_1^{1.5}} (\pi C_p \rho_{air} V_{wind}^3)^{1.5} D^{3.5} \tag{4.59}$$

As all the terms left of the rotor diameter D are constants the relation between generator mass and rotor diameter is shown in (4.60), (4.61) and (4.62) with constant G.

$$M_{em2} = G_1 D^{3.5} \tag{4.60}$$

$$M_{arms2} = G_2 D^{3.75} \tag{4.61}$$

$$M_{cy2} = G_3 D^{3.5} \tag{4.62}$$

Note that the fraction part in the above equations is constant. The variable P_2 is equal to the power produced by the rotor diameter of the wind turbine given in (4.43). Therefore, if the mass of the three parts and the corresponding power are known, it is possible to calculate the mass for a higher power rating of the generator. This only holds as an estimation of the mass, because no losses are assumed in the generator in these calculations.

Based on the report of Shrestha (2013), the data for the Enercon E82 double bearing generator is used to provide an idea of the mass scaling of direct drive generators. The Enercon E82 generator has a rated power of 2.3 MW (Enercon, 2018). The mass parameters that are used for scaling are presented in table 4.2.

Table 4.2: Enercon E82 mass parameters (Shrestha, 2013)

Component:	**Value:**
Weight of stator iron	6.99 tons
Weight of rotor iron	9.95 tons
Weight of stator copper	2.86 tons
Weight of rotor magnets	1.41 tons
Weight of rotor cylinder	2.37 tons
Weight of stator cylinder	4.03 tons
Weight of rotor arms	2.42 tons
Weight of stator arms	4.21 tons
Total	34.24 tons

With the data given in table 4.2, it is now possible to calculate the mass of the electromagnetic part M_{em}, the structural part M_{arm} and the cylindrical part M_{cy} as shown in equations (4.63), (4.64) and (4.65).

$$M_{em1} = M_{sI} + M_{rI} + M_{sCu} + M_{rM} \tag{4.63}$$

$$M_{arms1} = M_{rA} + M_{sA} \tag{4.64}$$

$$M_{cy1} = M_{rC} + M_{sC} \tag{4.65}$$

The total relation between power and mass of the generator is therefore given by (4.66).

$$M_{gen} = M_{em2} + M_{arms2} + M_{cy2} \tag{4.66}$$

To have a form of validation the method described in Fingersh et al. (2006) for the mass scaling of a direct-drive generator is used. Equation (4.67) is used to calculate the mass according to NREL. The equation is based on data and scaling laws obtained from the WindPACT studies. The low speed shaft torque T is used to determine the mass of the generator.

$$M_{NREL} = 661.25T^{0.606} \tag{4.67}$$

4.5 Results

4.5.1 Limiting mechanisms of a direct drive generator

As discussed in section 4.3, flux density and current loading are found to be the limiting mechanisms. A theoretical limit for the flux density $\hat{B}_g$ of 1 T in the airgap is found. The maximum current loading $\hat{A}_s$ is defined by the geometry of the stator and by the losses in the stator laminations and conductor windings. Changing the ratio of the stator slots and teeth per pole pitch is shown not to improve the force density F_d of the generator. Increasing the filling factor of the stator slots is difficult due to the necessity of insulation material and the shape of the conductors. However, significant increases in current loading can be achieved with different cooling methods as shown in table 4.1.

4.5.2 Torque density of a direct drive generator

In this section the results of the scaling method will be presented. This scaling method is based on the scaling equations discussed in chapter 4.4. The mass of the generator is based on the data of the Enercon E82 wind turbine. To obtain the results a python model was used. In figure 4.12 the contribution to the total mass of each of the three component categories is presented. It can be seen that the mass of the individual components scale with equations (4.54), (4.55) and (4.56). As expected there is an increasing trend for all the machine components as the rotor diameter and therefore the machine volume increases.

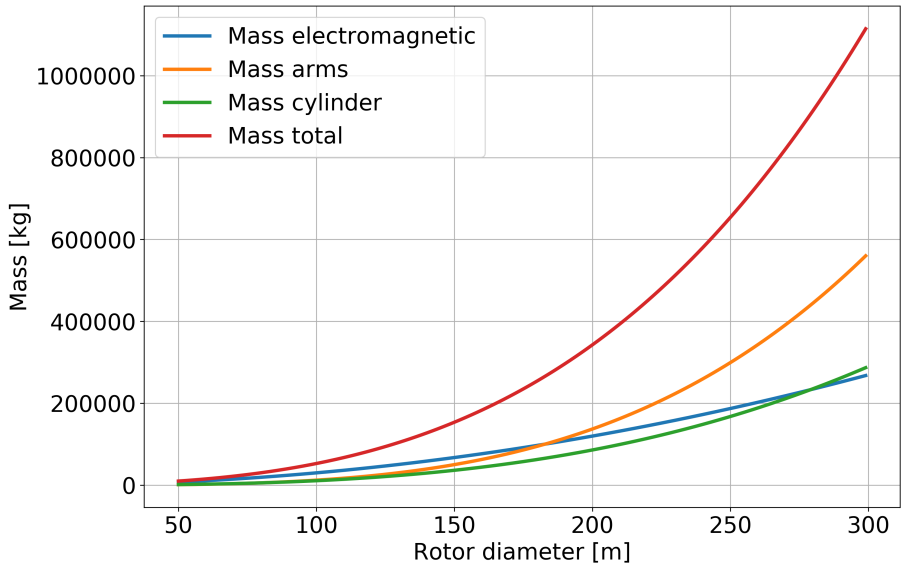

Figure 4.12: The contribution of the individual mass to the total mass of the generator

In figure 4.13 the mass comparison of the direct drive generator with the NREL model based on the data provided for the Enercon E82 wind turbine can be seen. To validate the model the mass of an existing General Electric generator (Monthly, 2011), a 3MW reference generator (Polinder, 2013) and a 10 MW reference generator (Polinder et al., 2007) were used. The NREL scaling model is based on data required in the year 2000.

As multi-mega watt direct-drive generator technology was in the beginning stages in that time, no multi-mega watt turbine data was available at the time. Therefore, this model shows low accuracy for larger rotor diameters. It has to be noted that the scaling model is heavily dependent on the input data provided by the Enercon E82 wind turbine.

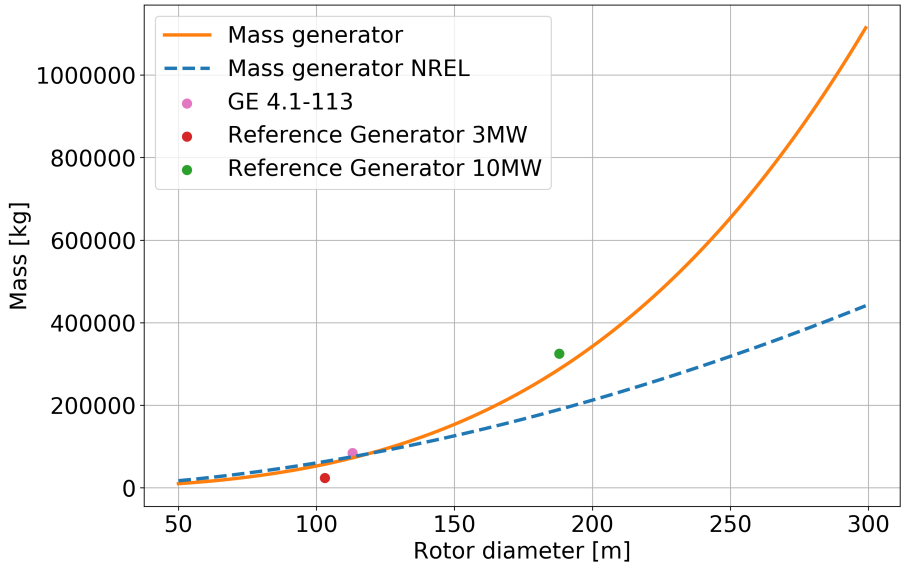

Figure 4.13: The Shrestha (2013) scaling model of a direct drive generator compared with the scaling model provided for direct drive generator by Fingersh et al. (2006)

In figure 4.15 the torque density of the generator can be seen. It can be concluded that the mass of the machine increases slower than the torque and therefore the torque density increases as shown in figure 4.14. Just as with the gearbox the rate of increase of the difference between torque and mass, decreases for larger rotor diameters, the torque density will therefore level off. When increasing the rotor diameter even further, the torque density will level off and then starts to decrease.

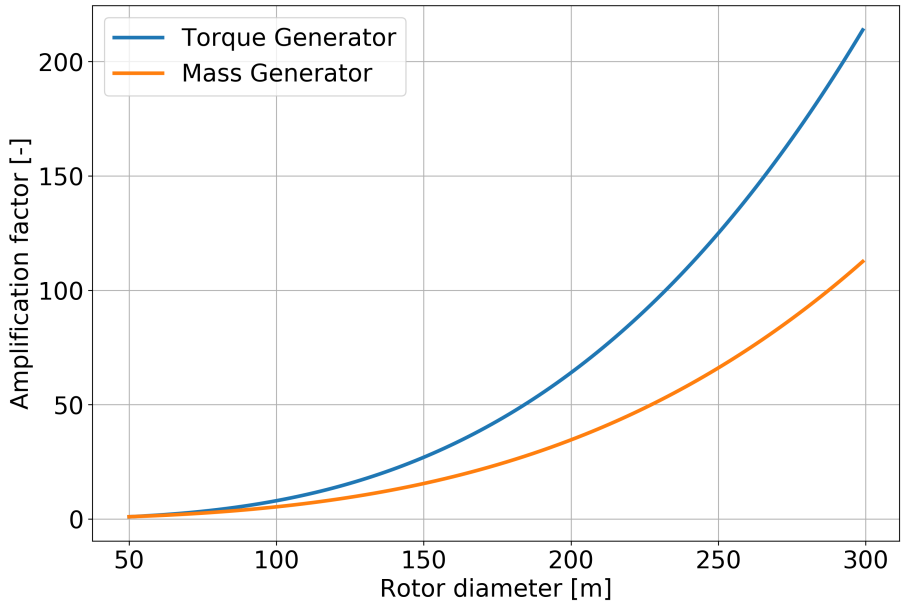

Figure 4.14: Amplification factor of the applied torque and generator mass

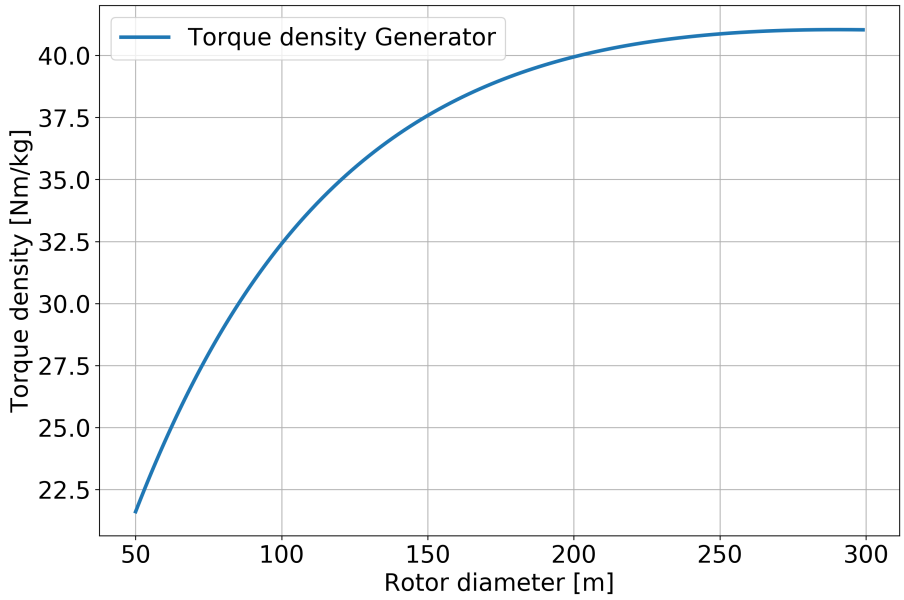

Figure 4.15: The torque density of the Enercon E82 generator

4.6 Conclusion

4.6.1 Limiting mechanisms of a direct drive generator

In sections 4.3.1 and 4.3.2 the limiting mechanisms of the direct drivetrain have been defined. The flux density is found to have a theoretical limit of 1 T because of the saturation of the stator tooth material in the generator. No theoretical limit can be found for the current loading $\hat{A}_s$ of the machine. As described in section 4.3.2, current loading depends on different variables (4.14). Firstly, due to practical limitations, increasing the height of the slots leads to an increase in slot leakage and is therefore not practical. Secondly, the filling factor can not be increased due to the insulation that is necessary for the conductors. Note that for modern generators square conductors are often used to make better use of the slot space. Thirdly, cooling increases the current density of the conductors and therefore has a positive influence on the current loading of the generator. However, as shown in figure 4.10, the required power needed to cool a generator for constant dimensions for increasing rotor diameter dramatically reduces the efficiency of the generator. Other cooling methods such as liquid cooling are potentially good options, however the positive influence on the torque density of these new cooling methods is not certain due to the potential increase of mass of the generator due to the mass of the cooling installation.

4.6.2 Torque density of a direct drive generator

As has been mentioned in section 4.5, the scaling model of the generator heavily depends on the mass inputs for the electro magnetic, structural and cylindrical parts of the machine. As the three inputs scale at different rates changing the composition will change the total mass for different parameters significantly. Unfortunately, very limited generator data is available, especially about the mass composition of the three mass categories. The model of the generator could be made more generic if it was assumed that ratios of the three mass inputs are the same for different generators. This assumption would make it possible to provide scaling models when only knowing the mass and the rated power of the generator. Unfortunately, this assumption is not very accurate as generator design differentiates widely between manufacturers (Anaya-Lara et al., 2018). Due to the lack of generator data especially in the two digit mega watt range, it is hard to validate the accuracy of this scaling method.

Furthermore it becomes apparent that the torque density seems to level off for larger rotor diameters. As the mass of the generator is increasing with a power higher than 1, the torque density starts to level off as shown in figure 4.15. The amplification factor for both the applied torque and mass of the generator is given in figure 4.14.

Because of the limiting mechanisms the force density F_d is not expected to increase much for the RFPMSGs if no new cooling method is introduced. Another possibility to achieve a significant reduction of generator mass would be to look for new support structures, for the generator rotor as described in Shrestha (2013). In the future, new generator designs might enable more compact designs. Such as superconduct-

ing generators described in Asger Bech Abrahamsen, Dong Liu and Henk Polinder and ironless generators described in Anaya-Lara et al. (2018). Super conducting generators have very low resistivity therefore the current loading $\hat{A}_s$ can be increased. Another development is the ironless machine that has no iron in the stator core. This results in lower attracting forces between the rotor and stator. As a consequence the support structure can be less strong and therefore lighter. These innovations path the way for higher torque density machines.

5 Wind turbine drivetrain with hydraulic pump transmission

5.1 Introduction

In this chapter the limiting mechanisms of an hydraulic pump used as a drivetrain unit in a offshore wind turbine is described. The hydraulic transmission is based on a Hägglunds radial piston motor used in pump configuration. In this chapter the limiting mechanisms of the hydraulic pump that uses oil as a hydraulic fluid will be described.

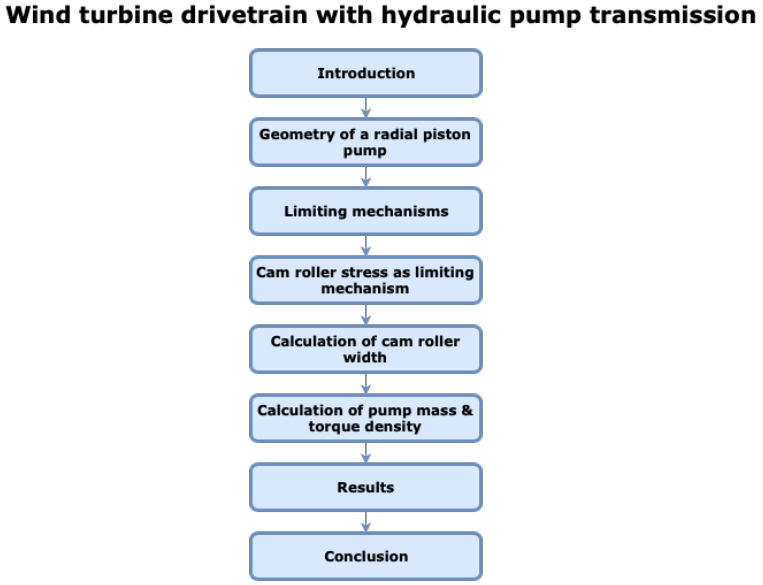

Figure 5.1: Hydraulic pump chapter overview

5.2 Geometry of a radial piston pump

As explained in the previous chapter a direct current (DC) generator can be used as a DC motor. The same goes for the radial piston motor being able to be used as a pump. In figure 5.2, the main properties of a Hägglunds pump can be seen. First of all, it is possible to see the main shaft connection to the pump. This shaft would be directly connected to the wind rotor. With a low rotational speed for big wind rotor diameters, as explained in previous chapters, the pump must be able to supply high torque in order to generate sufficient power. The main shaft is connected to a control ring, which is in turn connected to the pistons. The pistons interact with the camring which is held steady. The pistons have the same angular velocity as the drive shaft. As the pistons turn with the drive shaft they are forced to extent and retract by the the cam rollers interacting with the camring. A piston in extended and retracted position are shown in figure 5.2. A zoomed in version of the pistons and camring interaction is shown in figure 5.3.

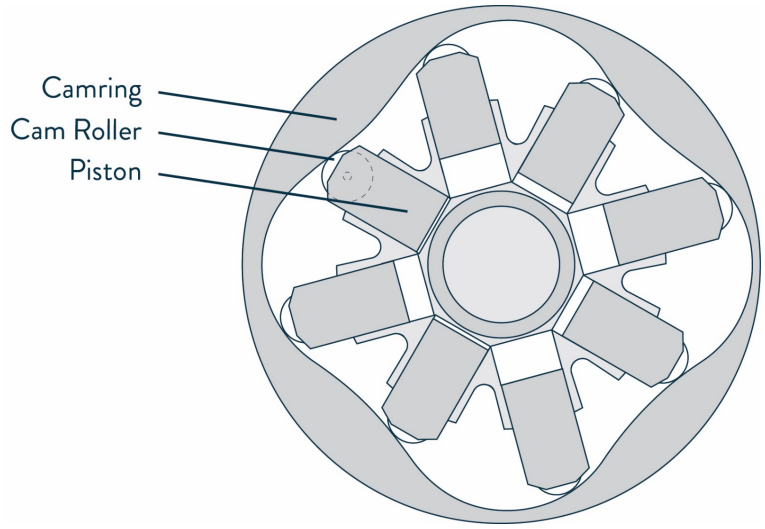

Figure 5.2: Cross-section of hydraulic piston pump with the essential components

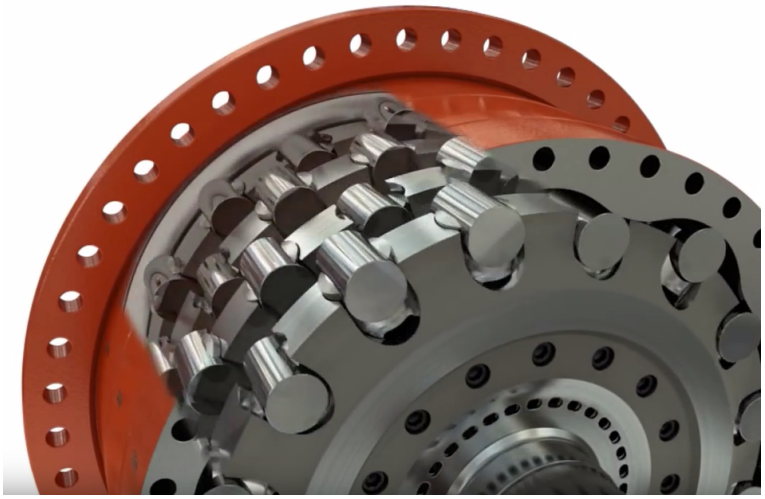

Figure 5.3: A zoomed in view of the Hägglunds pump with camring and pistons (Hagglunds, 2018)

In figure 5.4, the back of a Hägglunds pump is shown. The piston is pushed against the camring by the low pressure hydraulic fluid, given as the red arrow. The blue arrow corresponds with high pressure oil. This high pressure is caused by the piston retracting and pressurizing the oil in the cylinder. The hydraulic pump distributes oil through the valve plate to the pistons in the cylinder block, roughly 50% of them with high pressure and roughly 50% with charge pressure. The oil pressure forces the pistons outward against the camring (Hagglunds, 2018). The green arrow in figure 5.4 is the leakage line. As the surface area of the pistons is slightly smaller than the cylinder there will be some leakage in the cylinder when the hydraulic fluid is pressurized. The reason for this difference in area between the piston and the cylinder is to reduce friction between the piston and the cylinder. Note that the amount of cams in the camring determines how many times each cylinder charges

and discharges in one revolution.

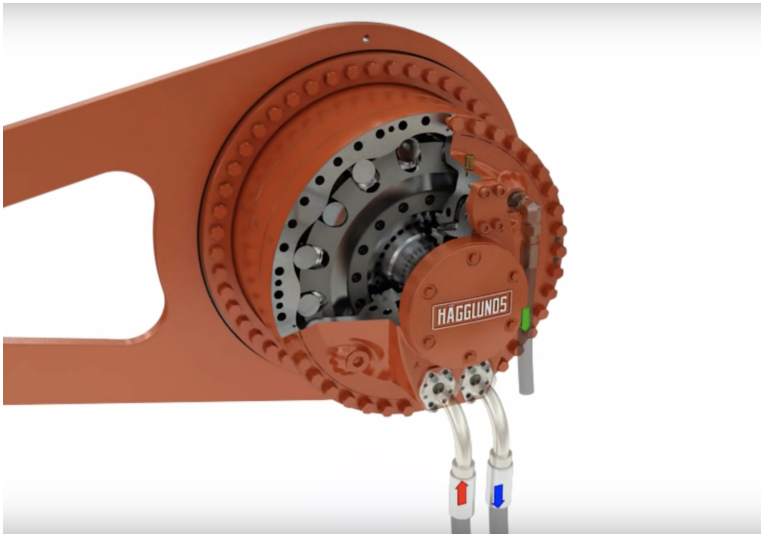

Figure 5.4: A back view from the Hägglunds pump with visible oil piping and pistons (Hagglunds, 2018)

In figure 5.5, a cross-section is presented of a Hägglunds pump. The position of the piston that is attached to the cylinder block is clearly visible. Furthermore, the position of the cam roller that is attached to the piston and the interaction with the camring can be seen. Note that the whole cylinder block can rotate due to the two bearing rings. The camring of the hydraulic pump will stay stationary.

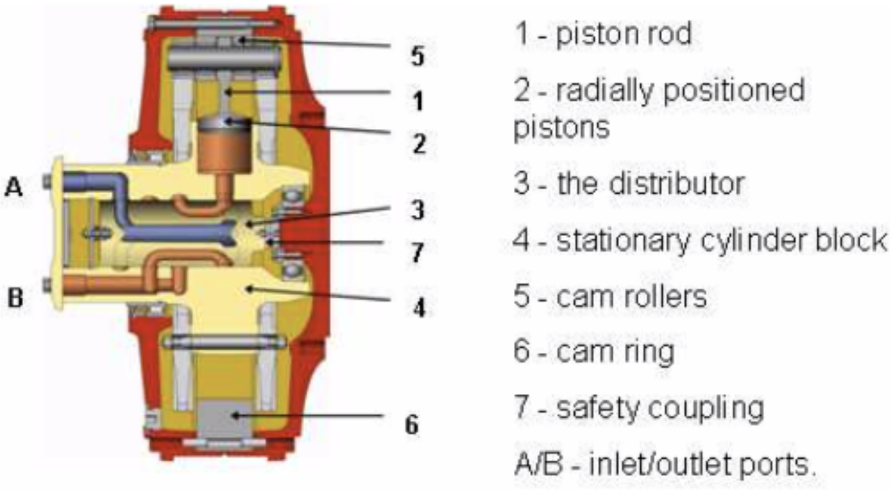

Figure 5.5: A cross-section of the Hägglunds pump with visible oil piping and pistons (Group, 2018)

It is important to understand what happens with the pressurized oil that is pumped out of the system. The total system for a wind turbine can be seen in figure 5.6. The oil circuit of the wind turbine is clearly visible as the blue and red line. Note that the

red line is in this case the high pressure line. Electricity is generated by coupling of the hydraulic pump to an oil motor that drives a generator.

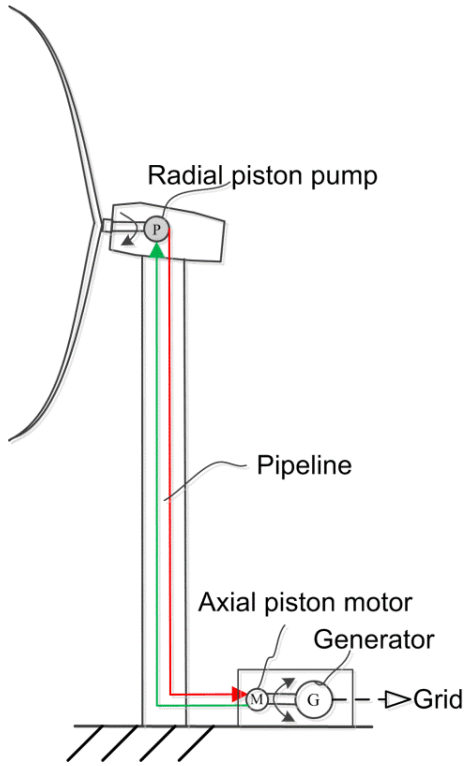

Figure 5.6: Total overview of a wind turbine with hydraulic transmission driving a generator (Yang et al., 2015)

5.3 Cam roller stress as limiting mechanism

The limiting mechanism that determines the size of the pump and therefore the mass of the pump are the hertz stresses between the cam roller and the camring as shown in figure 5.7. This interaction can be described as the interaction of two cylinders with different radii (Utah University). A schematic figure of the camring and piston interaction can be seen in 5.2. In theory, if the cam roller and camring would have an infinite elasticity modulus E, the contact point would be a line for two cylinders and the stress at this line will be infinitely high. However, as the materials do not have an infinite elasticity modulus, the interaction point of the cylinders will not be a one dimensional line, but will be a two dimensional contact area (Utah University). The force that is applied by one cylinder to the other will therefore be distributed over that contact area as can be seen in figure 5.8.

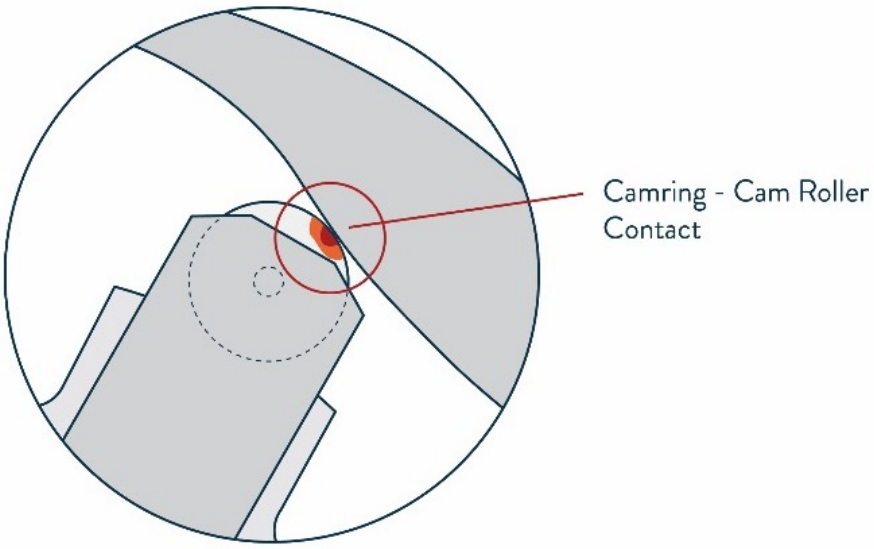

Figure 5.7: Location of the limiting mechanism for a hydraulic piston pump

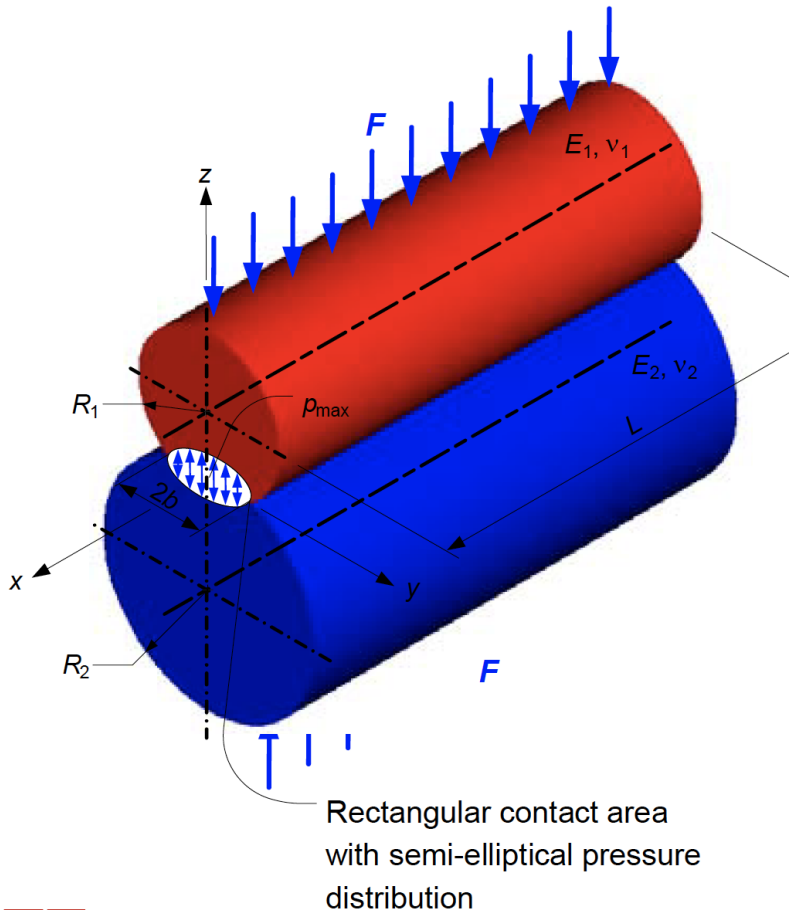

Figure 5.8: Interaction of two cylinders with contact area (Utah University)

The width and the maximum pressure of the contact area can be calculated with (5.1) and (5.2) (Budynas et al., 2008).

$$b_{cam} = \sqrt{\frac{4F_{cam}(\frac{1-\nu_1^2}{E_1} + \frac{1-\nu_2^2}{E_2})}{\pi L_{cam}(\frac{1}{R_{c1}}\frac{1}{R_{c2}})}} \tag{5.1}$$

$$P_{max} = \frac{2F_{cam}}{\pi b_{cam} L_{cam}} \tag{5.2}$$

In the above equations ν is the Poisson's ratio, R_c the radii of the cylinder and the cam roller. As reported in Budynas et al. (2008) P_{max} can defined as the surface endurance strength σ_{Hmax} leading to (5.3). To find the σ_{Hmax} value, fatigue tests have been conducted for 10^7 cycles. This limit is also known as the Hertzian endurance strength. The value for the Hertzian endurance strength of steel is: 1.72 [GPa] (Radzevich, 2012).

$$\sigma_{Hmax} = \frac{2F_{cam}}{\pi b L_{cam}} \tag{5.3}$$

Substitution of (5.1) and (5.3) leads to (5.5) where (5.4) is a constant depending on constant geometrical and material properties. It is now possible to calculate length L_{cam} of the cylinder when applying a force F_{cam}.

$$K = \frac{\frac{1-\mu_1^2}{E_1} + \frac{1-\mu_2^2}{E_2}}{\frac{1}{R_1} + \frac{1}{R_2}} \tag{5.4}$$

$$L_{cam} = \frac{F_{cam}}{K\sigma_{Hmax}^2 \pi} \tag{5.5}$$

First of all, it can be seen from the above equations that for an increase in force F_{cam} the length L_{cam} of the cylinder increases. Secondly, materials with a lower elasticity modulus will experience larger deformations, which will result into a larger contact area and therefore a lower contact pressure (Utah University). Thirdly it is important to note that the radius of the camring is continuously changing. When the piston is fully extended the radius of the cam is negative and small. When the piston is fully retracted, the radius of the piston is positive and small. Half way between these points the radius of the camring can be approached as infinite, as if the cylinder is in contact with a flat plate. A negative and infinite radius interacting with a cylinder is shown in figure 5.9.

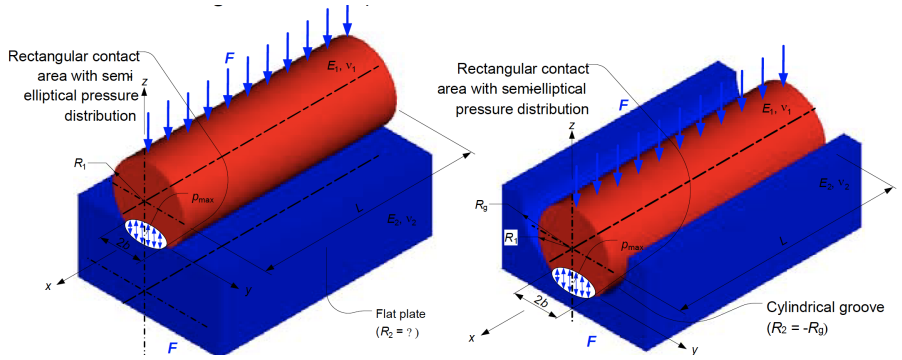

Figure 5.9: On the left the interaction of cylinder with a flat plate can be seen (infinite radius). On the right the interaction of a cylinder with a plate of negative radius can be seen. (Utah University)

From (5.4), it can be seen that an infinite radius for one of the cylinders has a positive effect on the required length L_{cam} of the cylinder. This can be explained by the larger contact area that is available due to the flat surface, which in turn reduces the stress. Studying the case of the piston cylinder interacting with the convex radius of the camring, shows that the required length will be the largest. Therefore, the convex radius of the camring will be considered in the calculations made in chapter 5.4.

5.3.1 Influence of lubricants on contact stress

As described in Hagglunds (2018), the hagglunds pump is filled with a lubricant. The lubricant will increase the contact area between the camring and cam roller as shown in figure 5.10. It can be seen that the contact band width B_{cam} is used in a more optimal way in regimen 3 than regimen 1. As a consequence the stresses are spread over a larger area enabling more compact, gear design.

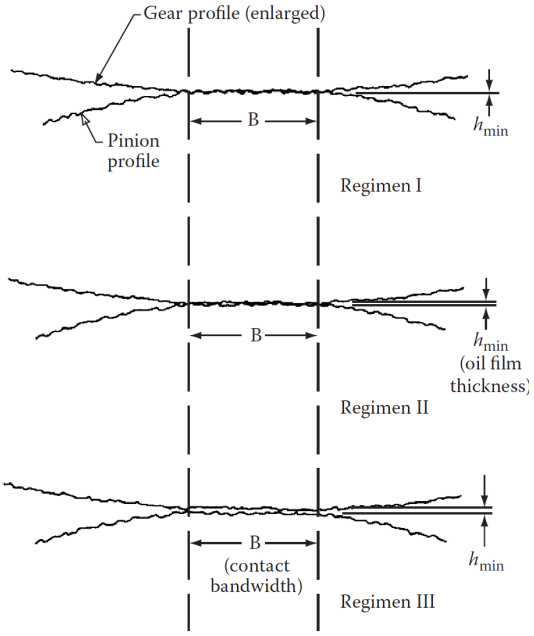

Figure 5.10: A microscopic view of the interaction of two gears for three lubricant regimes. (Radzevich, 2012)

The effect of the lubricant can be clearly seen on the Hertzian endurance strength σ_{Hmax} in figure 5.11. The Hertzian endurance strength of regimen 3 increases less than the other two regimes for the same amount of loading cycles. From this figure it can be concluded that the use of lubricants lowers the required width of, in this case, the cam roller.

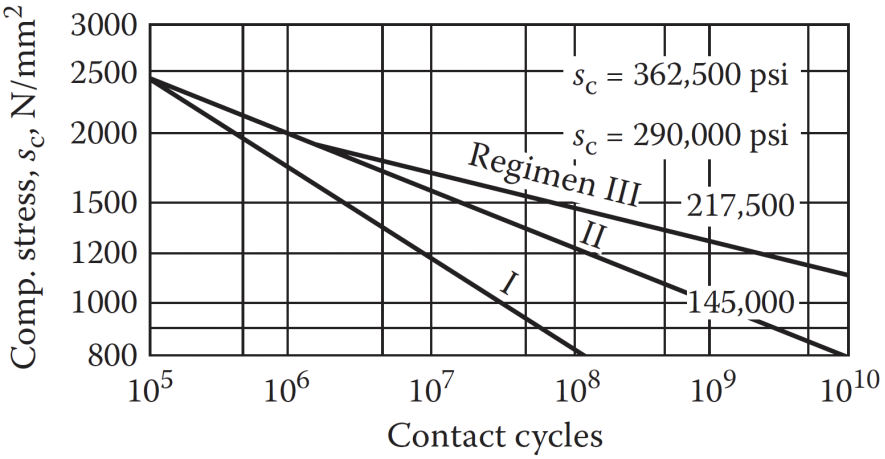

Figure 5.11: The influence of lubricants on the Hertzian endurance strength of carburized gears (Radzevich, 2012)

Lubricants that are used often in gears and pumps are presented in table 5.1. Note that for some nonmetallic gears water is also used as lubricant, however the oiliness properties are very poor. The use of water as a lubricant will generate, Hertzian

endurance strength values close to regimen 2 in figure 5.11.

Table 5.1: Fluids used to lubricate gears (Radzevich, 2012)

Fluids:	**Oiliness**	**Where Used**
Petroleum oils	Good	All types of gears except under unusual temperature conditions
Diester	Good	Aircraft and military gears with wide temperature ranges
Polyglycol	Good	Some bronze gears, steel gears with wide temperature ranges
Silicone	Poor	Some extreme-temperature cases, light load
Water	Very poor	Some nonmetallic gears
Phosphates	Good	Aircraft hydraulic equipment

5.4 Calculation method for the hydraulic pump mass

The wind turbine parameters for this model are the same as the ones used in table 2.1. Furthermore, the wind turbine equations and assumptions described in chapter 2.2.1 are used to calculate the torque and angular velocity of the shaft connected to the pump. The power of the wind rotor is again given by (5.6).

$$P = \omega T \tag{5.6}$$

As the shaft from the wind rotor is directly connected to the pump the torque and rotational speed of the pump will be equal. As the torque is therefore known the displacement of the cylinders of the pump can be calculated with (5.7) (BOSCH). Where Δp is the pressure difference between the incoming and out going oil pressure. The displacement of the pump V_{pump} is the total discharge volume of the pump for one rotation.

$$V_{pump} = \frac{T \cdot 2 \cdot \pi}{\Delta p} \tag{5.7}$$

The volume of a single cylinder can be calculated by knowing the amount of cams N_{cam} and the amount of cylinders N_{cyl}. Note that the number of discharges for one cylinder is equal to the amount of cams on the camring for one rotation. Therefore (5.8) can be used to calculate the volume of a single cylinder.

$$V_{cyl} = \frac{V_{pump}}{N_{cyl} N_{cam}} \tag{5.8}$$

To calculate the force that will act on the cylinder it is assumed that the cylinders are homogeneously divided over the camring and are all in a different state of compression. The last assumption is made by assuming that the camring describes a sinusoidal trajectory. With these assumptions all the cylinders can be seen to be rolling against a cosine shaped camring between 0 and π. The total horizontal force that is necessary to handle the rotor torque is calculated with (5.9).

$$F_H = \frac{2T}{D_{pump}} \tag{5.9}$$

The cylinder force is calculated by dividing the total horizontal force by the number of cylinders as seen in (5.10).

$$F_{Hcam} = \frac{F_H}{N_{cyl}} \tag{5.10}$$

To calculate the vertical and perpendicular component of the force, geometrical relations lead to equations (5.11), (5.12) and (5.13). With α as the slope of the cam, F_{Vcyl} as the vertical component causing pressure in the cylinder and F_{cam} as the perpendicular force between the cam roller and camring.

$$\alpha = \tanh \sin \frac{N_{cyl}(x)}{N_{cyl}} \pi \tag{5.11}$$

$$F_{Vcyl} = \frac{F_{Hcyl}}{\tan \alpha} \tag{5.12}$$

$$F_{cam} = \frac{F_{Hcam}}{\sin\alpha} \tag{5.13}$$

The pressure in the cylinder needs to be high enough to provide enough horizontal force to handle the torque. As the required vertical force for each position of the cam roller is calculated with (5.12) the highest required value is used to calculate the required area of the cylinder. As the outgoing pressure in the pump is held constant the area of the cylinder can be calculated with (5.14). Consequently the stroke length is calculated with (5.15).

$$A_{cyl} = \frac{F_{Vcyl}}{\Delta p} \tag{5.14}$$

$$S_{cyl} = \frac{V_{cyl}}{A_cyl} \tag{5.15}$$

Note that the assumption is made that there is no space between the cylinder and the piston. The force that is required by the piston to force the fluid out of the cylinder is determined by the required outflow pressure of the cylinder (Murrenhoff, 2016).
The force that is necessary to push the fluid out of the cylinder is equal to the vertical component of the interacting force between the cam roller and the camring . If the material properties of the camring and cam roller are known, (5.4) and (5.5) can be used to calculate the required width of the cam roller and the camring.

5.4.1 Mass calculation

In this section the method that was used to calculate the mass of the hydraulic pump is presented. Unlike the methods used to calculate the mass of the gearbox drivetrain and direct drive generator, the mass of the hydraulic pump is calculated purely based on empirical data obtained from Hägglunds data sheets. Data from the Hägglunds CB and CBM pump range were used. Attempts were made to develop a scaling model based on required dimensions of the piston roller, however the results proved to be very unreliable due to the many assumptions that had to be made regarding the volume of different parts of the machine. Another attempt to calculate the mass of the pump with empirical relations, provided by Kamat, was also made. Unfortunately, the empirical relations were not suitable for scaling to high power ratings and the Kamat pump is based on a different design principle. Therefore, the mass of the pump became unrealistically high. This will be discussed further in 5.6. Using the empirical data, a line was fitted through the data points as can be seen in figure 5.12. The equation describing the data fit of the plot is given in (5.16).

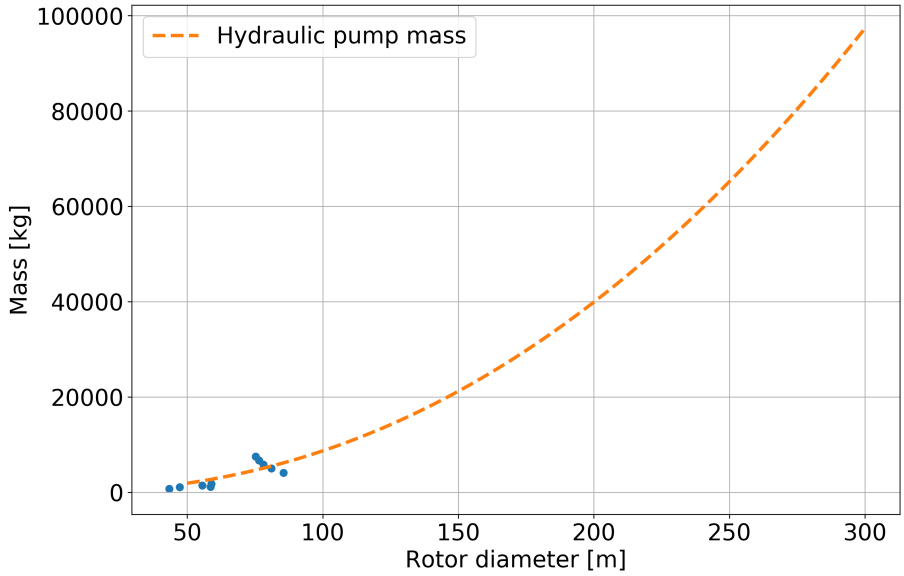

Figure 5.12: Mass function for a fluid transmission pump for increasing rotor diameter

$$M_{pump} = 0.35 D_{rotor}^{2.2} \tag{5.16}$$

It must be noted that only data was available for relatively small rotor diameters for the Hägglunds pumps, as is shown in figure 5.12. This generates quite a big uncertainty when creating (5.16) for larger rotor diameters.

5.5 Results

5.5.1 Limiting Mechanism of a hydraulic pump

The limiting mechanism of the hydraulic pump as defined in section 5.3 is the maximum Hertzian stress between the cam rollers en camring. This interaction is described with two interacting cylinders with different radii as shown in figure 5.9. The radius of the camring is changing due to its shape as discussed in 5.3. In (5.5) it can be seen that three material properties are of influence on the required length of the cam roller (L_{cam}). From (5.4), it can be concluded that an increase of the Poisson ratio (ν) has a increasing, therefore negative, effect on the required length of the cam roller. The Poisson ratio is a material property and is found to have a value of 0.3 for metals (Radzevich, 2012). Increasing the elasticity modulus of the material also has a negative influence on the required cam roller width as explained in 5.3. The elasticity modulus of steel is found to be 210 GPa (Radzevich, 2012). The third parameter that is influencing the required length of the cam roller is the Hertzian endurance strength (S_c). This value is found to be 1.72 GPa for 10^7 cycles using values for Regimen 3 lubrication (Radzevich, 2012). A higher value for the Hertzian endurance strength will lead to a lower required width of the cam roller. In figure 5.13, the calculated roller length for increasing rotor diameter can be seen. For the calculations the parameters presented in table 5.2, have been used as well as the equations in section 5.4. As expected the required cam roller width increases for an increase in rotor diameter. The radius of the cam is assumed constant, because only the concave section of the camring is considered. Furthermore, the radius of the cam roller is also constant to obtain a constant diameter of the pump.

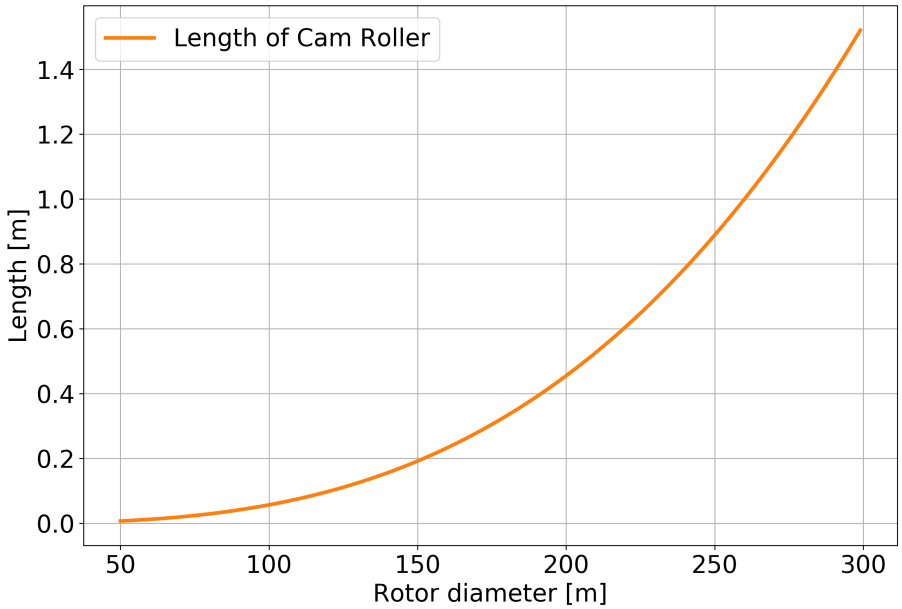

Figure 5.13: Required cam roller length

Table 5.2: Pump assumptions

Pump parameters	**Symbol**	**Value**
Pressure (Max)	P	350 Bar
Pressure loss	P_L	20 Bar
Charge pressure	P_c	8 Bar
Number of cylinders	N_{cyl}	40 -
Number of cams	N_{cam}	10 -
Aspect ratio cylinder	Asp_{cal}	1.5 -
Elasticity modulus	E	210 GPa
Hertzian endurance strength	S_c	1.72 GPa
Concave radius cam	r_{cam}	0.73 m
Roller radius	r_{roller}	0.23 m
Steel density	ρ_{steel}	8050 kg/mˆ3
Poisson's ratio	ν	0.3 -

5.5.2 Torque density of a hydraulic pump

In figure 5.14 and 5.16 the results for the mass and torque density of the pump are presented. The validation model that was used in figure 5.14 is described in Diepeveen (2013). This model is based on empirical radial piston data from 2013. With this data, (5.17) was created. From the results presented in figure 5.14 it can be concluded that pumps have become lighter over time for the same power level, leading to an increase of torque density. It is hard to define what the cause of this improvement is. Possibilities are that technical innovations have made it possible to construct a more compact pump design or the reduction of safety factors due to an improved reliability track record have made it possible to lower the mass. Do note that as mentioned in section 5.4.1 there is a large uncertainty for the larger rotor diameters due to the limited available pump data. It is is important to note that the Hertzian contact strength value is chosen for a regimen 3 lubrication regimen.

$$M_{pump} = 0.35 D_{rotor}^{2.2} \tag{5.17}$$

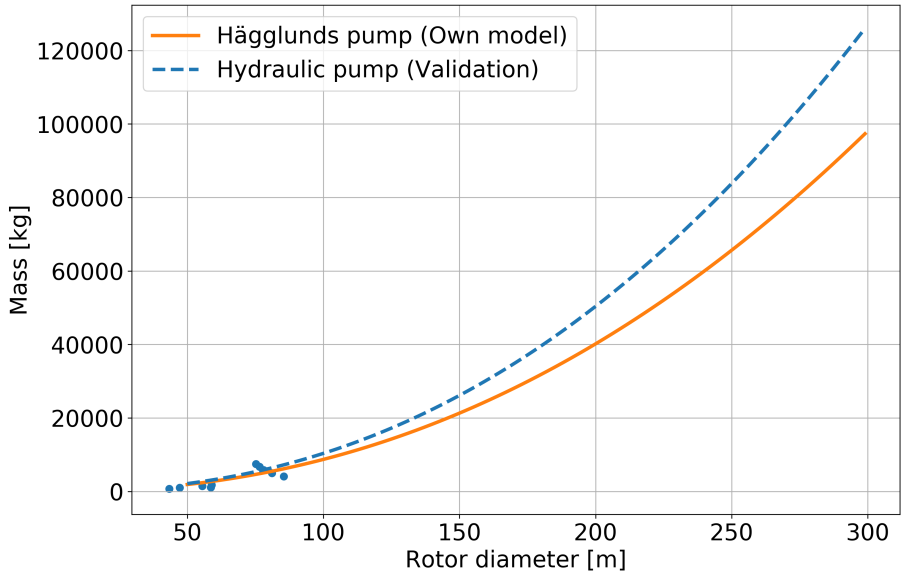

Figure 5.14: The mass of the pump compared to a validation model provided by Diepeveen (2013)

The torque density of the hydraulic pump is presented in figure 5.16. The torque density of the pump can be seen to increase as the rotor diameter increases. This means that the mass of the pump is increasing at a slower rate than the torque increases when increasing the rotor diameter of the wind turbine. The amplification factors of the applied torque and mass are shown in figure 5.15. As the torque increases with the power of three as shown in equation 2.7 while the increases with the power of 2.2 the torque density will increase with a power of 0.8.

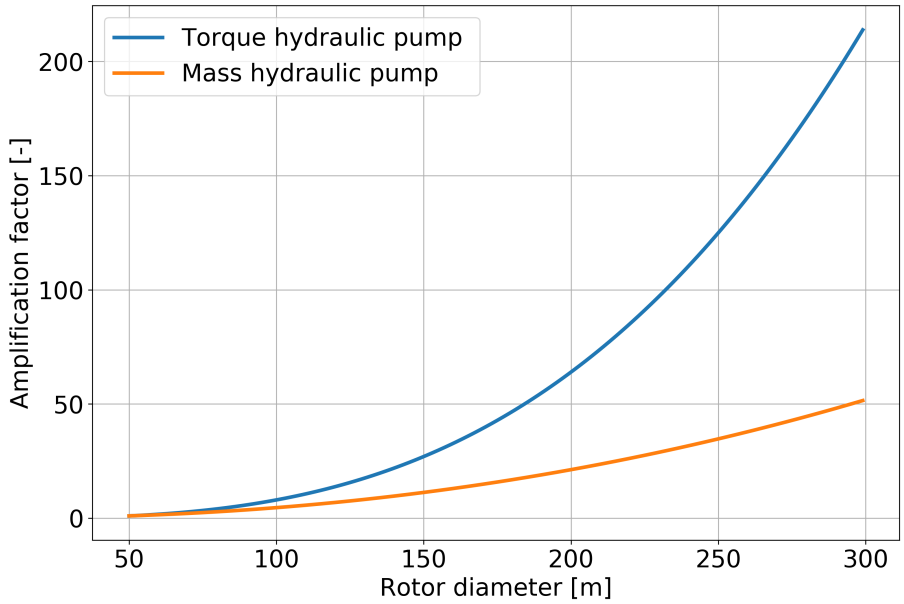

Figure 5.15: The amplification factor of a hydraulic pump

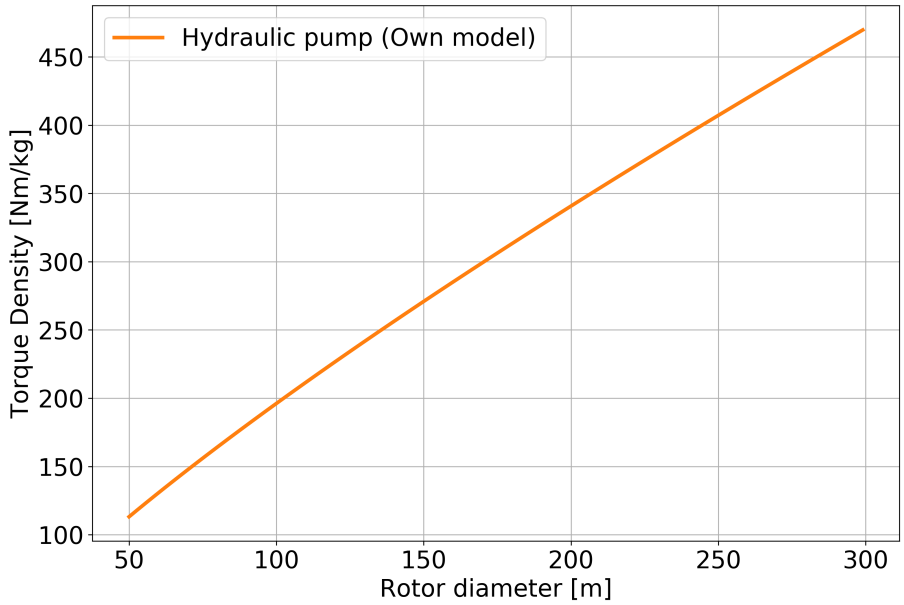

Figure 5.16: The torque density of a hydraulic pump

5.6 Conclusion

5.6.1 Limiting Mechanism of a hydraulic pump

The limiting mechanisms of the gearbox and hydraulic pump are very similar. Both the pump and gearbox are limited by Hertz stresses. As no teeth are involved in the pump design, no root stresses are present. The changing radius of the camring complicates the calculation of the necessary cam roller width. As described in 5.3, the radius that gives the largest required cylinder width is chosen to be limiting. It must be noted that adding a lubricant will decrease the required cam roller width as explained in 5.3.1, therefore enabling a more compact and lighter pump design. For the pump calculations a regimen 3 value for 10^7 cycles is assumed. A value for the hertzian endurance strength is found to be 1.72 GPa assuming carburized steel.

5.6.2 Scaling model of a hydraulic pump

Due to the lack of pump data for higher power ratings it was difficult to validate the results for the hydraulic pump with only Hägglunds data. In the end an empirical scaling equation was derived with data obtained from Hägglunds (Hagglunds, 2018). As shown in figure 5.12, all the data points are located in the lower rotor diameter region, therefore the uncertainty of pump mass values obtained for larger rotor diameters increases.

As argued in section 5.4 the radius of the cam is fixed as only the smallest radius is assumed of the camring. This can be justified by the fact that the smaller a radius is the bigger the required cam roller width will become.

It must be noted that the rated speed of the pumps used as data points differs. This has a influence on the pump data. If the angular velocity of the pump is increased the pump will have a higher power rating while maintaining the same mass. Therefore, in the pump data versions of the pumps where chosen that have similar rated speeds.

Finding a relation between the limiting mechanisms and the volume of the pump was not successful due to the lack of scaling equations for different components of the pump. Kamat, a pump manufacturer did provide empirical formulas for their pump design. However, these empirical relations proved not to hold for larger rotor diameters and therefore unrealistic results were obtained. Furthermore, the Kamat pump is based on different principles.

An explanation for the high torque density of the hydraulic pump can be found in the many Hertzian contacts over which the loads are spread in the pump. The contact area depends on the number of cam rollers and the size. The design of the radial piston pump makes it easy to create a large contact area in a relatively over which the stresses can be spread in a compact machine. The influence of the contact area is further discussed in chapter

6 Result comparison

In this chapter the results of chapters 3, 4 and 5 will be analyzed and discussed. The chapter consists out of two parts, the analysis of the limiting mechanisms and the results from the scaling methods for the three drivetrain configurations.

6.1 Limiting Mechanisms

As defined in chapters 3, 4 and 5, a limiting mechanism provides a restriction on the design of in this case a wind turbine drivetrain. Limiting mechanisms in machine design are often based on fundamental material properties, although limits can also be found due to practical design limitations.

6.1.1 Gearbox transmission

As discussed in chapter 3 the limiting mechanisms that can be found for a gearbox are the maximum allowable tooth flank stress and the root bending stress. Both of these limiting mechanisms are located on the gear teeth of a gear. From chapter 3 it can be concluded that the limiting mechanism can be found in the planet-sun gear interaction and not in the planet-ring interaction. Whether the root bending stress or the tooth flank stress will be the limiting mechanism depends on the module and ring diameter of the gear configuration. An increase of ring diameter will lead to an increase of the root stress. Furthermore, an increase in module of the gear will lead to a decrease in the root bending stress. The Hertz stresses on the tooth flank will decrease with an increase of contact ratio and therefore contact area. A cross-section of the gearbox with the most important components and limiting mechanisms is presented in figure 6.1

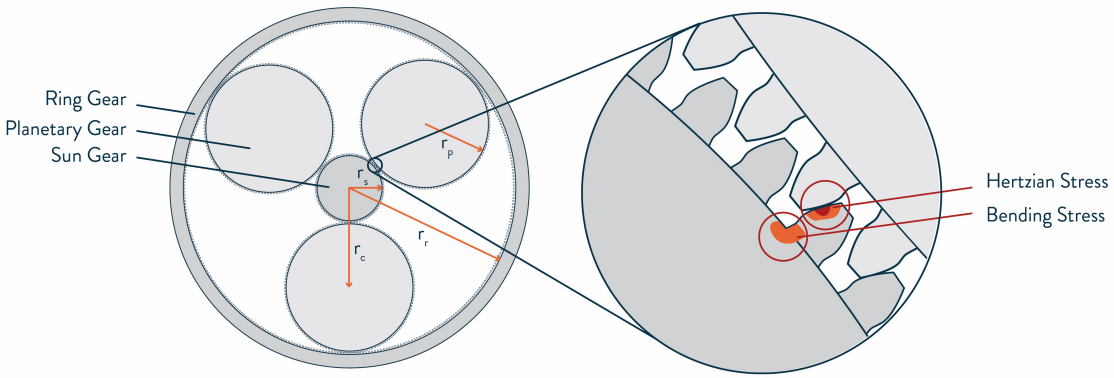

Figure 6.1: Gearbox cross-section highlighting the most important components and limiting mechanisms

As can be seen in equations (3.21), (3.30) the values that govern the required width of the gears are the maximum flexural strength and the maximum Hertzian endurance strength. An increase in value of both properties would lead to a size reduction of the gears. The increase of these values can be achieved by changing the gear material, but

also by using different lubricants as shown in figure 5.11. The Hertzian endurance strength (σ_{Hmax}) that is found in (Radzevich, 2012) for a regimen 3 lubricant is 1.72 GPa. The flexural strength limit (σ_{Fmax}) of the gear material is 0.24 Gpa (Gears, 2011).

A scaling model for the mass of a gearbox is developed using the required gear width that complies with the maximum tooth flank or root stress of the gears. This calculation method is presented in section 3.4. The model is validated with the model provided by NREL (Fingersh et al., 2006) and validation data from reference turbines for larger rotor diameters.

6.1.2 Direct drive generator

As discussed in chapter 4, direct-drive generators have a low rotational speed, because they are directly connected to the wind turbine rotor. In order to achieve a high power output, the generator has to provide enough torque to compensate for the low rotational speed as shown in (4.3). The amount of torque that a generator can deliver is related to the circumferential area of the air gap shown in figure (4.2). The force density F_d is relatively constant because it depends on two limiting values the flux density $\hat{B_g}$ and the current loading $\hat{A_s}$. A cross-section of the generator is presented in figure 6.2

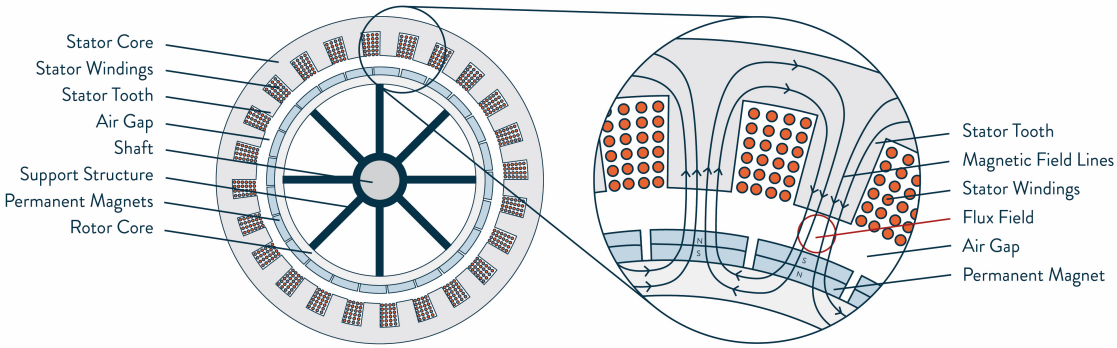

Figure 6.2: Generator cross-section highlighting the most important generator components

The flux density is limited by the saturation of the stator iron as described in section 4.3.1. Therefore, the maximum flux density in the airgap of the generator is 1 T. The mechanisms that limit the current loading are explained in section 4.3.2. As current loading is the amount of current that can flow through the conductor windings per pole pitch (4.14), three limitations have been defined.

1. Slot area
2. Filling factor

3. Current density

In theory the increase of the slot area would enable more conductors to fit in a slot and therefore more current could be run trough the slot per pole pitch. However, increasing the width of the slot will reduce the stator tooth area and increasing the height of the slot will increase the flux leakage.

Increasing the filling factor is also difficult due to the required amount of insulation of the conductors and the shape of the slot and conductors. Both the slot area and filling factor can be improved by small margins through optimization.

As explained in section 4.3, cooling of the generator will improve the current density, so more current can be run trough the same conductor area. Current loading values for different cooling methods are presented in table 4.1. Introducing more advanced cooling techniques like liquid cooling can improve the force density significantly of a generator while enabling the airgap area to stay the same. Note, that the extra mass from the cooling system and the decrease in efficiency the generator should be considered when calculating the total mass of the drivetrain system. In 4.10, a proportionality is defined between the power rating of a generator and the power needed to cool that generator while keeping the dimensions the same. From figure 4.10, it can be concluded that improvement of the force density of the generator is possible while keeping the generator dimensions the same, but that the energy losses can become very significant when increasing the power rating of the generator. Therefore, a machine efficiency limit can be found for the amount of generator cooling that is possible.

6.1.3 Hydraulic transmission

The Hydraulic drivetrain as described in chapter 5, is limited in design by the Hertz stresses between the cam roller and the cam ring. Just as with the gearbox, the required cam roller width is determined by the Hertzian endurance strength of the material in combination with the type of lubrication. For this Hägglunds pump a lubrication regimen 3 is used. As shown in figure 5.11, regimen 3 gives the highest endurance strength value and therefore the lowest possible roller width. The maximum endurance strength value for carburized gears, loaded 10^7 cycles is 1.72 GPa. The most important components and the location of the limiting mechanisms is shown in figure 6.3.

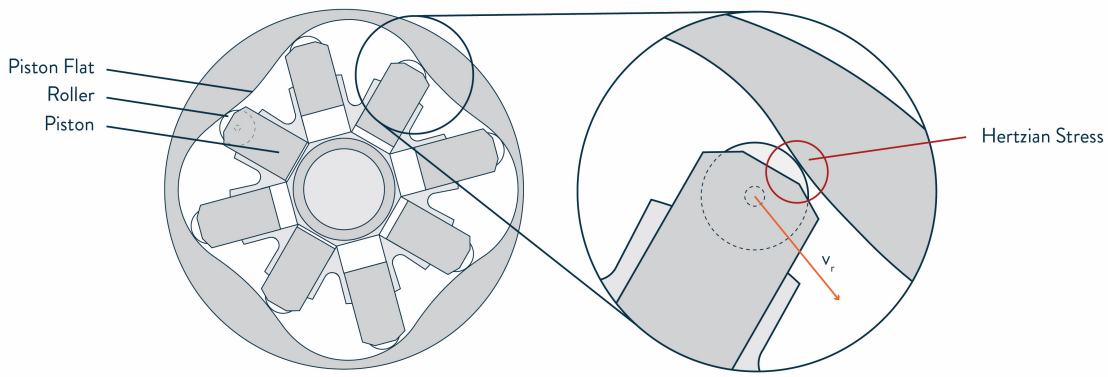

Figure 6.3: Hydraulic pump cross-section showing the most important components and the location of the limiting mechanism

The amount of torque that the pump can handle is related to the displacement of the pump as shown in equation (5.7). The higher the torque acting on the pump, the higher the force will be that is applied by the cam roller on the cam ring and so the required cam roller width will increase with equation (5.5). It is important to understand that increasing the displacement of the pump requires larger or more cylinders, cams and larger cam rollers. These larger or extra components, lead to an increase of the mass of the pump. Scaling these components for larger rotor diameters proved to be difficult because no scaling laws for each of the components were available in existing literature. A more thorough explanation about the scaling difficulties that were encountered can be found in section 5.6.2. In the end empirical data from Hägglunds pumps was used to create a mass scaling trend line for larger rotor diameters.

6.2 Torque density results

In figures 6.5 and 6.7 the mass and torque density scaling of the three drivetrain configurations are presented. These models are validated with existing scaling models based on empirical data provided by Fingersh et al. (2006) and Diepeveen (2013).

The scaling model developed for the gearbox shows a nearly similar trajectory as the validation model. As the gearbox scaling model is directly linked to the limiting mechanisms and material properties, the fundamental basis of this model is strong. From figure 6.7 it can be concluded that the torque density of the gearbox mass has improved over the years as the torque density of the scaling model is higher than that of the validation model.

The scaling of the direct drivetrain was based on existing scaling relations described in Shrestha et al. (2009). The difference between the validation line and mass has two reasons. First of all the model is highly dependent on the input power and mass of the reference generator as explained in section (4.50). Secondly the validation model is from the year 2000 and was based on low power rating generators (Sethuraman

et al., 2017). With validation data shown in figure 4.13 the most likely trajectory for the mass scaling of the direct drive generator is the trajectory of the own scaling model. From figure 6.7 it can be concluded that the validation model overestimates the torque density of the direct drivetrain as the scaling model shows to have a lower torque density for higher rotor diameters.

Both the scaling model and validation model of the hydraulic pump are based on empirical data. The validation model was developed for Hägglunds pumps with a low power rating. The scaling model was improved by adding more current data, showing an increase of the torque density when compared to the validation model, as can be seen in figure 6.7

The difference in mass for an increasing rotor diameter can be seen in 6.5. The direct drivetrain is seen to have the highest mass of the three configurations. The second highest mass is that of the gearbox and the lowest mass is that of the hydraulic pump. Note that the applied torque load coming from the wind rotor is the same for all the drivetrain configurations. Therefore, the hydraulic pump will have the highest torque density, the gearbox the second highest and the direct drive generator has the lowest torque density.

Relations for the rotor diameter of and volume of the gears are given by the following equations (3.60), (3.61), (3.59), (3.67), (3.68), (3.69) and (3.70) A relation for the mass of the generator and rotor diameter is given by (4.60), (4.61), and (4.62). Lastly a relation between the mass and rotor diameter for the hydraulic pump is found in (5.16).

An explanation for torque density values can be found in the limiting values of the machine (shown in table 6.1) and the required contact area shown in figure 6.4. It can be expected that the systems with a low limiting stress need a large contact area to handle the stresses. Looking at figure 6.4, it can be seen that this is especially true for the generator, requiring by far the largest contact area. When comparing the contact area of the pump and gearbox, the observation can be made that the gearbox requires a smaller contact area to handle the same torque when compared to the pump. However, it is by design easier for the pump to create a larger contact area for the same volume. The gearbox needs a lot of material to handle the large stresses on a small area leading to a high mass. This explains why the geared drivetrain has a lower torque density than the hydraulic pump.

Table 6.1: Comparison of the limiting mechanisms of the different drivetrain configurations

	Gearbox transmission	Direct-drive generator	Hydraulic pump transmission
Limiting mechanisms	σ_{Hmax} = 1.72 GPa σ_{Fmax} = 0.24 GPa	F_d = 60 kPa	σ_{Hmax} = 1.72 GPa

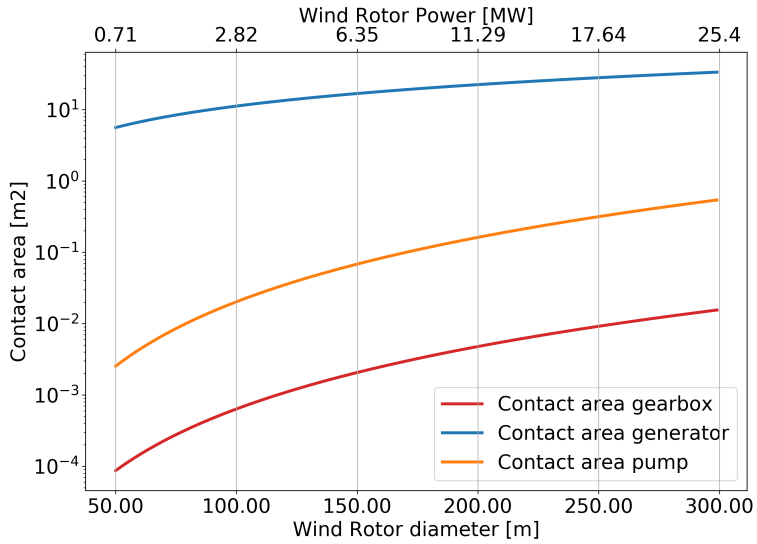

Figure 6.4: Minimal required contact area for the three drivetrains to handle the stresses caused by the applied rotor torque

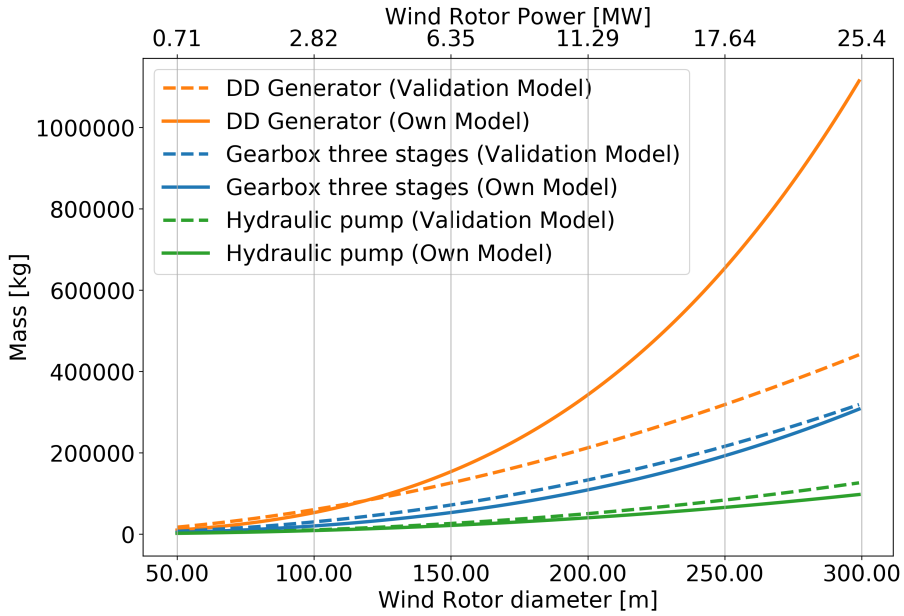

Figure 6.5: The mass comparison for the three drivetrain systems

The positive value of the torque density of all the drivetrains is first of all explained by the fact that the torque load is a lot higher than the mass of all the drivetrains over the entire rotor diameter. Secondly, figure 6.6 shows that the amplification factor of the torque over the rotor diameter is higher than the amplification factor of the three drivetrains. It can be concluded that the mass of all the drivetrains increases with a power higher than 2. This causes the torque density rate to decline as the torque increases with a power of three.

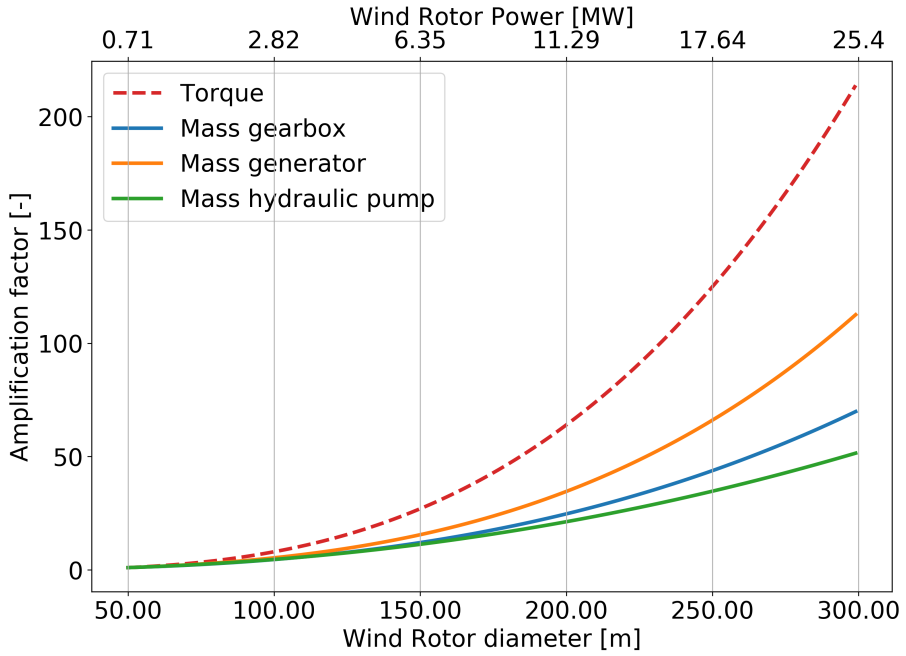

Figure 6.6: Amplification factor for the applied torque and the mass of the gearbox, generator and hydraulic pump

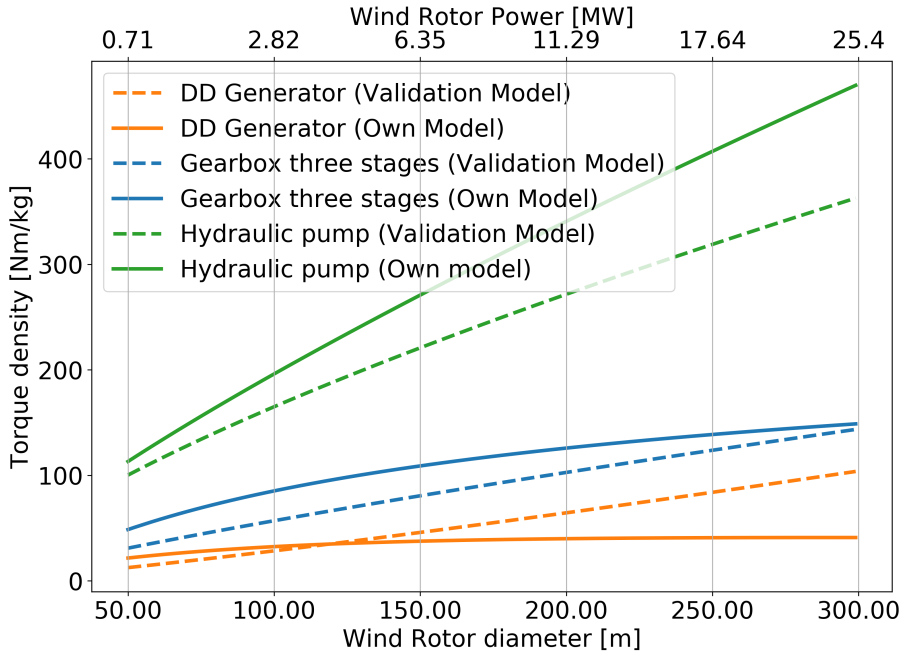

Figure 6.7: The torque density comparison for the three drivetrain systems

7 Conclusion

The difference in size between the three wind turbine drivetrain systems can be explained when looking at the maximum stress values of the limiting mechanisms presented in table 6.1. Note that the force density F_d follows from (4.1).
As explained, the three drivetrain configurations work in first principle the same. The three machines are all based on torque causing a rotation of the machine.
Looking at the results it can be concluded that the generator has lowest torque density. This low torque density is related to maximum allowable force density, however there is more to it. The forces that are generated in the machine depend on the diameter of the three drivetrains. The bigger the diameter of the machines the lower the tangential stress that need to be handled. For the generator the relation between machine diameter and torque capability is clearly visible in (4.2).It must be noted that an increase of generator diameter has a quadratic relation with the torque handling ability.

In the case of a gearbox stage, depending on the contact ratio, roughly 6 Hertzian contacts can be found to handle the stress. For the pump the contact area depends on the number of cam rollers. The contact area of the generator is the entire circumference of the rotor. In theory due to the large contact area the generator would be able to handle high torque loads, however as mentioned due to the low force density the generator has to become very large. The gearbox transmission and Hydraulic pump transmission both depend on the same limiting mechanisms. The contact area for both transmissions is a physical interaction of sun- ring gear contact or cam roller and camring contact. It can be concluded that due to the physical way of transferring the stress, the maximum allowable stress can be significantly larger, therefore requiring a much smaller contact area.
When looking at the design of a hydraulic pump it is possible to create more contact area by increasing the number of cam rollers while keeping the same compact design. As mentioned a gear stage has fewer contact points and therefore a smaller torque density than the pump. However, it must be noted that according to the latest developments in gearbox design the number of planets in a gear stage is increased significantly, therefore creating a larger contact area while keeping the dimensions the same.

For future high power rating applications the gearbox is a good candidate when looking at mass and torque density in figures 6.5 and 6.7. The reliability of wind turbine gearbox design has improved as a better understanding of the dynamic loads in a wind turbine were gained over time. However, with the lower rotational speeds of large rotor diameter wind turbines, providing a sufficient gear ratio will be a challenge. As shown in figure 3.11, the required gear ratio increases rapidly over the normal value of 120. It is therefore likely, that a medium speed generator will be used for large wind turbines. This medium speed generator is expected to be larger in volume and mass as explained in chapter 4, having a negative effect on the torque density of this drivetrain.

As there are practical and material limits that keep the force density constant of the generator, the only way to handle significantly more torque is to increase the volume and as a consequence the mass. New generator technologies are necessary to keep the direct - drive generator competitive with the gearbox drivetrain, if torque density is considered. Promising technologies that can help to increase the torque density of the generator are: ironless generators and super conducting generators (see C.4). New support structure types are also an option to reduce the mass of the generator as described in (Shrestha, 2013).

Hydraulic pumps can definitely start to play a roll in the wind turbine industry thanks to their low mass and high torque capability leading to a high torque density. As the Hägglunds motors currently don't have higher power ratings than 3MW, there is a large uncertainty about how the mass of these pumps will increase for larger rotor diameters. It can be concluded that for smaller rotor diameters the Hägglunds pump is definitely a competitor of the direct and gearbox drivetrains, when it comes to its torque density properties. The system yet has to prove that other properties such as reliability and efficiency are also competitive with the other two drivetrains. More tests and practical experience is necessary to determine the potential of the Hägglunds pump for these areas.

The results presented in figure 6.7 confirm the hypothesis that the Hägglunds hydraulic pump has the highest torque density of the three investigated drivetrain configurations. Furthermore, the research questions have been answered by defining the limiting mechanisms of the drivetrains and providing scaling models to find the achievable torque densities.

Appendices

A Wind turbine basics

In this literature study the focus will only be on horizontal axis wind turbines (HAWT). In figure A.1, the difference between a horizontal axis and vertical axis wind turbine can be seen. Furthermore the most important parts of a wind turbine are marked in figure A.1.

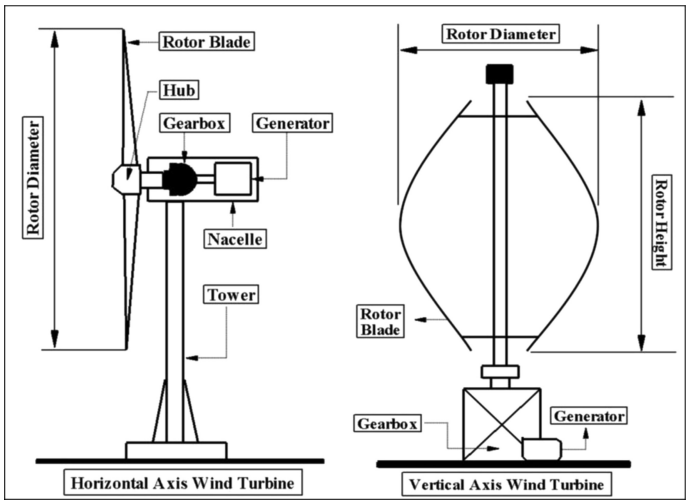

Figure A.1: Horizontal and Vertical Axis Wind Turbines (Huang et al., 2015)

As can be seen in figure A.1 the spinning of the blades by the wind rotate the hub of the wind turbine. This spinning motion is transferred to the drivetrain of the wind turbine within the nacelle. In the drivetrain, the rotational motion of the axis driven by the spinning of the blades is transferred to the gearbox and than to the generator which converts the rotational energy into electrical energy. There are several drivetrain concepts on the market. An example of a drivetrain is shown in figure A.2.

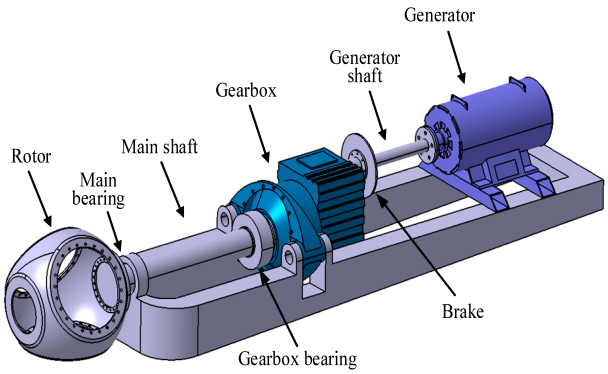

Figure A.2: Example of a Drivetrain (Qian et al., 2017)

Having a bigger rotor diameter enables the wind turbine to obtain more energy out of the wind and therefore produce more power. The power of wind turbines is mea-

sured in megawatts (MW). It can be seen that currently, 10 MW systems are being developed. Another benefit of the up-scaling of wind turbines is that it is cheaper to produce a single 10 MW wind turbine than two 5 MW wind turbines.

However, this up-scaling comes with the necessary innovations. First of all, to create a larger rotor surface area, bigger blades have to be developed. Nowadays, even a blade of 107 meters long is being developed by LM Wind Power, for the Haliade-X wind turbine (Power, 2018). As can be imagined these bigger blades do not only weigh more but also generate larger forces on the wind turbine support structure and have lower rotational speeds. The blade forces are attached to the hub which is attached to the nacelle. It can be imagined that the force and mass generate large stresses on the tower and foundations of the wind turbine. To design a wind turbine in such a way that it can deal with these larger forces requires extra money. If the structural components of the wind turbine can be made lighter by reducing the weight or volume of the components in the nacelle, whilst still being able to deal with the same forces, the whole structure can become cheaper and therefore the LCOE will decrease. One way to do this is by increasing the torque density of the drivetrain. Torque is the moment that results from a force with a certain arm to a rotation point. The torque on the axis of a wind turbine can be calculated with (A.1) (Burton et al., 2011). This equation is obtained with the Blade Element method (BEM). This method is used to calculate the energy that can be generated with a certain wind turbine configuration and wind speed. The BEM method will not be discussed further in this literature study, but a good explanation can be found in Burton et al. (2011).

$$T = \frac{1}{2} \cdot \rho \cdot U_\infty \cdot \pi \cdot R^3 \cdot \lambda \cdot \int_0^R \mu^2 \left(8 \cdot a'(1-a) \cdot \mu - \frac{W}{U_\infty} \cdot \frac{B \cdot \frac{C}{R}}{\pi} \cdot C_d(1+a') \right) d\mu \tag{A.1}$$

What is important to note in (A.1) is the relationship between the blade tip radius R and the torque Q that is generated. It can be seen that when the blade tip radius increases the torque will increase as well.

The torque density is the ratio of the torque handling ability of the mechanism over the mass of the mechanism as shown in (A.2).

$$T_{density} = \frac{T}{m} \tag{A.2}$$

As can be deduced from (A.2) the goal is to obtain an as high as possible torque density ratio. Torque density is a relevant parameter, because it makes it possible to compare the torque capabilities of different drivetrains with the space they occupy. Especially in locations where space is limited, such as the nacelle, the torque density is an important parameter. One could also consider to derive a ratio of the torque over the mass of the drivetrain. In this way the torque capabilities of different drivetrains can be compared with their weight. For this equation it would also be the goal to obtain a ratio that is as high as possible.

The rotational speed (ω) of the blades can be calculated by studying the velocity triangle given in figure A.3. In this figure W represents the wind velocity to the rotation point of the blade, ϕ represents the angle between the wind direction and the rotation plane of the blade, R represents the blade tip radius and a the axial flow induction factor.

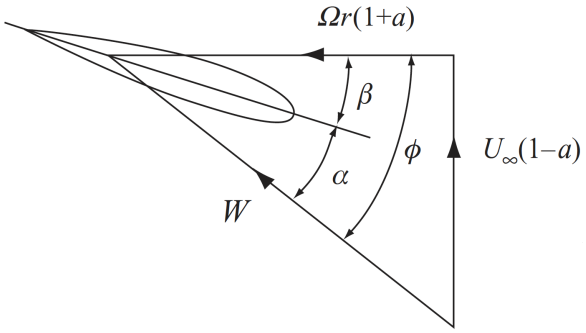

Figure A.3: Velocity triangle (Burton et al., 2011)

From the velociy triangle shown in figure A.3, (A.3) can be obtained. It is important to note that increasing the blade tip length in (A.3) results in a lower ω.

$$\omega = \frac{cos\phi \cdot W}{R \cdot (1+a)} \tag{A.3}$$

The shaft power of a rotating system can be calculated with (A.4). With P being power.

$$P = T \cdot \omega \tag{A.4}$$

Therefore it can be concluded from (A.1) that the torque of the system increases when the blade length increases. So to make the up-scaling of wind turbines possible the drivetrain has to be able to deal with the higher torque without using significantly more space or significantly increasing in mass.

B Drivetrain design selection

B.1 Gearbox Drivetrain Design

The gearbox drivetrain is the most common drivetrain in modern wind turbines. As the name suggests a gearbox can be found between the rotating shaft coming from the rotor hub and the generator, as can be seen in figure 3. A differentiation can be made between high speed, medium speed and low speed gearbox drivetrains. The difference between the two drivetrains is the type of generator that is used to generate the electricity.

Nowadays, high speed gearbox drivetrains are still the most common, because they make it possible to use standard high speed generators and other standard technology (Hau and von Renouard, 2003). These standard, high speed generators have a rotation speed of about 1200 rounds per minute (rpm) (Anaya-Lara et al., 2018). Whereas, a reasonably sized, 5MW wind turbine has a rotational speed of 12 rpm (Anaya-Lara et al., 2018). This means that a gear ratio of 1:100 is necessary in the gearbox. There are two types of gearbox stages used in wind turbines: the parallel shaft stage and the planetary stage. The gearbox shown in figure B.1 only has one planet stage containing three planets and a sun gear. The low speed input shaft coming from the hub of the wind turbine, is attached through a planet carrier to all the three planets, seen in figure B.2. The high speed rotation shaft is attached to the sun gear. To provide a gear ratio of 1:100, usually several planet stages are placed after each other inside the gearbox. Planetary gear stages have an approximate gear ratio of up to 1:12, whereas the parallel shaft gears have an approximate ratio of up to 1:5 (Hau and von Renouard, 2003). The planetary gearbox divides the high torque of the input shaft over the planets. In this way the gearbox can deal with the high dynamic loads caused by the torque.

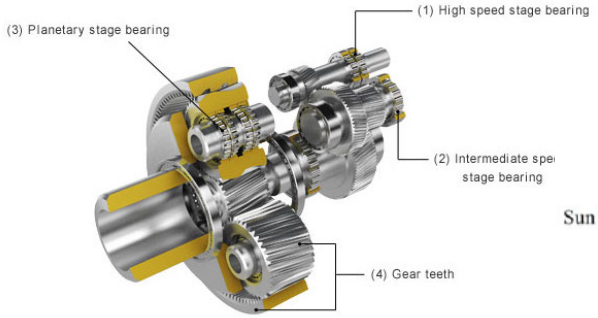

Figure B.1: The planetary and parallel gearbox stages of a wind turbine drivetrain (Olympus, 2018)

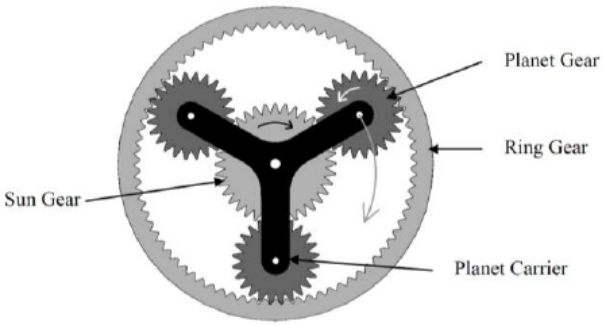

Figure B.2: Planetary gearbox layout (Smith et al., 2013)

A relatively new development is that of the medium speed gearbox drivetrain. This gearbox drivetrain concept involves a medium speed generator, therefore requiring a gear ratio of only 1:25 for a two stage gearbox and 1:15 for a one stage gearbox (Hau and von Renouard, 2003). Most commonly a permanent magnet generator is used (Hau and von Renouard, 2003). The reduction in gear ratio means a reduction in planetary stages, therefore reducing the weight. Also the concept gets rid of the high speed part of the drivetrain. This part of the drivetrain is supposed to be a source of failure, due to the many loading cycles (Hau and von Renouard, 2003).

Of all the gearbox configurations, the gearbox with the relatively lowest cost, weight and dimensions has a configuration of three planetary stages. It must be noted that this research was done for a small turbine with a rated power of 2.5MW and a rotational speed of 25 rpm. For larger turbines a configuration of three gear stages of which the first is planetary and the second and third are parallel becomes more popular (Hau and von Renouard, 2003).

Due to the fact that the gearbox and generator are all placed in line within the nacelle, they are all easily accessible (figure 2.1). This makes performing inspections and maintenance jobs easy. Moreover, in the case of complete failure of one of the drivetrain components, it can easily be replaced (Hau and von Renouard, 2003). Being able to individually remove and install components is very important, especially offshore where it is difficult and expensive to perform these complicated procedures. Looking more from a structural perspective, it can be found that the weight of the gearbox drivetrain is equally distributed over the nacelle (Hau and von Renouard, 2003). Having the center point of gravity located above the tower construction, makes the tower construction less expensive, because it can be designed for lower moment loading.

B.2 Currently used offshore gearbox drivetrain systems

The most commonly used offshore drivetrain configuration uses a three stage gearbox, with two planetary stages and one parallel stage. This gearbox configuration is used by manufacturers such as MHI Vestas (Vestas, 2018) and Senvion (Senvion, 2018) for offshore applications. This type of high speed gearbox has a gear ratio of roughly 1:100. The fact that this gearbox technology has proven itself in the past makes it a save choice for manufacturers and clients. However, the many different moving components in the gearbox are prone to fatigue damage caused by the dynamic behaviour or the wind turbine. Both manufacturers have chosen to create a modular design. That way components can be changed in the nacelle in case of failure. It must be noted that MHI Vestas is currently also using a medium speed gearbox in their V164-9.5MW turbine. This drivetrain configuration shows a lot of promise in regards to the slower rotational speeds of bigger wind turbines.
To ensure variable speed compatibility the two manufacturers use different methods. Senvion has chosen to use a double fed induction generator (DFIG) to ensure a 50HZ or 60HZ output frequency for the grid. The DFIG generator ensures that only 20% of the total output needs to be run through the converter (Senvion, 2018), ensuring a higher efficiency and cheaper converter. The properties of a double fed induction generator will be explained in section C. The MHI Vestas multi megawatt turbines use a permanent magnet generator where all the current is run through the converter with the availibily of better and cheaper converters MHI Vestas tries to create a more reliable and efficient turbine. An explanation about converter technology is given in section C.

C Direct Drivetrain Design

The second drivetrain configuration that will be studied is the direct-drive drivetrain. As the name suggests this drivetrain configuration does not include a gearbox, but instead the generator is directly powered by the wind rotor. In order to explain the direct drivetrain concept better it is necessary to eleborate more on the princiles of wind turbine generators.

As explained briefly in section B.1 the generator is the place where electricity is generated. In a gearbox drivetrain the generator is driven by an axis coming from the gearbox, but in the case of a direct-drive drivetrain it is powered directly by the wind rotor. It is possible to differentiate two types of generators: direct current (DC) and alternating current (AC). A DC current provides a constant flow of current over time whereas an AC current is shaped as a sine wave as shown in figure C.1.

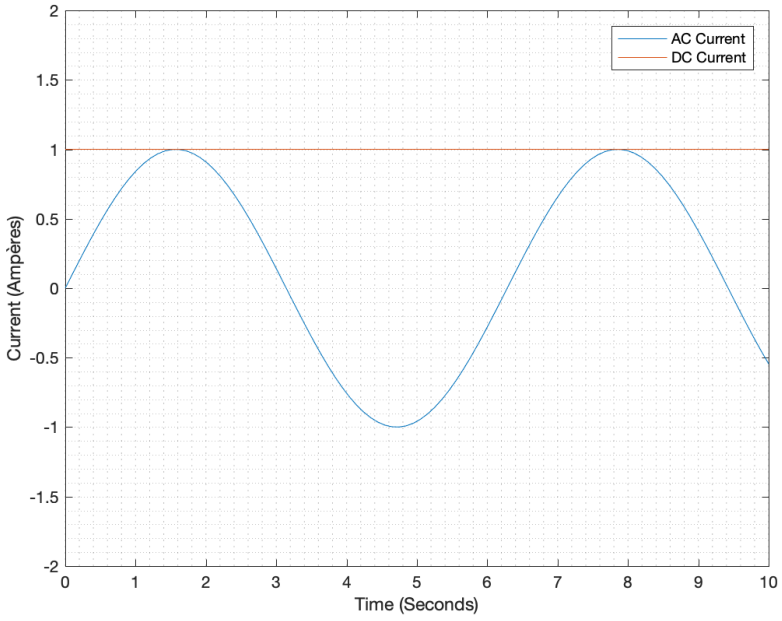

Figure C.1: Direct Current (DC and Alternating Current (AC))

The unsteady torque caused by the variable wind speed causes the power in the drivetrain to fluctuate. This fluctuation of power leads to varying rotation speed of the generator rotor causing a change in current frequency in the generator. For a DC generator this is not the case, because it provides a steady current over time therefore the freqency does not change this is why a DC generator can operate at variable wind speeds (Hau and von Renouard, 2003). However to connect the DC generator to the power grid, the current must be changed to AC. This is done with an DC/AC converter. It must be noted that the European power grid runs on a 50hz frequency whereas the power grid of the United States runs on a 60hz frequency. The rotational speed ω_{gen} of the rotor in generator can be calculated with (C.1) in [rad/s]. f is the frequency of the power grid and n_p is the amount of poles of the generator.

$$\omega_{gen} = \frac{4 \cdot \pi \cdot f}{n_p} \tag{C.1}$$

Nowadays DC generators are not often used anymore, because of their cost and expensive maintenance. For the larger wind turbines, nowadays, AC generators are used (Hau and von Renouard, 2003).

In the past AC generators were connected to the power grid directly. By connecting these generator types directly to the grid large load surges can cause loss of synchronization (Hau and von Renouard, 2003). Loss of synchronization means that the frequency of the generator does not match the frequency of the power grid anymore.

C.1 Fixed speed generators

Two types of wind turbines can be differentiated: fixed speed turbines and variable speed turbines (Anaya-Lara et al., 2018). Fixed speed machines are designed to rotate with a fixed speed, therefore providing a fixed rotating speed for the generator. In (C.2) the equation for the tip speed ratio is given with ω_{hub} being the rotational speed, R being the blade tip radius and being V_w the upwind wind velocity.

$$\lambda = \frac{\omega_{hub} \cdot R}{V_w} \tag{C.2}$$

For a fixed speed turbine the tip speed ratio (λ) changes with the changing wind speed. Therefore the wind turbine will only have a maximum power coefficient C_p at a certain wind speed. A fixed speed machine uses a three phase squirrel-cage generator (SCIG) (Anaya-Lara et al., 2018). The speed of the generator rotor is almost constant and therefore the frequency of the current as well. This is possible, because of the slip in between the rotor and the stator in the generator, which is able to deal with wind gusts acting on the wind rotor. The SCIG has good damping characteristics, but does give large power and load differences (Anaya-Lara et al., 2018). In figure C.2, it can be seen that the bigger the slip in a generator the lower its efficiency becomes. Furthermore, increasing the rated slip percentage also increases the mass and the cost of the generator as seen in figure C.3. The necessity for generators obtaining higher rated slip percentages is driven by the upscaling of wind turbines. Bigger loads on the turbine require larger slip percentages to damp the voltage frequencies introduced to the grid. This is why for bigger wind turbines inverters were introduced. Fixed speed turbines are robost, reliable and have low intitial costs, however they have low energy conversion due to the changing tip speed ratio and therefore non optimal C_p.

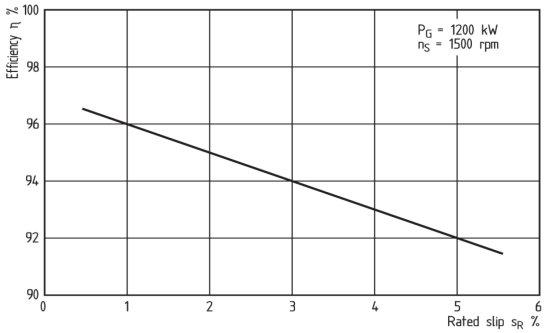

Figure C.2: Efficiency & slip (Hau and von Renouard, 2003)

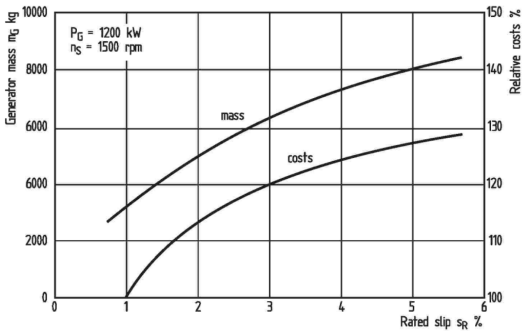

Figure C.3: Cost & Mass for slip in a generator (Hau and von Renouard, 2003)

C.2 Variable speed generators

Modern wind turbines in the MW range use variable speed generators (Hau and von Renouard, 2003). The switch happened for wind turbines larger than 1,5 MW from 1996 (Polinder, Henk). These variable speed generators generate an AC current. As has been previously mentioned, using these generators at variable speeds does not comply with the constant grid frequency that is required. Therefore, in the case of variable speed generators it is necessary to use an inverter to create a constant frequency that matches the frequency of the grid. Using a variable speed generator enables the wind rotor to operate at an optimal aerodynamic performance therefore improving the power coefficient C_p (Polinder, Henk).

The job of the inverter is not only to create a nice sinusoidal shape out of the alternating current, but also rectifies harmonic frequencies (Hau and von Renouard, 2003). In this way a high quality grid frequency can be delivered to the grid. Inverters are usually equipped with a DC-link circuit as shown in figure C.4. This DC-link circuit consists out of a rectifier and the inverter. The rectifier converts the alternating current coming from the generator to direct current by running it through the diodes on the left side of the link. Diodes can only let current through in one direction therefore the current will only flow in one direction. In the case of figure C.4 from the left side to the right side through the top wire (Hau and von Renouard, 2003). The three pairs of diodes can deal with the three phases of the AC current coming from the generator. On the right side of figure C.4 the inverter can be found. The six symbols on the right side are the transistors. They open up in pairs to create a 120^o phase difference to mimic the AC current. However, this AC current still consists out of a blocked wave instead of a sinusoidal wave, possibly damaging AC equipment. To mimic the sinsoidal wave the transistor pairs open and close for different durations each cycle. In this way a different amount of current is let through for each open and close movement, making it possible to create the sinusoidal wave. This type of inverter is called an insulated gate bipolar transistor (IGBT) and is becoming increasingly common in wind turbine drivetrains. Where in the past running all the output power through the inverter would be less efficient, this is not the case today, because of the improved quality of inverters (Hau and von Renouard, 2003).

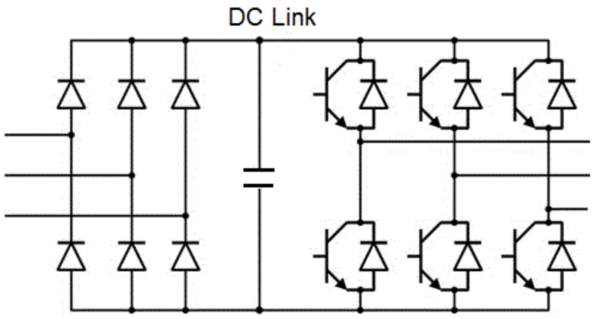

Figure C.4: DC-Link with rectifier & inverter (Electrotechnik, 2018)

C.3 Currently used onshore generator systems

In the list below the six currently used generator system setups can be found (Polinder, Henk). Of these setups, the first setup in the list is constant speed and the others are variable speed setups.

1. Constant speed (CS)
2. Doubly-fed induction generator (DFIG)
3. Electrically Excited direct drive (DD-EE)
4. Permanent magnet direct drive (DD-PM)
5. Variable speed permanent magnet generator with full converter (GFC-PM)
6. Variable speed induction generator with full converter (GFC-IG)

Number one and two from the list correspond with setup one and two in figure C.5. Number three and four from the list correspond with setup three from the top down in figure C.5. Number five and six from the list correspond with the drivetrain setup in the bottom of the figure.

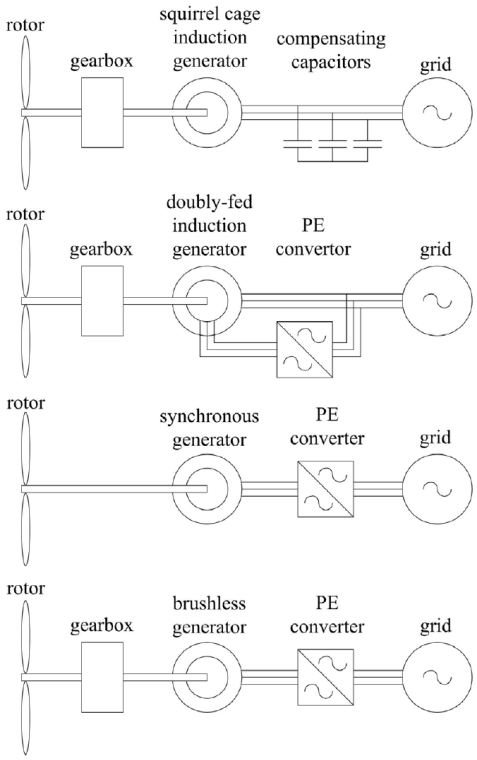

Figure C.5: Drivetrain generator setups (Polinder, Henk)

In the first drivetrain setup in figure C.5 it can be seen that the squirrel cage induction generator (SCIG) is directly connected to the power grid and a multi-stage gearbox is placed in between the rotor and the SCIG. Therefore the generator has to have a fixed rotating speed that generates the same frequency as the power grid

frequency. The grid provides the squirrel cage generator with the necessary reactive power to provide the magnetic flux. The capacitor is used to compensate for the consumed reactive power. Advantages of this system are the simplicity. Due to the slip characteristics of the squirrel cage induction generators the system has reasonable damping. However, the fixed speed characteristics cause the wind rotor not to operate at the optimal power coefficient (Polinder, Henk).

In the second drivetrain a doubly-fed induction generator and gearbox can be seen Polinder, Henk. Moreover, a converter is used in the system to supply the generator rotor with power. This way the generator can operate in over- or sub-synchronous power or in other words as motor or as generator. By controlling the converter the reactive and active power can be controlled that is supplied to the grid. The slip of the generator rotor can also be influenced by controlling the converter, therefore controlling the generator speed. The power used to control the slip of the rotor generator goes to the converter and is from there fed to the power grid. In this way a higher efficiency can be reached than simply applying external resistors for slip control (Hau and von Renouard, 2003). Only one third of the power is fed through the convertor, therefore the convertor can be smaller, has lower costs and and a higher efficiency can be obtained as compared to drivetrain setups that convert all the power. Because of its variable speed capabilities this drivetrain setup can operate at an optimal power coefficient and is currently used in many different wind turbines.

In the third drivetrain setup of figure C.5 no gearbox is spotted. This drivetrain setup is called the direct drive setup and will be one of the three drivetrain setups that this thesis will focus on. All the power coming out of the generator is fed to the IGBT converter. This way the generator frequency is completely decoupled from the power grid frequency. Therefore, no gearbox is necessary to obtain a high rotational generator input speed. However, to obtain a reasonable generator frequency more poles than usual are necessary in the generator. From (C.1) it can be seen that that decreasing the wind rotor speed has to result in a higher amount of poles in order to keep the same frequency, so the generator will increase in size. The electric efficiency of the direct-drive setup with inverter is about 0.94. Therefore, this type of drivetrain has become a serious contender (Hau and von Renouard, 2003). Two types of direct-drive generators can be differentiated as seen in the list presented above: Electrically excited direct drive generators and permanent magnet generators. The difference between the two designs is that the electrically excited generator needs direct current to magnetize the rotor (Staines et al., 2015). This is done by using an rectifier that changes the three phase current current coming from the generator to direct current as shown in figure C.6. It must be noted that only very few companies are using the electrically excited direct drive generator design (Hau and von Renouard, 2003). Furthermore, electrically excited direct drive generators require brushes that need regular maintenance or need to be replaced (Polinder, Henk). Therefore, it is preferred to have a system without brushes.

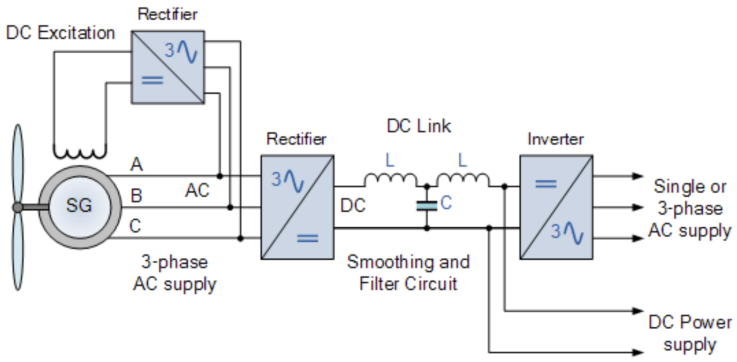

Figure C.6: Electrically excited direct drivetrain (Tutorials, 2018)

The fourth drivetrain design uses a gearbox, brushless generator and full converter as can be seen in figure C.5. Two types of generators can be used: squirrel cage induction generators and permanent magenet generators. Although the usage of a full converter can have disadvantages in regards to the efficiency of the system and cost, the main advantage would be the grid fault ride through properties. During a grid fault, currents in the power grid can become large therefore causing a failure in the power electronics (Polinder, Henk). The converter enables the system to have full control over the current. This is not the case for a doubly-fed induction generator as not all the current is fed to the converter (Hau and von Renouard, 2003). Furthermore, getting rid of the brushes in the generator reduces maintenance and repair costs (Polinder, Henk).

C.4 Currently used offshore direct drive drivetrains

For a generator to be successful offshore, the generator must fulfill the following characteristics listed below (Anaya-Lara et al., 2018).

1. Highly efficient accross the power curve
2. Reliable
3. Cost Effective
4. Lightweight, Compact and Easy to Install
5. Able to operate over a large speed and torque range

The gearbox driven double fed induction generator (DFIG) that is nowadays still the most common generator solution for onshore turbines as mentioned in section C.3 is not the best solution for offshore wind turbines. The reasons for this are that the efficiency of the DFIG goes down with high rated powers of offshore wind turbines (5MW>) and the reliability is not high enough (Anaya-Lara et al., 2018).
Currently, the following existing and new generators are being used or developed for offshore wind turbines, presented in the list below (Anaya-Lara et al., 2018).

1. Direct-driven double fed induction generator (DDDFIG)
2. Direct-drive radial-flux permanent magnet synchronous generator (RFPMSG)
3. Direct-driven ironless permanent magnet synchronous generator (iPMSG)
4. Superconducting Generator

1. The Direct-driven double fed induction generator might be an interesting design because it does not have a gearbox and and not all the current of the system is fed to the converter, making the converter cheaper. Disadvantages of the system are the size of the generator, because of the many poles necessary due to lacking a gearbox, not having good voltage dip ride through properties (Hau and von Renouard (2003)) due to the absence of a full converter and the necessity of needing a big airgap between the rotor and the stator, reducing efficiency (Anaya-Lara et al., 2018).

2. The conventional solution for modern 5MW and bigger offshore wind turbines is the radial-flux permanent magnet synchronous generator (RFPMSG) with full converter. Companies like Siemens Gamesa (Siemens, 2018) and General Electric use this type of offshore drivetrain. The machine however will become very expensive and big when scaling up in torque. The ability to cool the generator is also a problem (Hau and von Renouard, 2003). The reason for using permanent magnet technology as opposed to electric excitation is that permanent magnet technology enables a more compact design, therefore reducing the tower head of the structure. It has to be noted that for direct drive technology the nacelle and the generator have to be designed for each other specifically (Hau and von Renouard, 2003).
In figure C.7 a section is shown of a RFPMSG. It has to be noted that for this setup

the rotor is on the outside and the stator on the inside of the generator. This is called an outer rotor configuration.

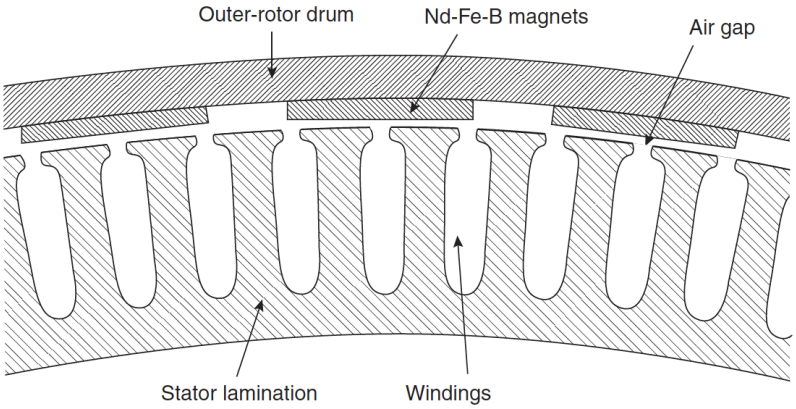

Figure C.7: RFPMSG with outer rotor (Mueller, Markus and Polinder, Henk)

3. A special category of the RFPMSG is the ironless permanent magnet synchronous generator iPMSG. This generator has lower normal forces between the stator and the rotor and therefore the mass of the support structures, that makes up 80% of the mass of the RFPMSG, can be reduced dramatically. An example of an outer rotor IPMSG can be seen in figure C.8. It can be seen that the coils of the generator are supported by plastic. However, to create enough torque more magnetic material is needed which makes the generator more expensive and causes a bigger loss of Eddy currents (Anaya-Lara et al., 2018). Ironless generators are currently not used for offshore applications.

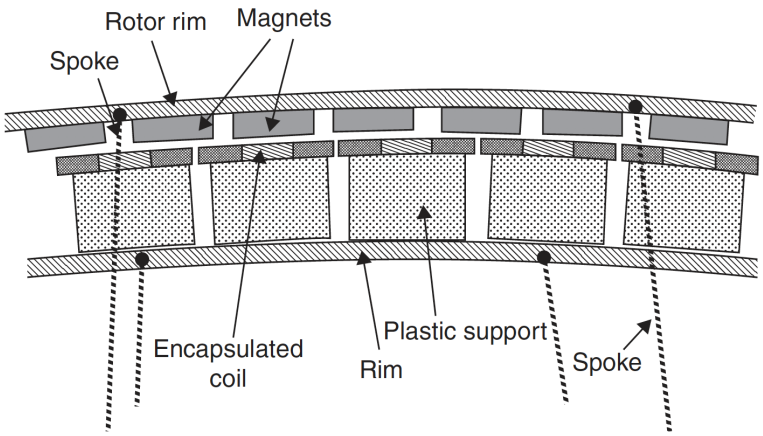

Figure C.8: iPMSG with outer rotor (Mueller, Markus and Polinder, Henk)

4. A future generator candidate for offshore wind applications could be the super conducting generator. Until now this generator has only recently been tested onshore at Thybørn. The permanent magnet generator that used to be in the nacelle was replaced with a super conducting generator (of Twente, 2018). The increase in flux density in the air gap and lower excitation losses of the superconducting generator enable a mass reduction of 50% compared to the the RFPMSG (Anaya-Lara et al., 2018). The diameter of the Thybørn generator was reduced from 5.5 meters to 4 meters of Twente (2018) while having the same 3.6 MW power output, as shown figure D.1. The main difficulty of this new technology is the cooling of the generator. This cooling is done by cryocoolers, that cool the superconducting material. In this way the superconducting material can conduct current with very little to almost no resistance and can create powerful magnetic fields. The cryocoolers turn around with the rotor (of Twente, 2018).

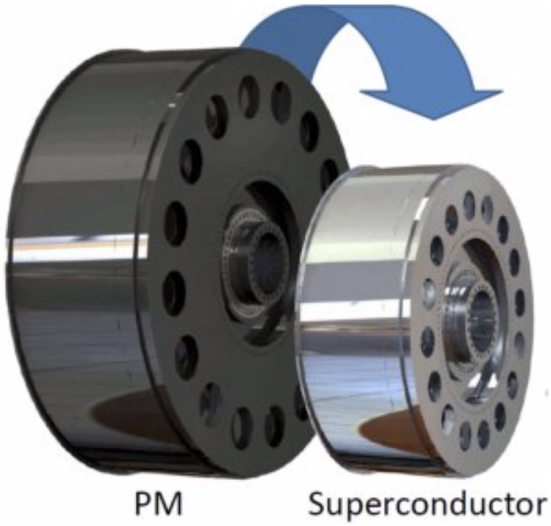

Figure C.9: Superconducting generator volume compared with permanent magnet generator (of Twente, 2018)

D Hydraulic & Hydro Drivetrains

Over the years different companies have been working on hyrdo drivetrain concepts. These companies were ChapDrive AS (Norway), Artemis (Scotland), Voith Turbo (Germany) and DOTPower (Netherlands) (Diepeveen, 2009). Hydraulic in this context can mean water or oil. All of the concepts except the DOT concept use oil as hydraulic fluid. In this literature study we will define a drivetrain concept that uses water as pump fluid with the term hydro. The main motivation for developing hydraulic and hydro drivetrains is to improve the reliability of wind turbines by getting rid of expensive and sometimes unreliable gearboxes, generators and power electronics in the nacelle that are necessary for variable speed wind turbines (Thomsen et al., 2012). As a consequence, using an hydraulic or hydro drivetrain design can reduce the weight in the nacelle benefiting the cost, design and frequency of the structure. If the system is able to handle the same or higher torque loads while decreasing the volume or weight and increase of the torque density is reached.

D.1 Voith

, is only changing the coupling of the gearbox to the generator. This is done by fluid coupling. Increasing or decreasing the pressure of the fluid in the coupling influences the damping of the coupling. This method provides the system with sufficient damping enabling the generator rotor to rotate with a constant speed (Diepeveen, 2009). Voith is still designing hydraulic couplings, however they are not specifically targeting the wind energy market anymore.

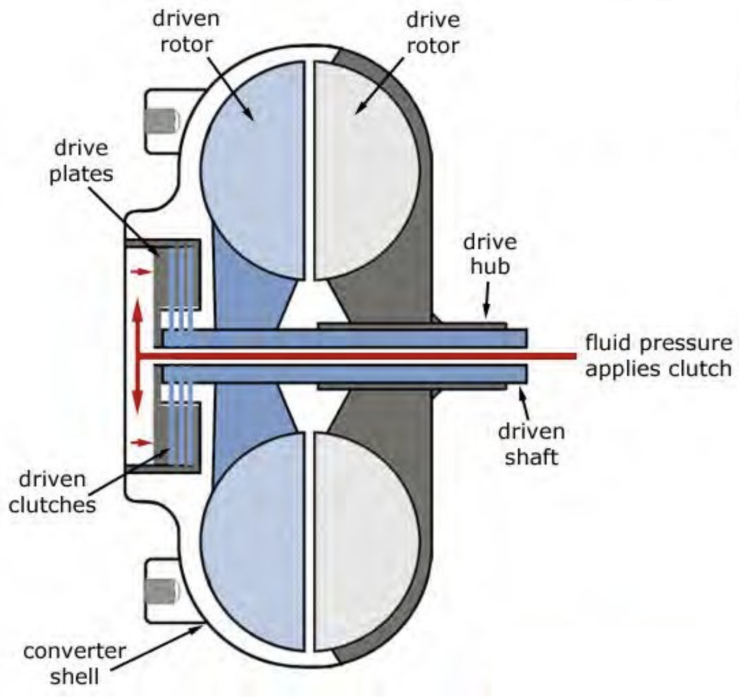

Figure D.1: A section of a fluid coupling with on the left side the driven rotor and on the right side the drive rotor (Aboshosha et al., 2015)

D.2 Artemis

, is using poppet valves to create high, low or no pressure difference. By being able to very rapidly control the pressures in these valves, it is possible to control the discharge pressure. In the Artemis concept two hydraulic motors are used to drive the two synchronous generators at a fixed rotational speed. The drivetrain setup and orientation of the poppet valves can be seen in figure D.2 and figure D.3. Artemis is nowadays part of MHI Vestas and are currently still busy with developing their system.

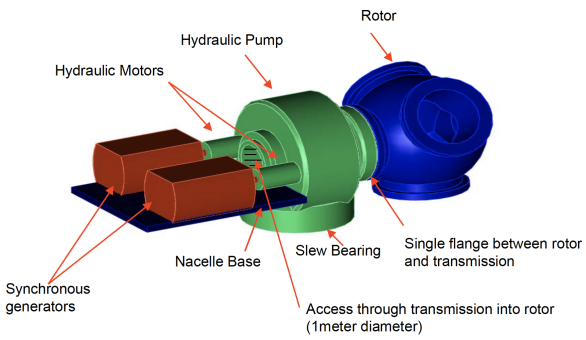

Figure D.2: Artemis hydraulic drivetrain concept (Rampen)

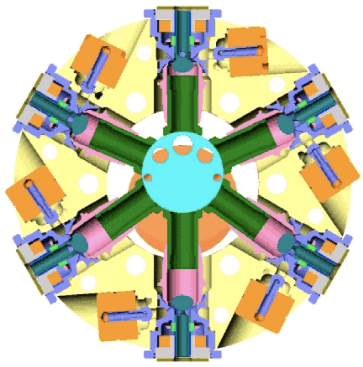

Figure D.3: Artemis poppet valves (Rampen)

D.3 Chapdrive

The drivetrain concept from Chapdrive is in some ways similar to the drivetrain concept developed by DOT. The similarity is in the fact that the generator is not located in the nacelle. This makes the nacelle lighter and therefore the whole design becomes cheaper. In figure D.4 the concept for the chapdrive can be seen. A pump with constant stroke volume will pump oil to a motor which in turn powers the generator (Diepeveen, 2009). The motor is able to very its stroke in turn being able to power the generator with a constant speed. The concept of chapman was very promising however, due to a dip in the wind energy market after the economic crisis one of their major investors pulled out and the company was liquidated.

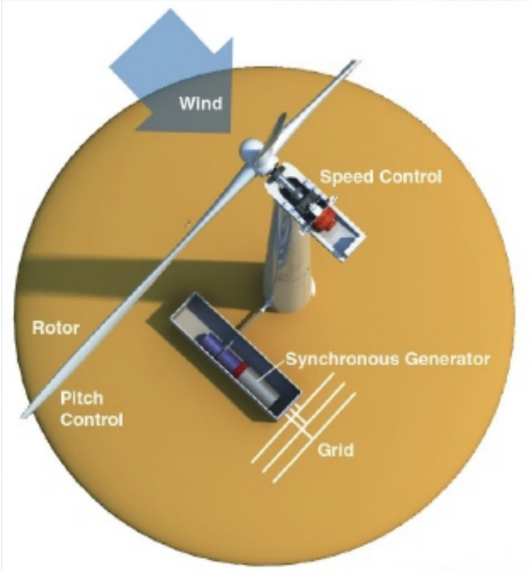

Figure D.4: Chapdrive drivetrain design (Chapdrive, 2009)

D.4 Hydro drivetrain design

DOTpower is currently busy developing and testing their new hydraulic turbine design. The first Delft Offshore Turbine (DOT) prototype has recently been installed at the Amalia Offshore Windfarm (OffshoreWIND.biz, 2018). As mentioned the concept is comparable to that of Chapdrive. The radical difference is that DOTpower wants to use sea water in the hydraulic circuit instead of oil. This cuts out the oil loop and therefore the motor. The pressurized sea water is fed to a Pelton generator. Using sea water as an hydraulic pump fluid has never been done before and therefore a new pump has to be developed (Michailidis and Diepeveen, 2011). By regulating the pressure with the pump in the nacelle the discharge can be kept equal, enabling a constant rotation speed of the Pelton generator.
However, the DOT prototype still uses oil as hydraulic fluid for the pump in the nacelle. The pressurized oil drives a second pump that pressurizes sea water and pumps it into the Pelton turbine, which is in turn connected to a synchornous generator. The final concept for the DOT will get rid of the second uses sea water for the entire system.
The ambitions of DOTpower go even further by letting multiple turbines drive one Pelton generator, herewith further reducing the LCOE of offshore wind turbines (Michailidis and Diepeveen, 2011).

References

A. Aboshosha, J. Amarnath, K. Reddy, M. Zohdy, S. NARABOINA, S. Omekanda, T. A. Perkins, V. Purnachandra Rao, S. Tirunagari, P. Srinath Rajesh, J. El-Azab, H. Kandel, and M. Khedr. Acse-volume14-issue2-p1111453358. 07 2015. doi: 10.13140/RG.2.1.3901.1689.

O. Anaya-Lara, J. O. Tande, K. Uhlen, and K. Merz. *Offshore Wind Energy Technology*. Wiley Online Library, 2018.

J. B. Anders Nymark, Magnus Gottlieb. Europe powered by green energy, 2018.

Asger Bech Abrahamsen, Dong Liu and Henk Polinder. Direct drive superconducting generators for innwind.eu wind turbines. Technical report, DTU Wind, 2018.

I. Boiadjiev, J. Witzig, T. Tobie, and K. Stahl. Tooth flank fracture—basic principles and calculation model for a sub surface initiated fatigue failure mode of case hardened gears a2, velex, philippe. In *International Gear Conference, Lyon, France, Aug*, pages 26–28, 2014.

R. BOSCH. Hydraulic formulary.

R. G. Budynas, J. K. Nisbett, et al. *Shigley's mechanical engineering design*, volume 8. McGraw-Hill New York, 2008.

T. Burton, N. Jenkins, D. Sharpe, and E. Bossanyi. *Wind energy handbook*. John Wiley & Sons, 2011.

Chapdrive. Chapdrive - hydrostatic drive for wind turbines, 2009. URL `https://www.slideshare.net/Calion/chap-drive-1`.

A. A. CIRCUITS. Permeability and saturation, 2018. URL `https://www.allaboutcircuits.com/textbook/direct-current/chpt-14/permeability-and-saturation/`.

M. Díaz, R. Cardenas, B. M. Espinoza, A. Mora, and F. Rojas. A novel lvrt control strategy for modular multilevel matrix converter based high-power wind energy conversion systems. In *Ecological Vehicles and Renewable Energies (EVER), 2015 Tenth International Conference on*, pages 1–11. IEEE, 2015.

N. Diepeveen. Design considerations for a wind-powered seawater pump. In *European Offshore Wind Conference Proceedings, EWEA, Marseille, France. Available at: http://www. ewea. org*, 2009.

N. Diepeveen, A. Jarquin Laguna, and A. Kempenaar. Water-hydraulic power transmission for offshore wind farms. In *Topic water hydraulics: Proceedings of the Dutch Fluid Power Conference, Ede, The Netherlands, 13 Sept., 2012*. Vereniging Platform Hydrauliek, 2012.

N. F. B. Diepeveen. On the application of fluid power transmission in offshore wind turbines. 2013.

Electrotechnik. What is a dc link?, 2018. URL https://www.electrotechnik.net/2015/02/what-is-dc-link.html.

Enercon. Enercon e82, 2018. URL https://www.enercon.de/en/products/ep-2/e-82/.

L. ENERGY. Design race in wind turbine drivetrains, 2014. URL https://www.leonardo-energy.org/resources/768/design-race-in-wind-turbine-drivetrains-5824781952ab0.

L. Fingersh, M. Hand, and A. Laxson. Wind turbine design cost and scaling model. Technical report, National Renewable Energy Lab.(NREL), Golden, CO (United States), 2006.

K. S. Gears. Bending strength of spur and helical gears, 2011. URL https://khkgears.net/new/gear_knowledge/gear_technical_reference/bending-strength-of-spur-and-helical-gears.html.

C. GHIŢĂ, S. Nedelcu, I. TRIFU, and T. TUDORACHE. Finite element analysis of the useful magnetic flux of a low speed pmsg. *Scientific Bulletin of University POLITEHNICA of Bucharest, Series C*, 75(1):239–250, 2013.

R. B. Group. Product catalogue hägglunds cbm. *Bosch Rexroth Mellansel AB*, 2018.

Hagglunds. Hagglunds, 2018. URL https://www.boschrexroth.com/en/xc/company/haegglunds-landingpage/haegglunds-landingpage.

H. Hartviksen. Application of scaling laws for direct drive permanent magnet generators in wind turbines. Master's thesis, NTNU, 2015.

E. Hau and H. von Renouard. *Wind turbines: fundamentals, technologies, application, economics*. Springer, 2003.

G.-Y. Huang, Y. Shiah, C.-J. Bai, and W. Chong. Experimental study of the protuberance effect on the blade performance of a small horizontal axis wind turbine. *Journal of Wind Engineering and Industrial Aerodynamics*, 147:202–211, 2015.

I. .-. . International Organization for Standardization. Wind turbines–part 4: Design requirements for wind turbine gearboxes, 2012.

B. B. Jensen, N. Mijatovic, and A. B. Abrahamsen. Advantages and challenges of superconducting wind turbine generators. In *2nd International Conference E/E Systems for Wind Turbines*, 2012.

KhanAcademy. What is magnetic flux?, 2018. URL https://www.khanacademy.org/science/physics/magnetic-forces-and-magnetic-fields/magnetic-flux-faradays-law/a/what-is-magnetic-flux.

M. A. Laughton and M. G. Say. *Electrical engineer's reference book*. Elsevier, 2013.

D. Michailidis and N. Diepeveen. Conceptual design of a dot farm generator station. In *Proceedings of the EWEA Offshore 2011 Conference, Amsterdam, The Netherlands, 29 November-1 December 2011*. European Wind Energy Association, 2011.

W. P. Monthly. Company profile: Ge sets its sights on offshore markets, 2011. URL https://www.windpowermonthly.com/article/1067473/company-profile-ge-sets-its-sights-offshore-markets.

Mueller, Markus and Polinder, Henk. *Electrical drives for direct drive renewable energy systems*. Elsevier, 2013.

H. Murrenhoff. *Fundamentals of Fluid Power: Part 1: Hydraulics*. Shaker, 2016.

A. R. Nejad, Y. Guo, Z. Gao, and T. Moan. Development of a 5 mw reference gearbox for offshore wind turbines. *Wind Energy*, 19(6):1089–1106, 2016a.

A. R. Nejad, Y. Guo, Z. Gao, and T. Moan. Development of a 5 mw reference gearbox for offshore wind turbines. *Wind Energy*, 19(6):1089–1106, 2016b.

U. of Twente. Lighter windmills thanks to superconductivity almost no use of rare earth metals), 2018. URL https://www.utwente.nl/en/news/!/2018/11/320075/lighter-windmills-thanks-to-superconductivity.

OffshoreWIND.biz. Aegir installs dot at princess amalia, 2018. URL https://www.offshorewind.biz/2018/10/01/aegir-installs-dot-at-princess-amalia/.

Olympus. Inspections of wind turbine gearboxes, 2018. URL https://www.olympus-ims.com/en/applications/rvi-wind-turbine/.

H. Polinder. *Principles of electrical design of permanent magnet generators for direct drive renewable energy systems*. Elsevier, 2013.

H. Polinder, D. Bang, R. Van Rooij, A. McDonald, and M. Mueller. 10 mw wind turbine direct-drive generator design with pitch or active speed stall control. In *2007 IEEE International Electric Machines & Drives Conference*, volume 2, pages 1390–1395. IEEE, 2007.

Polinder, Henk. *Overview of and trends in wind turbine generator systems*. 2011.

L. W. Power. Ge unveils haliade-x: The world's largest offshore wind turbine, powered by 107-meter-long lm blades, 2018. URL https://www.lmwindpower.com/en/stories-and-press/stories/news-from-lm-places/ge-announces-haliade-x-the-worlds-largest-offshore-wind-turbine.

J. Pyrhonen, T. Jokinen, and V. Hrabovcova. *Design of rotating electrical machines*. John Wiley & Sons, 2013.

P. Qian, X. Ma, and D. Zhang. Estimating health condition of the wind turbine drivetrain system. *Energies*, 10(10):1583, 2017.

S. P. Radzevich. *Dudley's handbook of practical gear design and manufacture*. CRC Press, 2012.

W. Rampen. Gearless transmissions for large turbines-the history and future of hydraulic drives artemis ip ltd, scotland.

F. Roos and C. Spiegelberg. *Relations between size and gear ratio in spur and planetary gear trains*. Number 1. KTH, 2005.

R. S. Semken, M. Polikarpova, P. Röyttä, J. Alexandrova, J. Pyrhönen, J. Nerg, A. Mikkola, and J. Backman. Direct-drive permanent magnet generators for high-power wind turbines: Benefits and limiting factors. *IET Renewable Power Generation*, 6(1):1–8, 2012.

Senvion. 6.2m126, 2018. URL https://www.senvion.com/global/en/products-services/wind-turbines/6xm/62m126/.

L. Sethuraman, M. Maness, and K. Dykes. Optimized generator designs for the dtu 10-mw offshore wind turbine using generatorse. In *35th Wind Energy Symposium*, page 0922, 2017.

G. Shrestha. Structural flexibility of large direct drive generators for wind turbines. 2013.

G. Shrestha, H. Polinder, and J. Ferreira. Scaling laws for direct drive generators in wind turbines. In *2009 IEEE International Electric Machines and Drives Conference*, pages 797–803. IEEE, 2009.

Siemens. Wind turbine sg 8.0-167 dd, 2018. URL https://www.siemens.com/content/dam/webassetpool/mam/tag-siemens-com/smdb/wind-power-and-renewables/offshore-wind-power/documents/brochures/sg-data-sheet-offshore-wind-turbine-sg-8-0-167-en.pdf.

W. Smith, L. Deshpande, R. Randall, and H. Li. Gear diagnostics in a planetary gearbox: a study using internal and external vibration signals. *International Journal of Condition Monitoring*, 3(2):36–41, 2013.

C. S. Staines, C. Caruana, and J. Licari. Review of power converters for wind energy systems. In *WINERCOST Workshop 'Trends and Challenges for Wind Energy Harvesting', Coimbra, Portugal, 30th-31st March*, 2015.

K. E. Thomsen, O. Dahlhaug, M. Niss, and S. Haugset. Technological advances in hydraulic drive trains for wind turbines. *Energy Procedia*, 24:76–82, 2012.

T. Tobie, F. Hippenstiel, and H. Mohrbacher. Optimizing gear performance by alloy modification of carburizing steels. *Metals*, 7(10):415, 2017.

T. T. Tran and A. D. Smith. Incorporating performance-based global sensitivity and uncertainty analysis into lcoe calculations for emerging renewable energy technologies. *Applied Energy*, 216:157–171, 2018.

A. E. Tutorials. Synchronous generator, 2018. URL http://www.alternative-energy-tutorials.com/wind-energy/synchronous-generator.html.

Utah University. Contact stresses and deformations, 2019. URL http://www.mech.utah.edu/~me7960/lectures/Topic7-ContactStressesAndDeformations.pdf.

M. Vestas. V164-10.0 mw turbine, 2018. URL http://www.mhivestasoffshore.com/innovations/.

Wenzel. Sustainable wind power generation depends on wenzel cmm coordinate measuring machines, 2014. URL https://www.wenzelamerica.com/sustainable-wind-power-generation-depends-on-wenzel-cmm-coordinate-measuring-machi

L. Yang, Z. Jiang, Z. Gao, T. Moan, et al. Dynamic analysis of a floating wind turbine with a hydraulic transmission system. In *The Twenty-fifth International Ocean and Polar Engineering Conference*. International Society of Offshore and Polar Engineers, 2015.